TAMPEREEN TEKNILLINEN YLIOPISTO
TAMPERE UNIVERSITY OF TECHNOLOGY

Pooya Saketi

Microrobotic Platform with Integrated Force Sensing Microgrippers for Characterization of Fibrous Materials:
Case Study on Individual Paper Fibers

Julkaisu 1309 • Publication 1309

Tampere 2015

Tampereen teknillinen yliopisto. Julkaisu 1309
Tampere University of Technology. Publication 1309

Pooya Saketi

Microrobotic Platform with Integrated Force Sensing Microgrippers for Characterization of Fibrous Materials:
Case Study on Individual Paper Fibers

Thesis for the degree of Doctor of Science in Technology to be presented with due permission for public examination and criticism in Festia Building, Auditorium Pieni Sali 1, at Tampere University of Technology, on the 21st of July 2015, at 12 noon.

Tampereen teknillinen yliopisto - Tampere University of Technology
Tampere 2015

ISBN 978-952-15-3545-1 (printed)
ISBN 978-952-15-3550-5 (PDF)
ISSN 1459-2045

Abstract

Mechanical characterization of micro-scale fibrous materials determines the key parameters which affect the quality of products such as composites, textile and paper. The current laboratory tests are mainly based on bulk measurements. This thesis introduces a microrobotic platform to handle and to characterize micro-scale fibers (MF), with the dimensions of few micrometers to hundreds of micrometers, at individual fiber level. The platform facilitates handling and specimen preparation of micro-scale fibrous material. A major challenge in mechanical characterization of MF is lack of proper force sensing microgrippers in the market. MF do not need a lot of force to manipulate, but their ultimate tensile strength is high and relatively large forces are required to perform a micro-tensile test. In this thesis, three force sensing microgrippers are developed and they are integrated into the mentioned microrobotic platform. Two of them are developed to measure the bonding forces between individual pulp fibers, normal to the bonded area (Z-direction) and parallel to the bonded area (shear-mode). Their force sensing solution is based on bending polyvinylidene fluoride (PVDF) films and their force range is up to $10mN$. The third one, with the force range of $20mN$, is developed to perform micro-tensile tests on MF. It uses a microspring and a magnetic encoder to measure the force. The force range of this force sensing microgripper can easily be increased by changing its microspring to a stiffer one. This feature makes the proposed force sensing approach adaptable to a wide range of MF.

Even though pulp and paper fibers are used as a case study in this thesis, the applications of microrobotic solutions presented here are not limited

to pulp and paper fibers for the following reason: pulp and paper fibers are natural fibers with random morphology, therefore if a microrobotic solution is capable of handling these morphologically challenging fibers, it is easily adaptable to synthetic fibers which have uniform morphology. The prototypes of all three force sensing microgrippers are calibrated and their performance are validated.

Acknowledgment

This work was carried out in the Micro- and Nanosystems Research Group at Department of Automation Science and Engineering, Tampere University of Technology. The research results were achieved during Mar. 2010 – Dec. 2014 under several research projects: SmartFibre, PowerBonds (EU) and Fibam (Academy of Finland). The goals of these projects formulated the need and the structure of this thesis. The funding of TUT President's Doctoral Program for the last year of my PhD studies is also gratefully acknowledged.

I want to express my gratitude to Prof. Pasi Kallio who has supported me with his knowledge and dedication throughout my PhD studies, and provided me the perspective required to conduct research in the field of Microsystems Technology.

My special thanks go to the pre-examiners Prof. Wolfgang Bauer from Graz University of Technology and Prof. Andreas Dietzel from Braunschweig University of Technology for reviewing my thesis and their constructive comments. I am deeply grateful to Prof. Stéphane Regnier from Pierre-and-Marie-Curie University and Prof. Wolfgang Bauer from Graz University of Technology to be my opponent at the public PhD defense.

I wish to thank the professors, colleagues and the personnel of the Department of Automation Science and Engineering for providing such a great research atmosphere. I am thankful to the present and past col-

leagues at Micro- and Nanosystems Research Group, Juha Hirvonen, Mathias von Essen, Kourosh Latifi, Yuli Lai and Martina Bozic for their input and support during the projects, and also Joose Kreutzer and Mariaana Savia. I would like to thank Prof. Jukka Lekkala and his research group, especially Antti Vehkaoja, Mikko Peltokangas and Satu Rajala for their collaboration and support on the measurement electronics.

I am indebted to Prof. Artem Kulachenko from Royal Institute of Technology (KTH) for his unsparing guidance on mechanical optimization methods. I also would like to thank Manuel Mikczinski from University of Oldenburg for all of the joint works and publications which we accomplished together.

My wholehearted thanks go to my lovely wife, Negar, who has been the unsetting sun of my life in the dark winters of Finland. I want to thank my family, especially my parents Parviz and Tahereh, for their everlasting love and support throughout my life, and also my grandmother for her Sunday calls which has kept me connected to my roots back in Iran.

Finally, I would like to thank my dear friends Ali, Morteza, Milad and Fatemeh for all of the wonderful and memorable time which we have spent together. Their friendship has supported me to move forward all these years.

Tampere, 10th June 2015
Pooya Saketi

Contents

List of Acronyms

AFM	Atomic Force Microscope
C.#-F.#	Component Number-Figure Number
CNT	Carbon Nanotubes
CV	Coefficient of Variation
ElNi	Electroplated Nickel
FOV	Field-of-View
GH	Gauge Height
GW	Gauge Width
LIGA	a German acronym for “Lithographie” (Lithography), “Galvanoformung” (Electroplating), “Abformung” (Molding)
MEMS	Microelectromechanical systems
MF	Micro-scale Fibers
NT	Nanotomography
PG	Pulling Microgripper
PLS	Precision Linear Slider
PVDF	Polyvinylidene fluoride
RH	Ring Height - The transverse diameter of the ellipses in the microspring.
RMSE	Root-Mean-Square-Error
RQ	Research Question
RSD	Relative Standard Deviation
RW	Ring Width - The conjugate diameter of the ellipses in the microspring.
SEM	Scanning Electron Microscopy
SG	Sensitive Microgripper

STD Standard Deviation
STM Scanning Tunneling Microscopy

List of Symbols

α	Crossing Angle
β	Vertical Angle
ϵ^{σ}_{km}	Permittivity
ν	Poisson's Ratio
σ	Stress
σ_{max}	Maximum Stress
σ_y	Yield Strength
A_{calc}	Calculated area of a fiber bond
Cr	Chromium
Cu	Copper
c^E_{ijkl}	Elastic Compliance
D_k	Dielectric Displacement
d_{kij}	Piezoelectric Coefficient
D_{oC}	Output Signal of Optical Encoder of Linear Actuator used as Position Feedback
D_{oR}	Displacement of Linear Actuator
D_{oM}	Displacement Output Signal of Magnetic Encoder
E	Young's Modulus
E_m	Electric Field
f_{iC}	Actuation Frequency of Piezo-drive of the Linear Actuator
G	Penalty Functions for State Variable Constraints
H	Penalty Functions for State Variable Constraints
L_0	Initial Length
ΔL_G	Displacement of pulling microgripper
Si	Silicon

ΔL_S	Displacement of sensitive microgripper
S_{ij}	Strain
U_{max}	Maximum Displacement
V	Voltage
V_{iC}	Actuation Voltage of Piezo-drive of the Linear Actuator
V_{oRF}	Voltage out of the Reference Force Sensor
ΔV	Voltage Difference
$w1, w2$	Widths of individual pulp fibers
W	Penalty Functions for State Variable Constraints
X	Penalty Functions for Design Variable Constraints

List of Figures

List of Tables

1 Introduction

This doctoral thesis studies the technological solutions for handling, sample preparation and mechanical characterization of micro-scale fibrous materials. This chapter reasons out the motivation for this thesis by discussing the challenges in the aforementioned fields and providing the research questions. After forming the scope of the thesis, the objectives are defined and the contributions are presented. Finally, the structure of the thesis is outlined.

1.1 Motivation and Challenges

Micro-scale fibrous materials are widely used in various industrial sectors such as composites (carbon nanotubes and glass fibers), biomedical technology (bio-degradable fibers), information technology and optics (glass fibers), textile (nylon, cotton, wool, hemp), pulp and paper (wood fibers), cosmetics (hair), military and safety (Kevlar). A major step in developing a product based on any of the aforementioned fibrous materials is mechanical characterization. Due to the small dimensions, few micrometers to hundreds of micrometers, of these fibrous materials, handling and characterizing them as individual fibers are tedious tasks. Therefore, they are either characterized as bulk materials in a web or a

matrix, or if they are characterized as individuals, they are characterized in small numbers.

The tools and devices for mechanical characterization of these materials in a web or a matrix are well developed, and they are commercially available. But characterizing these materials in bulk, does not provide direct data on the behavior of fibers at the individual level and it requires interpretation. For example in a paper hand-sheet, what portion of the strength comes from fibers and what portion comes from bonds? Therefore, tools to characterize micro-scale fibrous materials at individual fiber level with high throughput, minimum 500 fibers per day, are required to produce statistically reliable data. Such data are not only interesting for material producing industries to lower their costs, but also for academia in understanding fundamentals of failure mechanisms. Both industry and academia can also benefit from such tools to provide data for their modeling tools. Even though the mathematical models for multi-scale modeling of materials and homogenization techniques are well developed, experimentally acquired data on the mechanical properties of such fibrous materials are needed to utilize these existing models.

The author argues that even though microrobotic technologies have been extensively utilized in many application areas such as living cells and micro-assembly, the potential of microrobotic technologies has been very inadequately utilized in fibrous materials research. In this thesis, novel microrobotic solutions are presented for both specimen handling and mechanical characterization of micro-scale fibrous materials. An important aspect of the entire system is its modularity which allows prompt reconfiguration of the microrobotic platform to match the needs of a versatile measurement setup.

The microrobotic solutions developed in this thesis are mainly focused on pulp and paper fibers for the following two reasons: (1) pulp and paper industry is a major player in Finnish economy and it contributes to 1 % of the national gross domestic product; (2) pulp and paper fibers are natural fibers with challenging morphology, therefore if a microrobotic

solution is capable of handling these fibers, it is easily adaptable to synthetic fibers with uniform morphology. Therefore, the applications of microrobotic solutions presented in this thesis are not limited to pulp and paper fibers even though they are used as a case study example.

1.2 Methodology and Scope

The thesis discusses the development of microrobotic solutions for handling, specimen preparation and mechanical characterization of microscale fibrous materials. The need for each solution has been initiated based on industrial and academic feedback. After selecting the approach to tackle the need, a proof of concept for each solution is tested and then a prototype is developed accordingly. The performance of the prototypes is validated and finally they are tested in real laboratory experiments.

The solutions for handling and specimen preparation are considered as preliminary steps for a final microrobotic platform capable of mechanical characterization of fibrous materials. The focus of the thesis is primarily on developing force sensing microgrippers which are integrable into the microrobotic platform. The author aims to prove that the working principle of the developed prototypes for force sensing microgrippers are valid. The steps to turn these prototypes into a product level solution are beyond the contributions of this thesis. The microrobotic solutions are presented purely from a hardware point of view. The software and automation aspects are not a part of this thesis and therefore they are not discussed. In brief, the thesis presents a modular tele-operated microrobotic platform capable of manipulating fibers with dimensions from few to hundreds of micrometer. It includes force sensing microgrippers with the force ranges of up to 20 mN and sensitivities of as low as 27.22 $\mu N/mV$.

1.3 Objectives and Contributions

The objective of the thesis is to develop microrobotic solutions for handling, specimen preparation and mechanical characterization of micro-scale fibrous materials, with the mechanical characterization being the main objective. The following research questions (RQ)s are addressed in this thesis:

RQ.1 Which microrobotic solutions can address the challenges of handling and specimen preparation of micro-scale fibrous materials?

RQ.2 Which force sensing approach can measure bonding forces of paper fibers at individual bond level?

RQ.3 Which force sensing approach can be used for micro-tensile testing of fibers using a microgripper?

The contributions of the thesis are as follows:

- A microrobotic platform for manipulation and specimen preparation of micro-scale fibrous materials for microscopic studies is designed and developed.
- Novel force sensing approaches for microgrippers used in micro-tensile testing applications are proposed.
- A polyvinylidene fluoride (PVDF) based force sensor with passive specimen holder capable of measuring the Z-directional breaking forces of paper fiber bonds is developed.
- A PVDF based force sensing microgripper for measuring bond breaking forces in shear-mode is developed.
- Utilizing microsprings as force sensors for micro-tensile testing applications is a new approach. The use of electroplated Nickel structures for force sensing applications is reported presumably for the first time.

- A microrobotic platform for mechanical characterization of micro-scale fibrous materials is developed.

1.4 Outline of the Thesis

The thesis is organized as follows: Chapter 2 discusses the background, State-of-the-Art and how to go beyond it. Chapter 3 describes the design and implementation phases of a microrobotic platform for specimen preparation of micro-scale fibrous materials. Chapter 4 explains design and fabrication of three force sensing microgrippers for mechanical characterization of micro-scale fibrous materials. Chapter 5 encompasses the integration of developed force sensing microgrippers into the microrobotic platform, and demonstrates the mechanical characterization capabilities of the platform.

1.5 List of the Definitions and Technical Terms

For the sake of simplicity and fluency of the thesis the repetitive technical terms are defined as follows. If these terms are used for any other meaning than defined in the following, they are explained in the same paragraph.

3D-MICROMANIPULATOR: It includes three SLC-1730 micropositioners (SmarAct GmbH, Germany) perpendicular to each other, providing a 100 nm resolution, a ± 10 μm absolute accuracy, a ± 1 μm repeatability and a 21 mm travel in X, Y and Z axis directions.

BOND: The term "bond" refers to a single fiber crossing made of two individual paper fibers. In order to differentiate between the chemical and mechanical bonding mechanisms, pulp and paper chemists sometimes use a term "joint" instead of "bond", while using the term "bond" is more common among the physicists. In this thesis the term "bond" refers to the summation of all mechanical and chemical forces which hold two individual paper fibers together.

LINEAR ACTUATOR: It refers to an SLC-1730 micropositioner (SmarAct GmbH, Germany) which provides a 100 nm resolution, a ± 10 μm absolute accuracy, a ± 1 μm repeatability and a 21 mm travel.

PULP FIBER AND PAPER FIBER: Pulp fibers are wood fibers which have been extracted from wood in a pulp mill using chemical or mechanical processes. Pulp fibers are turned into paper-sheets in a paper mill. Paper fibers are the fibers extracted from a paper sheet. Duo to the technological focus of the thesis on microrobotics and microsensors, for the convenience of non-paper experts, the term "Paper Fiber" is commonly used instead of "Pulp Fiber".

REFERENCE FORCE SENSOR: It refers to an FT-S10000 force sensor with ± 10 mN force range (FemtoTools AG, Switzerland). Its sensitivity and resolution are 5000 $\mu N/V$ and 2 μN, respectively. Its operating principle is based on measuring the differential capacitance of a moving Silicon comb structure.

RELATIVE STANDARD DEVIATION (RSD): RSD is the absolute value of the coefficient of variation expressed as a percentage. In other words, it is the ratio of the standard deviation to the mean expressed as a percentage.

ROTARY-TABLE: It refers to a SR-1908 rotary positioner (SmarAct GmbH, Germany) which provides a resolution of 10 μ°.

SIDE-VIEW: Refers to a vision system which includes a Manta-G504 camera (AVT AG, Germany) and a motorized Macro Zoom 7000 with 1.1X magnification (Navitar, USA).

TOP-VIEW: Refers to a vision system which includes a Sony-XCDU100 camera (Sony Co., Japan) and a motorized $12\times$ Zoom with $0.29\times - 3.5\times$ magnification (Navitar, USA).

XY-TABLE: It includes two SLC-1760 micropositioners (SmarAct GmbH, Germany) perpendicular to each other, providing a 100 nm resolution, a ± 10 μm absolute accuracy, a ± 1 μm repeatability and a 41 mm travel in X and Y directions.

2 Background and State-of-the-Art

2.1 Individual Paper Fibers and Bonds

Depending on their type, wood fibers are cells having typical dimensions of 0.6 $mm - 7\ mm$ in lengths and 16 $\mu m - 70\ \mu m$ in diameters [9, 10, 11, 12]. An individual paper fiber bond is made of two crossed individual wood pulp fibers, and the angle between these two fibers is called a crossing angle, α. A fiber bond is the construction unit of a paper sheet which is a network of pulp fibers. Therefore, the fiber bonds and their strength and stiffness strongly contribute to the key parameters affecting the quality of paper sheets. Understanding parameters affecting the strength of bonds can lead to reducing the grammage of paper products and reducing the raw material consumption, consequently.

In 1933, it was suggested that the bond forms due to Laplace pressure inside a water bridge between two fibers [13]. In 1940, the challenges to measure the bond strength were stated as: "Fundamental measurements of this property are impossible because of such unmeasureable and uncontrollable variables as the formation of the sheets, the nature of the actual area tested, and the several fundamental stresses empirically applied in any one standard physical test" [14]. Despite of the scientific and technological achievements in the last decades, the aforementioned

challenges are still valid. During the sixties, structural aspects of bonding were explained [15], investigated using direct observation [16], and a theory was proposed for tensile strength of the paper [17].

It is suggested that there are six bonding mechanisms involved in forming a bond: mechanical interlocking of microfibrils, cellulose interdiffusion, hydrogen bonding, van der Waals bonding, Coulomb interaction [18] and capillary bridges [19]. Studies to identify quantitative properties and the role of the mentioned mechanisms through modeling have been reported [19, 20]. Even though the results of such atomistic models are scientifically valuable, these models not only require empirical measurements for validation, but also they must be scaled up to macro-scale in order to provide industrial impact. Therefore, there have been significant efforts to simulate static [21] and dynamic behavior [22, 23] of fiber networks, recently. Even though the models for simulation of fiber networks are well developed, experimentally acquired data on the mechanical properties of individual fibers and fiber bonds are still required to be used in these models. Therefore, measuring the bond breaking force directly is a necessity.

The challenges of measuring the bonding forces directly, are not only limited to finding an adequately accurate and sensitive force sensor but also to handling and mounting them. Manipulating and mounting the bonds in all of the reported methods are performed manually [24, 25, 26, 27]. In addition, specimen preparation in these studies is also done manually and without controlling the crossing angle, α, of the fibers. Crossing angle not only affects the bonded area [1] but also it affects the bond strength measurement. Non-perpendicular crossing angles lead to dividing the breaking force into two components which requires resolution of forces. Thus, either a two-axis force sensor is required or the resolution of forces should be carried out using simulation tools and a structural model of the bond [26].

In addition to the inhomogeneous nature of fibers and fiber bonds, as specimen preparation (bond making), handling and measuring a large number of bonds with current tools are difficult tasks, providing sta-

tistical reliable data is not possible [28]. Therefore, a large variation even within the same sample exists in the reported bonding forces [28]. Because of the aforementioned complications, paper fiber specialists still rely more on bond strength estimations on the hand-sheet level rather than on the individual level. Thus, to provide statistically reliable data, it is preferred to measure the energy required to break a certain number of bonds on the hand-sheet level instead of characterizing many individual bonds [29]. A lack of high throughput bonding force measurement tools is one of the main reasons for the tendency of paper fiber specialists to use tests on the hand-sheet level. They include static tests, e.g. Z-directional tensile test and shear cohesion test; and dynamic methods, e.g. Scott bond test [30]. Recent studies, however, on internal bond strength measurement methods on the hand-sheet level such as a peel cohesion test, a delamination test, a Z-directional tensile test, a cantilever beam test, a shear cohesion test and a Scott bond test prove that the results acquired with these methods contain undesirable information [30]. Even though the results of such tests on hand-sheets are highly correlated to the internal bond strength of paper/board, all of them include undesirable information in their results which are not decoupleable. For example: the Z-directional tensile test measures both intra- and inter-fiber bonding energies, the shear cohesion test couples the force required to shear the bond with the force acting on the plane of the sheet, and the dynamic nature of the Scott bond test overestimates the bond strength [30]. Therefore, the necessity of getting new information and data on bonds has increased during the recent years. The reported methods for paper fiber bond strength tests in individual bond level are either direct which are manual, laborious and have a low throughput or indirect which require data interpretation as well. These methods are explained in detail in Section 2.1.3.

In the following, the state-of-the-art on specimen preparation of micro-scale fibrous materials in general, fiber bonds (bond making) specifically, and bond characterization methods will be explained.

2.1.1 Specimen Preparation

Specimen preparation is a laborious and time consuming task which requires skilful and experienced personnel [31]. The specimen preparation techniques are categorized based on the mounting type to temporary or permanent, and based on the sample type to biological and non-biological [31]. Both biological and non-biological fibrous materials are of interest in such fields as unwoven materials, pulp and paper, composites, textiles, and optics. Not introducing artifacts and structural changes to the specimen in the specimen preparation processes of micro-scale fibrous materials is a challenging issue with prime importance [4]. The structural changes formed while handling the specimens are mainly caused by human error [4]. Robotic systems can reduce this damage whilst simultaneously increasing the handling throughput [4]. At macro-scale, robotic gripping techniques have been reviewed for use with fibrous material sheets [32]. At micro-scale, the issue is harder to tackle because of the aspect ratio of fibrous materials, which may be tenths of micrometers in diameter and only a few millimetres in length. While microrobotic technologies have been extensively utilized for microassembly [33, 34, 35, 36], handling micro- and nanoscale specimens such as carbon nanotubes (CNT)s [37, 38], optical fibers [39, 40, 41] and living cells [42, 43, 44, 45, 46, 47], their use in micro-scale specimen handling is rarely reported. Examples of using microrobotics for handling biological (e.g. single cells in aqueous media [48] and non-biological (e.g. individual tobermorite crystals for Atomic Force Microscopy studies [49]) samples exist; however, microrobotic systems for the specimen handling of micro-scale fibrous materials are not reported yet.

2.1.2 Bond Making Approaches

The real bonded area between two fibers is the area which is in molecular contact, and it might be detectable using high resolution nanotomography (NT). High resolution NT is a very slow imaging technique. Other methods such as imaging the sliced bonded area (destructive) [1] and measuring the apparent overlapping area between two fibers (non-

destructive) provide an acceptable estimate for the real bonded area [50]. The "apparent overlapping area" is also known as "optical bonded area" which is determined by optical microscopy. It has been shown that using this non-destructive approach results in 60% overestimation of real bonded area, which is the result of incomplete bonding of overlapping fiber regions [1]. Although the disadvantages of such non-destructive bond area estimation are very well known, it is still widely used because of its simplicity and accessibility. The data produced by this method are useful for relative comparison of various samples, but it is not recommended to be used for reporting absolute results.

Measuring the real bonded area is beyond the scope of this thesis. Hereafter, the term bonded area refers to the apparent overlapping area between two fibers. There are two important parameters in determining a bonded area, crossing angle, α, and vertical angle, β. The vertical angle is the angle between the fiber axis and the image plane. The crossing angle affects directly the bonded area [see Figure 2.1]. Equation 2.1 shows the relation between the crossing angle, α, with the calculated area of a fiber bond, A_{calc}:

$$A_{calc} = w1 \times w2 / sin(\alpha) \tag{2.1}$$

where $w1$ and $w2$ are the widths of individual fibers [1]. A common bond making approach is highly diluting the suspension of fibers and placing the droplets of suspension between two Teflon plates. Then the plates are dried for 45 minutes at $70°C$ [1]. The drying time and temperature might change from one laboratory to another, but the general process remains the same. The randomly oriented bonds in this method lead to random α and β angles which is shown in Figure 2.2A. Other examples of possible artifacts caused by this bond making method are illustrated in Figure 2.2B, C and D.

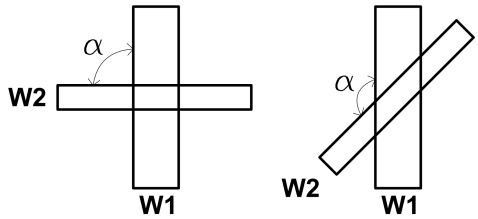

Figure 2.1: Crossing Angle (α) [1].

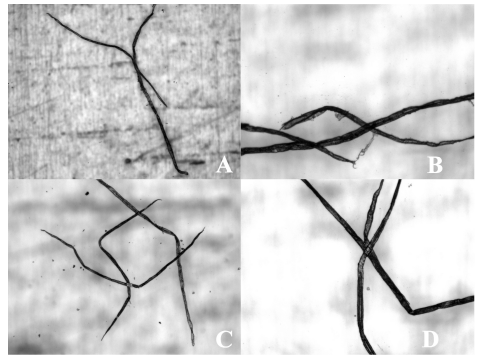

Figure 2.2: Artifacts caused by the conventional bond making method approach. A) Random (α & β) angles, B & C) More than one bond on one fiber, D) Two bonds on the top of each other [2].

2.1.3 Bond Characterization Methods

It is possible to categorize bond strength measurement methods into direct and indirect methods. Indirect methods are either experimental which are mainly correlating bonded area with bond strength, or they are based on modeling [19, 20]. A typical approach to determine the apparent bonded area is using polarized light microscopy [16] and microtome serial sectioning combined with image analysis [1]. This method provides information only on optically bonded area which is not representing the real bonded area. Since the latter method is a destructive measurement method, it is not possible to correlate the real bonded area to the bond strength. In the quest to find the real bonded area, the most recent and the most accurate method is using NT. The

main drawback of nanotomography is the longer scanning times, which makes it an inefficient method for providing statistical data.

In order to understand the mechanical properties of bonds, they have to be characterized in different loading modes. The loading modes for bond strength measurement are as follows: shear or sliding mode, Z-directional or opening mode, torsional or tearing mode [51], and peeling mode [52] [See 2.3].

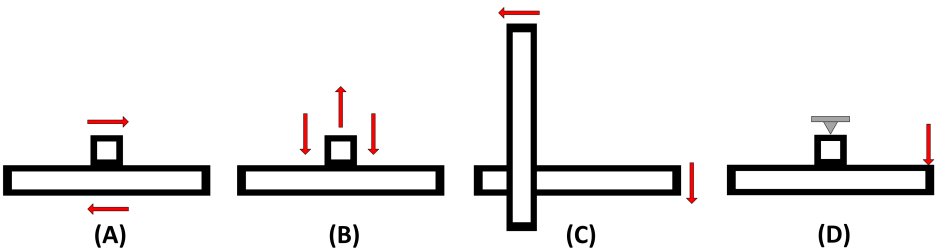

Figure 2.3: Different modes of fiber bond loading. A) Shear or sliding mode; B) Z-directional or opening mode; C) Torsional or tearing mode; D) Peeling mode [3].

Bond strength measurement dates back to the sixties [53]; in 1962, a modified chainomatic balance was used for measuring the shear strength, and cement was used to mount the bonds to the specimen holder [50]. In 1964, an Instron tensile tester was used for measuring the shear strength, and double-sided adhesive tape was used for mounting the bonds [54]. In 1990, the second generation of a load-elongation recorder developed by Hardacker in 1962 [55], was used to measure the bond strength, and Epon 907 resin and hot melt was used to mount bonds [24]. In 2011, a modified atomic force microscope (AFM) probe was used to measure the strength in the peeling mode [25]. In the same year, an Instron ElectroPulse E1000 electrodynamic tensile testing machine equipped with a Honywell Sensotec 50 g load cell was used to measure the bond strength [26]; the bonds were mounted on specimen holders using glue. In order to estimate the state of loading in normal and shear direction, by using the imaged geometry of each bond, a structural model of the bond was analyzed [26]. In 2013, a calibrated AFM probe was used, the same method as in [25], to measure the bond under

static and dynamic loading, and also the formerly bonded areas were investigated to study the effect of mechanical interlocking as a bonding mechanism [27]. Table 2.1 summarizes the reported bond strength measurement methods.

Table 2.1: List of reported bond strength measurement methods.

Year	Measurment Device	Mode	Mounting Method
1962 [50]	Modified Chainomatic Balance	Sliding	Cement
1964 [54]	Instron Tensile Tester	Sliding	Adhesive Tape
1990 [24]	IPC Load-Elongation Recorder	Sliding	Epon 907 Resin
2011 [25]	Modified AFM probe	Peeling	Nail-Polish
2011 [26]	Instron ElectroPulse E1000 & Honywell Sensotec 50 *g* load cell	Sliding & Tearing	Glue
2013 [27]	Calibrated AFM probe	Peeling	Nail-Polish

The aforementioned bond characterization methods is not a complete list. In order to study these methods further, reading the following references are recommended [56, 57, 58, 59].

2.2 Micro-Tensile Testing

Micro-tensile testers are required mainly in two application areas: characterizing materials and components used for fabricating microelectromechanical systems (MEMS) [60, 61, 62, 63], and characterizing micro-scale specimens of various materials [64, 65] such as micro-scale fibers [66, 67, 26, 68]. The devices used for micro-tensile testing are divided in three categories: commercialized universal micro-testing machines which use load cells e.g. Instron 5848 [63, 69]; AFMs with special cantilevers [66, 68, 70], and micro-tensile testers developed for specific application areas by utilizing micro-electro-mechanical technologies [61, 64, 65, 71, 72, 73, 74, 75, 76]. On the one hand, universal micro-testing machines and their gripping devices are mainly used for standard test methods and they are difficult to apply in testing thin films [74]. On the other hand, AFM based micro-tensile testing techniques are limited in their force range and they are slow. Therefore, many research groups fabricate their own micro-tensile testers which belong

to the third aforementioned category. An interferometric strain/displacement measurement system, which measures the strain using a laser sensor and measures the force using a load cell, was developed in National Aeronautics and Space Administration (NASA) and reported in 1989 [71]. This system was improved by using air bearings to eliminate friction in the loading system in 1997 [72]. In this system, a piezoelectric transducer was used to apply the load on the specimen and a load cell with 5 mN resolution and 2.2 N range was used to measure the force [72]. In 2001, heat resistive grippers and a new load cell, with 90 N range and 200 mN resolution, were integrated into the platform, allowing high-temperate micro-sample testing [73]. Another load cell based micro-tensile tester, which was used for in-situ AFM measurements, was reported in 2006 [76]. The reported resolution for this device was 125 mN for the force range of 25 N [76]. Besides commonly used load cells, other technologies have been developed for high resolution micro-tensile testing. A micro-tensile testing system, for sub-micrometer thick films, was developed using a servo controlled balance with 100 mN force range and 1μN resolution [61]. In order to measure the tensile strength of free standing thin films, an eddy-current displacement sensor and two steel flex stripes were used to fabricate a micro-tensile tester with 12 mN force range [74]. In another approach, micro-tensile testers utilizing a bender as the force sensing component were also reported; e.g. a silicon beam bender for studying the micromechanics of polymers [64] and a deflectable pipette for viscoelastic analysis of muscle cells [65]. In order to characterize the material properties of nanostructures, e.g. nanowires, a tensile testing system for in-situ electron microscopy strength measurements was developed [75]. This system consists of an electrostatic comb drive actuator for loading the specimen and a thermal actuator for displacement control. A differential capacitive comb structure was integrated into the system as the force sensing component with the resolution of 12 nN and the force range of 1.5 mN [75].

2.3 Force Sensing Microgrippers

In recent decades, many microgrippers have been developed either for various micromanipulation tasks or mechanical characterization of micro-scale objects. The microgrippers can be categorized into three types: (i) microgrippers without force sensing features; (ii) microgrippers capable of gripping force measurement; (iii) microgrippers capable of tensile force measurement.

2.3.1 Microgrippers without Force Sensing Features

Pioneers such as Fukuda were studying microgrippers since 1987 [77]. One of the first cases that reported the design, fabrication and testing process of a typical microgripper was at the Berkeley Sensor and Actuator Center in 1990 [78, 79]. The mentioned on-wafer PolySilicon microgripper with 10 μm gripping range was actuated electrostatically [78, 79, 80]. Later, a monolithic overhanging microgripper was developed with enhanced micromanipulation features [81]. Other microgrippers such as an SMA microgripper with antagonistic actuator and an integrated gear mechanism [82], an electrothermally actuated polysilicon microgripper to manipulate CNTs [83] and a two-degrees-of-freedom piezoactuated microgripper for micromanipulation tasks [84] were only capable of grasping micro-scale objects without any force sensing feature.

2.3.2 Microgrippers Capable of Gripping Force Measurement

Since micro-scale objects, especially biological samples, are extremely sensitive to the applied forces during manipulation, many microgrippers equipped with an integrated gripping force sensor have been developed and reported in recent years. For example, a monolithic compliant piezoelectric-driven microgripper with integrated gripping force sensor and an integrated tip displacement sensor has been developed using

a pseudorigid-body-model method [85]; a superelastic NiTi microgripper with embedded miniaturized voice coil actuators and piezoelectric PVDF force sensors has been reported [86, 87]; a silicon electrothermal microgripper integrated with two-axis capacitive force sensors, one axis dedicated to contact detection and another one for gripping force measurement, was developed for mechanical characterization of microcapsules [88]; piezoresistive cantilever beams were integrated to an electrothermal microgripper to measure the gripping force [89]. Another well studied type of microgrippers which have an integrated gripping force sensor are electrostatic grippers; they are using a lateral comb drive system for actuation and a transverse comb drive system to sense the gripping force [90, 91]. Some of these microgrippers such as FT-G microgripper series (FemtoTools AG, Switzerland) have already been commercialized [91].

2.3.3 Microgrippers Capable of Tensile Force Measurement

Even though microgrippers with integrated gripping force sensors are widely reported, successful studies on microgrippers capable of micro-tensile testing are rare. Examples include SU-8 based electrothermal micro-gripper integrated with an optical fiber displacement sensor for micro-tensile testing of biological samples [92], and an electrostatically actuated monolithically integrated two-axis micro tensile-tester for the force range of $\pm 60\ \mu N$ which includes a two-axis capacitive force sensor and a capacitive position sensor [93]. Electrostatically actuated microgrippers are compact and easy to fabricate with MEMS fabrication processes but they have a very limited force range. In Chapter 4 of this thesis, novel solutions for microgrippers capable of tensile force measurement are presented.

2.4 Polyvinylidene Fluoride Film Sensors

Polyvinylidene fluoride (PVDF) is a piezoelectric polymer material having a solid and homogenous structure [94] which was discovered by Kawai in 1969 [95]. Similar to other piezoelectric materials, such as PZT (Lead Zirconate Titanate), an electrical signal is induced in the electrodes when an external force is applied on PVDF. This is called direct piezoelectric effect with the following constitutive equation in which electric field and stress are the independent variables:

$$D_k = d_{kij}\sigma_{ij} + \epsilon^{\sigma}_{km}E_m \tag{2.2}$$

where D_k is dielectric displacement, d_{kij} is piezoelectric coefficient, σ_{ij} is stress, ϵ^{σ}_{km} is permittivity and E_m is electric field. The converse piezoelectric effect is expressed by the following constitutive equation:

$$S_{ij} = c^{E}_{ijkl}\sigma_{kl} + d_{kij}E_m \tag{2.3}$$

where S_{ij} is strain and c^{E}_{ijkl} is elastic compliance.

The charge sensitivity of a piezoelectric material is characterized by its piezoelectric coefficients d_{kij}, which are defined for each direction of the generated electrical field, $i = 1, 2, 3$, and the direction of the affecting force, $j = 1, 2, \ldots, 6$, [96].

The d_{kij} is a third-rank tensor expressed in terms of 3×6 matrix, however, crystal symmetry reduces the number of independent piezoelectric

coefficients [97]:

$$d_{kij} = \begin{pmatrix} 0 & 0 & 0 & 0 & d_{15} & 0 \\ 0 & 0 & 0 & d_{24} & 0 & 0 \\ d_{31} & d_{32} & d_{33} & 0 & 0 & 0 \end{pmatrix} \tag{2.4}$$

For PVDF films the electrical axis, i is always 3 since the electrodes are at the top and bottom of the film. For the mechanical axis, j can be 1, 2 or 3 since the stress can be applied to any of these axes. The polarization of PVDF is oriented in the manufacturing phase by stretching the film and poling it under a strong electric field [98].

In recent years, PVDF has been used for various force sensing applications. PVDF sensors for sensing micro-Newton forces were integrated with a commercial micromanipulator and their force sensing abilities were demonstrated in 1D and 2D sensing systems [99]. A PVDF film with upto $20mN$ force range for cellular force measurement in biomanipulation application [100], and a sensorized microgripper based on PVDF film sensor for forces up to $6mN$, for alignment of micro-opto-electrical components was developed [87]. In addition, high sensitivity PVDF force sensors with a resolution in the range of sub-μN for micro-assembly [101] and micromanipulation [102] applications have been reported. In another application, in order to detect cell injection forces PVDF sensors have been utilized [103, 104]. PVDF sensors were also used for micro-force tracking systems [105]. Due to the high resolution and fast response, PVDF is a suitable solution for micro-force sensing applications.

2.5 Electroplated Nickel

MEMS structures such as inertial switches [106] and vibration energy harvesters [107] are widely fabricated from Electroplated Nickel (ElNi) using LIGA processes. LIGA is a German acronym for “Lithographie”

(Lithography), “Galvanoformung” (Electroplating), “Abformung” (Molding). Therefore, factors affecting mechanical properties of ElNi [108, 109, 60], such as plating conditions [110, 111], have been studied during the last decade. Young’s modulus is the most important mechanical property of ElNi which has been studied using the following two categories of techniques: dynamic techniques such as analysis of vibration frequencies of free-clamped microcantilevers [108, 112], and static techniques such as beam bending [113, 114], bulging of membranes [113], indentation [108], tensile test [60], and balance method [115]. Studies show that plating temperature and current density are the major factors influencing the Young’s modulus of ElNi [110]. It is possible to adjust the Young’s modulus of the final fabricated product in the range of $85GPa$ – $205GPa$ by controlling plating temperature and current density [110].

An exemplary fabrication process of ElNi structures using LIGA is illustrated in Figure 2.4 [7]. First, a Cr/Cu layer is sputtered on a Si wafer (Figure 2.4A), then positive photoresist e.g. AZ®50XT is spun on the Cr/Cu layer to the height of e.g. $50\mu m$ (Figure 2.4B). Next, using a mask and the UV-lithography process trenches are made in the photoresist (Figure 2.4C). The nickel specimen layer is electroplated in $50°C$ with a current density of $10mA/cm^2$ to the desired height of $50\mu m$ (Figure 2.4D); the main composition of electroplating solution is nickel sulfamate Ni(NH2SO3)2.6H2O with pH of 3.9. After electroplating, the positive photoresist is removed using NaOH solution (Figure 2.4E), and the Cr/Cu layer is back-etched using NH3.H2O.H2O2 solution (Figure 2.4F) [7].

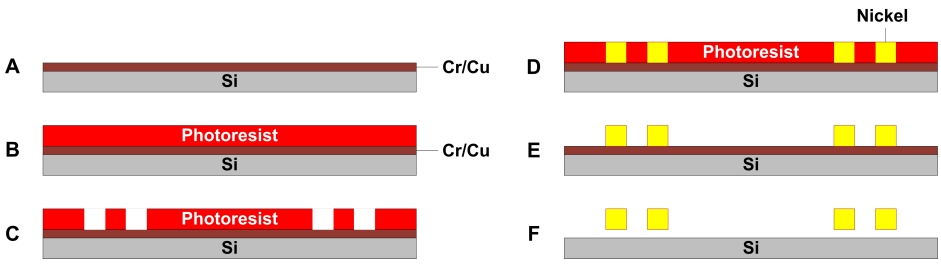

Figure 2.4: Fabrication process of ElNi microspring.

The type of lithography process, e.g. UV or X-ray, and the type of photoresist, positive or negative, varies depending on the final product quality and requirements. The UV-lithography is usually used for structures with heights smaller than $100\mu m$ while X-ray lithography is used for structures with heights larger than 100 μm. Negative photoresists usually provide better side-wall quality compared to positive photoresists.

2.6 Beyond State-of-the-Art

This thesis aims to elevate the state-of-the-art in characterization of micro-scale fibrous materials by introducing the following novelties:

- A microrobotic platform for manipulation and specimen preparation of micro-scale fibrous materials for microscopic studies, e.g. scanning electron microscopy (SEM) and NT, is designed and developed. This microrobotic platform minimizes the human interaction with the specimens while decreasing the specimen preparation time [4]. Using the developed microrobotic platform, not only the traditional manual bond making method based on Teflon-plates is enhanced with a robotic one [2], but also perpendicular bonds, instead of randomly formed bonds, were made and measured for the first time [5].

- Tensile testing of micro-scale fibrous materials does not need a lot of force to manipulate but their ultimate tensile strength is very high and relatively large forces are required to perform a micro-scale tensile test, e.g. CNTs require $0.5mN$ – $30mN$ [116, 117], wood fibers require $40mN$ – $370mN$ [118] and paper fiber bonds require $0.2mN$ – $20mN$ [5, 24, 6]. This thesis proposes a novel force sensing approach for grippers used in micro-tensile testing applications.

- Use of ElNi microsprings based force sensor for micro-tensile testing applications is a new approach compared with the other approaches reported in the literature such as load cells [71, 72, 73],

servo controlled balance [61] and eddy-current based force sensors [74]. Even though design and fabrication of S-shape and U-shape ElNi springs for testing micro-scale thin films were already reported in [119], the use of ElNi MEMS structures for force sensing applications has not been reported. For the first time, in this thesis, an elliptical ElNi microspring is designed, fabricated and integrated into a low-friction precision linear slider (PLS) for force sensing applications [7].

- The equipment for Z-directional testing at the hand-sheet level is very well developed and there are several commercial devices and methods [120] available to perform such tests, including the Lab Master® Z-direction tensile tester (Testing Machines, Inc., USA) and the L&W Z-direction tensile tester (Lorentzen & Wettre, Sweden). However, there is no device available in the market, or even reported in the literature, which is capable of measuring the Z-directional breaking forces of bonds. A novel method for the measurement of Z-directional individual bond breaking forces, using a PVDF sensor which is operating in a cantilever-like bending mode is presented in this thesis [3].

3 Microrobotic Platform for Specimen Preparation

This chapter introduces a modular tele-operated microrobotic platform to address the challenges of handling and specimen preparation of micro-scale fibers. The modularity of the platform allows a promptly adaptable reconfiguration to match the needs of various specimen handling and preparation techniques. Design and implementation of the microrobotic platform is presented in Section 3.1. Then the performance of the platform is demonstrated by accomplishing the following tasks: preparing samples for scanning electron microscopy and nanotomography, described in Section 3.2; making individual bonds using the microrobotic platform, described in Section 3.3; making perpendicular bonds using the microrobotic platform, described in Section 3.4.

3.1 Design and Implementation

Since micro-scale fibers cover a wide range of dimensions, the platform should be able to handle fibers with diameters ranging from 10 μm to 1000 μm and lengths of a few millimeters. Another important factor is the ambient conditions of the sample. Due to hygroscopic properties of pulp and paper fibers, the standard ambient conditions for pulp and paper studies are $50\% \pm 2\%$ relative humidity and $23 \pm 1\,^{\circ}C$ temperature.

Since initially many fibers are suspended in an aqueous medium (e.g. pulp fibers in water), the platform should be able to handle specimens in both wet and dry conditions. Furthermore, in their initial state, fibers are not aligned and have a random orientation, so the platform requires an alignment process to orient the samples. Other steps in the handling process are to separate, pick, sort and mount the fibers on specimen holders. In many sample preparation cases, it is also necessary to treat the sample chemically by adding a known volume of different chemicals [121]. The platform should be able to chemically treat the fibers individually and depending on the dimensions of the fiber, the platform should be able to generate known volumes of chemicals in the nano-liter to micro-liter scale, and dispense the droplet accurately on the desired place. The high aspect ratio of fibers requires the handling of samples in three dimensions. Therefore, the platform should be capable of operating not only in 2D but also in 3D. As different microscopy tools have different types of specimen holders, the platform should be modular and be able to mount the fiber on different types of specimen holders. Since specimen handling of micro-scale fibers is a laborious and time consuming task, the platform should be designed so that it can be automated in applications where high throughput is essential. The architecture of the platform is shown in Figure 3.1.

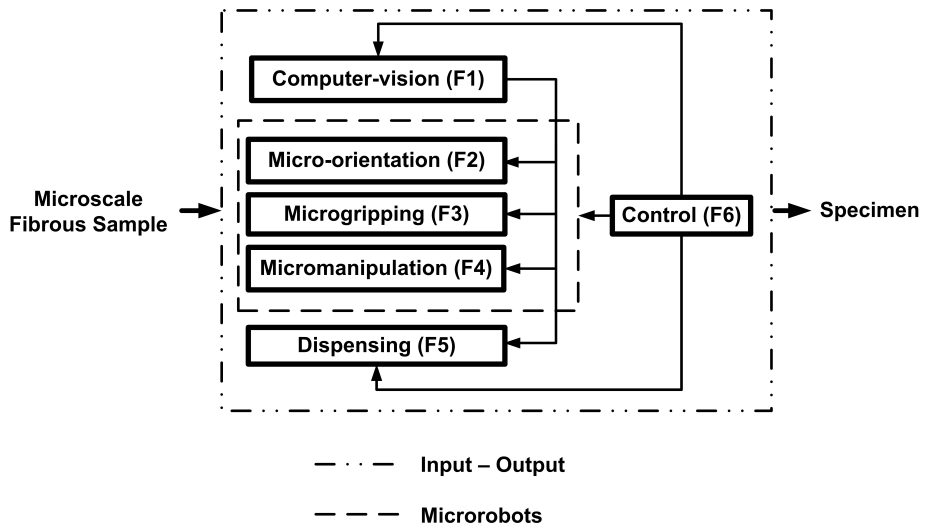

Figure 3.1: Main functions of the microrobotic platform [4].

To fulfill the aforementioned tasks the following functions are required: the computer-vision function (F1) identifies the fiber; the micro-orientation function (F2) aligns the fiber; the micro-gripping function (F3) grasps the fiber; and the micromanipulation function (F4) handles and mounts the fiber on a specimen holder. When necessary, a dispensing function (F5) treats the individual fiber chemically. The control function (F6) orchestrates the other functions and provides a user-interface for the operator.

Figure 3.2 and Figure 3.3 show the design of the platform and Figure 3.4 depicts the implementation of the platform. The same numbering method is used in Figure 3.2 and Figure 3.4. Hereafter, the components in the figures are labeled "C.#-F.#", which refers to "Component Number-Figure Number". The stacked gantry crane structure provides several benefits such as having the most compact design without coordinate mapping and with fixed cameras. This structure holds three micromanipulators (C.1-F.3.2, C.2-F.3.2 and C.3-F.3.2) and an XY-table (C.6-F.3.2). The micromanipulators are composed of three similar linear actuators (SmarAct GmbH, Oldenburg, Germany) which provide a 100 nm resolution, a ± 10 μm absolute accuracy, a ± 1 μm repeatability and a 21 mm travel in X, Y and Z directions. Two micromanipulators (C.1-F.3.2 and C.2-F.3.2) are equipped with microgrippers, and the third manipulator (C.3-F.3.2) is equipped with a probe. A linear actuator is added to one of the micromanipulators with a microgripper (C.1-F.3.2) to move a dispenser (C.4-F.3.2) which is used for the chemical treatment of the samples. The micropositioner C.4-F.3.2 facilitates the application of droplets down to 70 nl with the dispenser (TheLee Co., LA, USA) on any chosen location. A rotary-table (C.5-F.3.2) with a resolution of 10 μ° is mounted on the XY-table for orienting and aligning the samples. A holder for the samples and a holder for the finished specimen are integrated onto the top of a rotary-table. The sample holder is a small container which holds the samples either in a dry or a wet state. The specimen holder is an SEM stub, or a scanning tunneling microscopy (STM) probe which is used as a specimen holder in NT. The microgrippers attached to micromanipulators (C.1-F.3.2 and C.2-F.3.2) are tailored for that purpose and have exchangeable jaws with an opening gap of

1 mm (SmarAct GmbH, Oldenburg, Germany). The probe attached to the third micromanipulator (C.3-F.3.2) is a stainless-steel probe fabricated using laser-micro-machining. Figure 3.3 shows the design of the mounting probe. The tip of the probe is designed in such a way that it allows the mounting of fiber on both horizontal and inclined specimen holders. The 300 μm horizontal edge on the tip is used for mounting the fiber on horizontal specimen holders, and the inclined 707 μm edge with the 45 ° angle is used for mounting on inclined specimen holders.

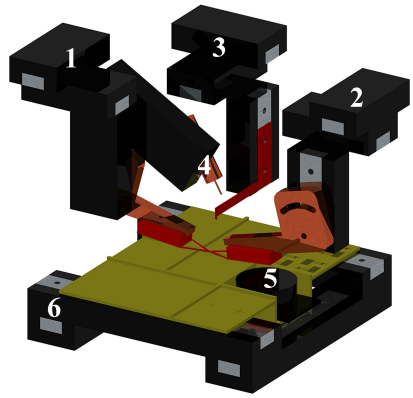

Figure 3.2: Design of the microrobotic platform for handling individual fibers and bonds. (1 and 2) XYZ-micromanipulators with active microgrippers; (3) XYZ-micromanipulator with a probe; (4) Solenoid-dispenser; (5) microrotary-table and (6) XY-table [4].

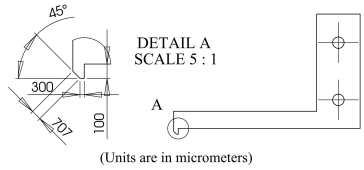

Figure 3.3: The design of the self-fabricated mounting probe and its tip [4]. © *John Wiley and Sons* Reprinted, with permission, from [P. Saketi, et al., A flexible microrobotic platform for handling micro-scale specimens of fibrous materials for microscopic studies, 10/2012].

All micromanipulators, with the exception of the dispenser micromanipulator, are equipped with position sensors. The dispenser micromanipulator and the rotary-table are controlled using visual feedback. A

12× computer-controlled zoom with 0.29 × −3.5× magnification, a fine focus and an illumination system (Navitar Inc, Rochester, NY, USA) and a CCD camera (SONY XCD-U100) provide visual feedback from the top. A 6× macro–zoom-lens (Optem, Munich, Germany) and CCD camera (SONY XCD-X710) provide the side view. The pixel sizes of the top-view and side-view cameras are 4.4 μm and 4.65 μm, respectively. Figure 3.4 shows the configuration and the modular features of the microrobotic platform; numbering is as in Figure 3.2. The modularity of the platform eases the configuration of various samples and sample holders. The first configuration of the platform [Figure 3.4A] is designed to handle specimens of fibers for SEM imaging. The sample container is a stainless steel dish with a depth of 100 μm. This depth guarantees that the fibers cannot stay inclined in the medium and that they are graspable with the microgrippers. In this configuration, the specimen holder is an SEM stub in the center of the rotary-table which is available in various inclination angles and can be easily changed depending on the imaging needs [Figure 3.4B]. The second configuration of the platform is designed to handle specimens for NT imaging [Figure 3.4C]. The depth of the sample container is 100 μm – the same as in the first configuration. An STM probe is used as the specimen holder for NT imaging. It is attached to the rotary-table to align the sample with the probe.

The control software's main responsibility is to provide the functionality to control the devices in the platform. In addition, it acquires data from sensors and cameras and it also provides a user interface for the operator. In a typical scenario, the operator places the fiber in the sample container and visually inspects the fibers via the provided user interface. The operator is responsible for selecting the best fiber. In the next phase, the operator aligns the selected fiber with microgrippers using the rotary-table and moves the microgrippers to the proximity of the end points of the fiber. The selected fiber is grasped by closing both gripper jaws synchronously. After the fiber is successfully grasped, it is moved onto the specimen holder and aligned appropriately. Finally, the fiber is mounted on the specimen holder using the probe. Figure 3.5 illustrates the signal flow diagram in control software during the tele-operated specimen handling processes.

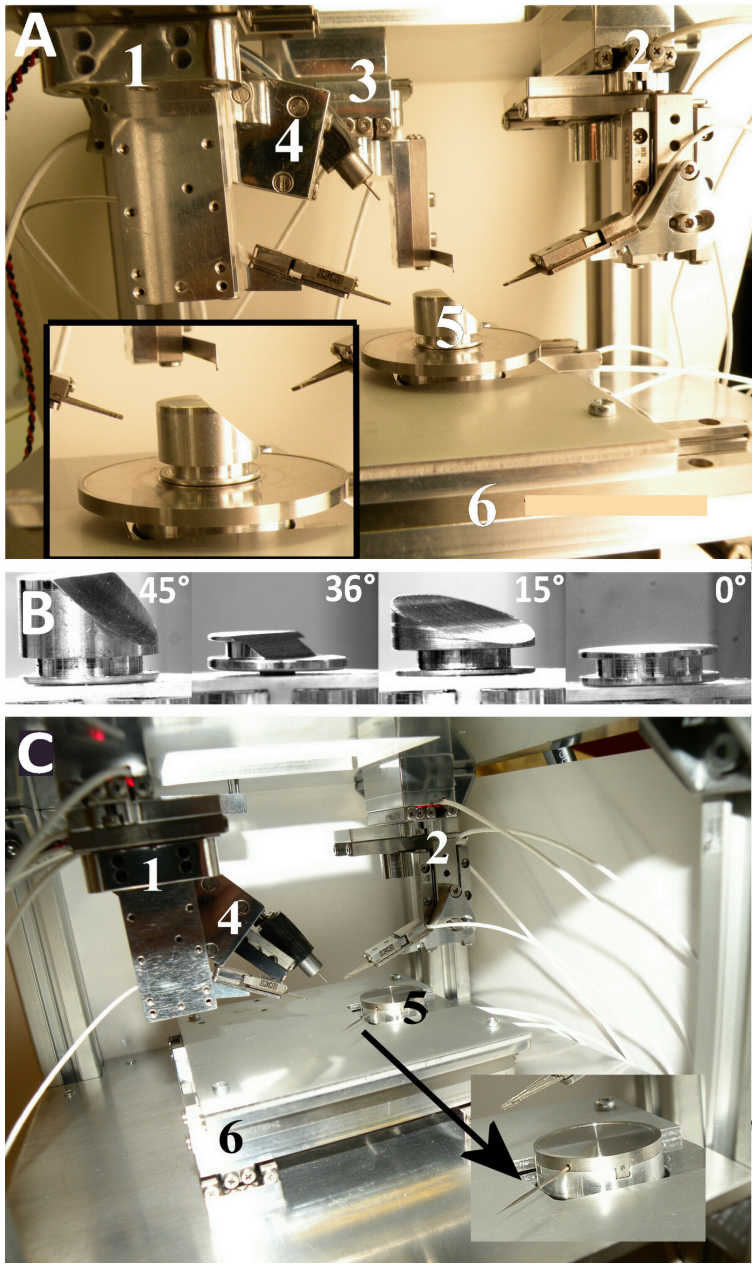

Figure 3.4: The configuration of the platform (numbering is as in Figure 3.2). (A) The platform configuration for the specimen handling of fiber for SEM imaging. (B) Stubs with varying inclination: 0 °, 15 °, 36 °, and 45 °, all with a diameter of 12.5 mm. (C) The platform configuration for the specimen handling of fiber for NT imaging [4]. © *John Wiley and Sons* Reprinted, with permission, from [P. Saketi, et al., A flexible microrobotic platform for handling micro-scale specimens of fibrous materials for microscopic studies, 10/2012].

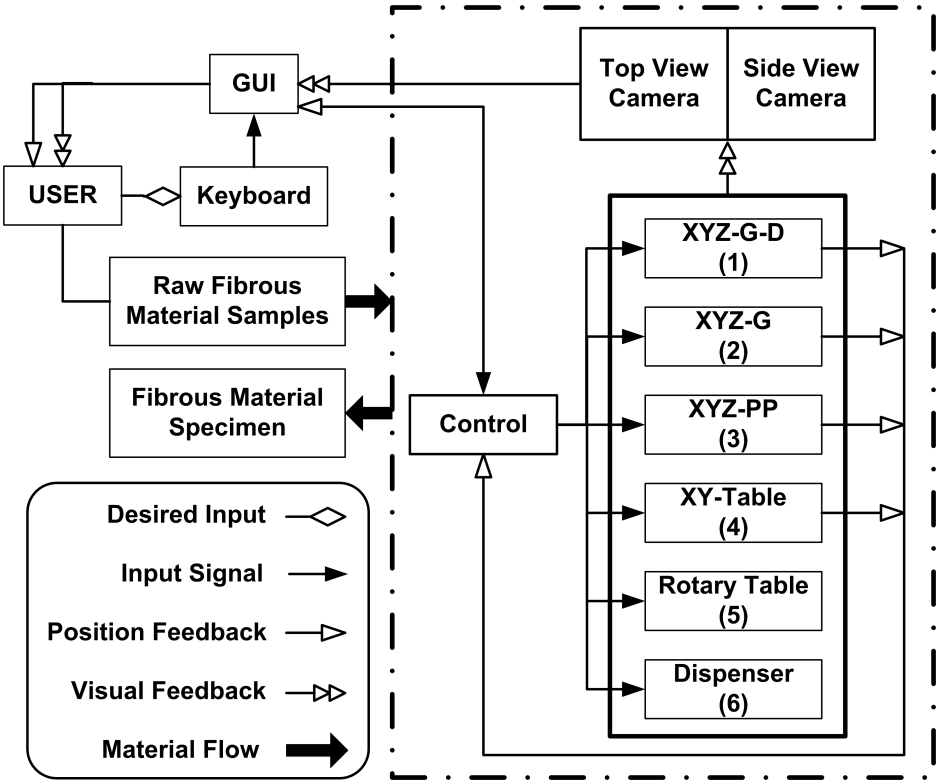

Figure 3.5: Signal flow diagram during the specimen handling processes. XYZ: The 3DOF micromanipulator; G: including microgripper; D: including dispenser positioner; PP: including Probe [4].

3.2 Preparing Samples for Scanning Electron Microscopy and Nanotomography

To image small specimens with an SEM, the specimens are generally placed on carriers referred to as stubs. These carriers are available in different sizes and materials, such as aluminium or copper (Agar Scientific, UK). Stubs with a diameter of 12.5 mm and a varying inclination angle (0 °, 15 °, 36 °, and 45 °, [Figure 3.4B]) were used for the experiments. The inclined stubs ease the approach to the fibers with microrobots inside the SEM. To mount the paper fibers on the stubs, two pieces of adhesive carbon pad are fixed onto the stub surface. Since paper fibers are natural fibers with largely varying lengths, the pads form a narrowing groove, in the shape of a "V". This "V" shape groove guarantees that fibers with different lengths can be mounted.

Figure 3.6 illustrates the process of specimen preparation for a diagonal compression test of a paper fiber inside an SEM. The fibers in this experiment are refined bleached pine kraft pulp fibers which are disintegrated in deionized water and placed on the rotary-table by using a pipette. To mount both ends of a fiber on the edges of the "V" shape groove, two microgrippers grasp an individual paper fiber at both ends and lift it above the rotary-table to a suitable height so that the stub can move under it (Figure 3.6A & B). Then, the paper fiber is aligned with the "V" shape groove to match its length. The alignment process is a combination of fine movements with the rotary-table and the XY-table (Figure 3.6C). To increase the accuracy of mounting, the mounting probe pushes one end of the grasped fiber – very close to the microgripper – to the carbon pad while holding both ends of the fiber with the microgrippers (Figure 3.6D). The same process is repeated for mounting the other end of the fiber onto the carbon pad (Figure 3.6E). Finally, the microgrippers release the fiber ends after the mounting process is over (Figure 3.6F). The process is repeated for mounting several fibers on differently inclined stubs. The paper fibers ranged from 25 μm – 34 μm in diameter and 0.8 mm – 3 mm in length.

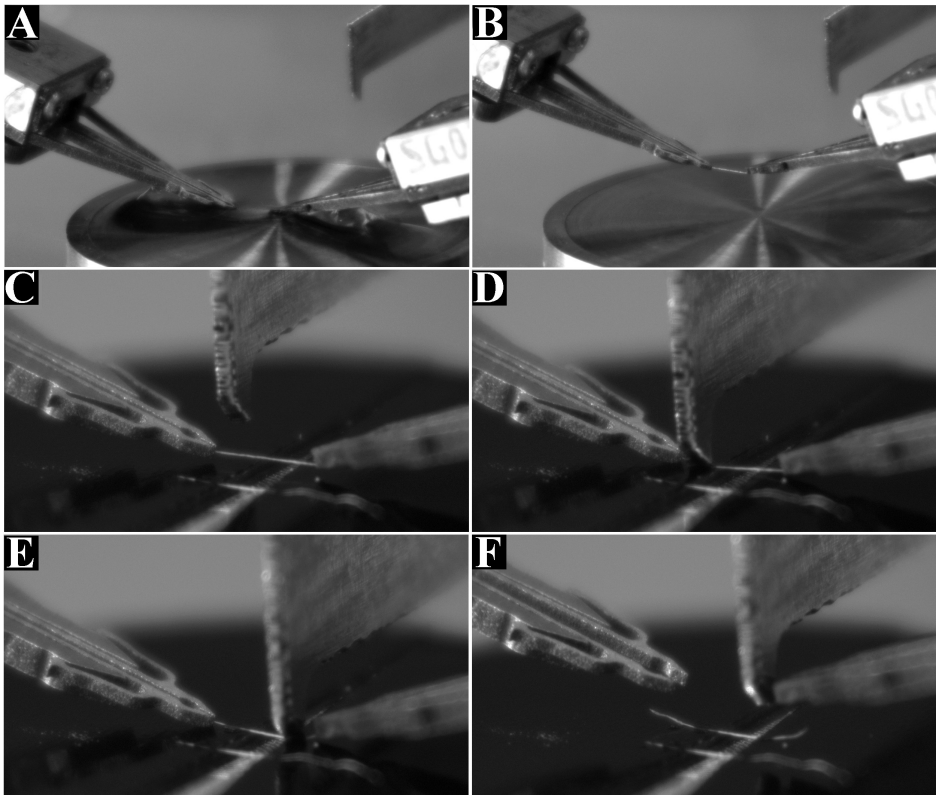

Figure 3.6: The process of paper fiber specimen preparation for the diagonal compression test inside an SEM. (A & B) Two microgrippers grasp an individual paper fiber at both ends and lift it above the rotary-table to a suitable height so that the stub can move under it; (C) The paper fiber is aligned with the "V" shape groove of the carbon pad to match its length; (D & E) The mounting probe pushes one end of the grasped fiber at a time – very close to the microgripper – to the carbon pad while holding the both ends of the fiber with the microgrippers; (F) The microgrippers release the fiber ends after the mounting process is over. [4] © *John Wiley and Sons* Reprinted, with permission, from [P. Saketi, et al., A flexible microrobotic platform for handling micro-scale specimens of fibrous materials for microscopic studies, 10/2012].

In the NT studies, an STM tungsten probe was used as the sample holder for a strand of human hair and also for an individual paper fiber bond. Figure 3.7 shows the process of handling a strand of human hair with a diameter of 142 μm for NT. The microgripper grasped the human hair in a dry state from the rotary-table and aligned it both vertically and horizontally with the STM probe (Figure 3.7A & C). The coordinates of the

rotary-table are saved. The rotary-table turned the STM probe, dipped it in glue and returned it back to the saved coordinates. Finally, the microgripper moved the hair fiber close to the STM probe for mounting (Figure 3.7B & D). Individual paper fiber bonds are delicate samples to manipulate – they require approximately 1 mN - 20 mN to break – and they exhibit a more complex shape than single fibers. Figure 3.8 shows the process of the specimen handling of an individual paper fiber bond for nanotomography. The process steps are similar to the handling of the human hair.

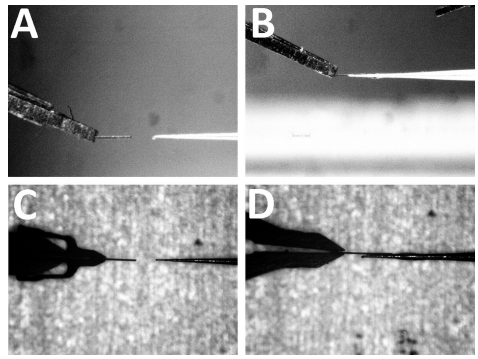

Figure 3.7: The process of handling human hair for NT studies. (A & B) side view; (C & D) top view. The diameter of the hair sample is 142 μm [4].

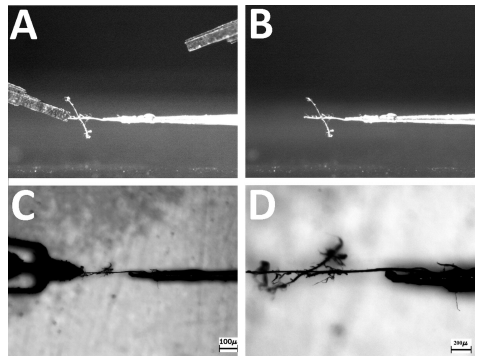

Figure 3.8: The process of specimen handling for NT studies of individual paper fiber bonds. (A & B) side view. (C & D) top view [4].

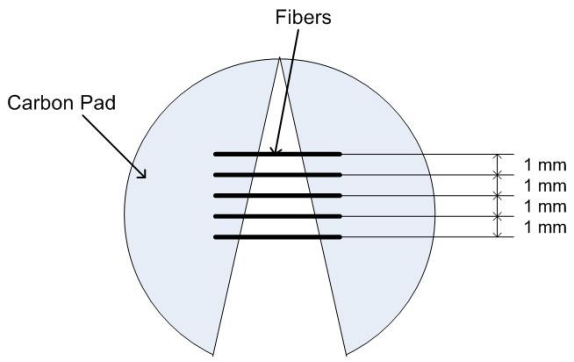

Figure 3.9: Schematic of reference paper fiber mounting task to compare the skilled worker accuracy and speed with the microrobotic platform quantitatively [4].

To compare the precision and speed of mounting the fibers using the microrobotic platform with manual work of a skilled worker quantitatively, the following task was defined and performed: Five fibers were mounted on a stub with the distance of 1 mm from each other as illustrated in Figure 3.9, and it was repeated four times. The process of mounting paper fibers on SEM stubs using microrobotic platform was already mentioned in the beginning of this section [see Figure 3.6]. The consumed time to perform the assigned task using the microrobotic platform was calculated from the time stamps of the sequence of images recorded during the process. The average time to picking up a paper fiber from the diluted pulp suspension was 67 s per fiber (Figure 3.6A & B). The main challenge in picking up the suspended individual paper fibers from water was the shadows cause by the water meniscus around the microgripper jaws; Figure 3.6A illustrates this problem. These shadows complicate the detection of paper fiber endpoints in the top-view when the microgrippers are inside the water. The average time to perform the fiber alignment and position the fibers in the requested distances from each other needs the average time of about 28s per fiber (Figure 3.6C). The required time to mount the both ends of a fiber, open the microgrippers and lift them was 75s (Figure 3.6D, E & F). Therefore, the average time for the entire process was 170s per fiber. The total required time to perform the assigned task of mounting five fibers on each stub using the

microrobotic platform was about 14 minutes per stub. A skilled laboratory worker performed the aforementioned assigned task manually to compare the results with the microrobotic approach. The manual paper fiber mounting steps are as follows: disintegrating the paper fibers; diluting a drop of concentrated fiber slurry in a Petri dish; putting a drop of water on a microscope glass slide; taking single fibers from the Petri dish which seem to be long enough using tweezers (Dumoxel non-magnetic, size 5) and placing them into the water droplet on the glass slide by naked eyes. Then taking the first fiber with the tweezers from the glass slide and bring it to the stub; positioning the fiber to match the width of the "V" shape groove on the carbon pad, and pressing one fiber end onto the carbon pad using the tip of the tweezers. Positioning the other fiber end using a stereo microscope and mounting it using the tweezers. The same process is repeated for the next four fibers. The most time consuming part of the process was to separate the individual paper fibers from disintegrated fibers; grasping and mounting them on the stub was less time consuming after the training. Excluding the required time to separate the individual fibers from the disintegrated fibers, the learning curve showed that preparing the first stub took about 20 minutes, but the time was reduced to approximately 7 minutes for the last stub. The entire process of mounting 20 fibers on four stubs (five fibers per stub) took approximately 80 minutes. The total required time to perform the assigned task of mounting five fibers on each stub manually was about 20 minutes per stub.

Figure 3.10 shows the representative SEM images of individual paper fibers mounted on the stubs. The images in the top row of Figure 3.10 show the individual paper fibers mounted manually (Figure 3.10M1, M2 & M3), and the images in the bottom row show the individual paper fibers mounted using the microrobotic platform (Figure 3.10R1, R2 & R3). The following four parameters are taken into account in order to compare the results of the manual approach with the microrobotic approach: time, gap between the fibers (Figure 3.10M2 & R2), angle between the fibers (Figure 3.10M3 & R3) and curliness of the fibers. Here, the curliness is defined as the broadest distance the fiber covers in the lateral direction, which is an indicator of the real curliness

correlated with the length of the fiber between the fixation points. Table 3.1 compares the results of the manual approach with the microrobotic approach and presents the aforementioned parameters quantitatively. Preparing the paper fiber specimens using the microrobotic platform consumes 30% less time than the manual approach, improves the mounting precision and reduces the fiber curliness. The average gap of $670.0 \pm 10.9\ \mu m$ between the fibers indicates that the microrobotic platform provides better mounting precision compared to the manual approach ($824.3 \pm 150.3\ \mu m$), but it also indicates that there is $330\ \mu m$ offset from the target gap of $1\ mm$. This offset can be compensated by calibrating the platform in the future.

Besides the aforementioned achievements, another major achievement in this specimen preparation process is minimizing the introduction of artifacts to the paper fiber samples. Only the end points of the fiber were affected by the microgrippers and the central parts were totally untouched. The possible applied tension on the fiber during the manipulation process might be the only source of artifact with the described method. This problem can be tackled by integrating the force sensing microgrippers developed in Chapter 4 into the 3D-micromanipulators, and consequently monitoring the force applied on the fibers during manipulation and mounting. This modification is assigned as one of the future tasks to improve the platform presented in this thesis.

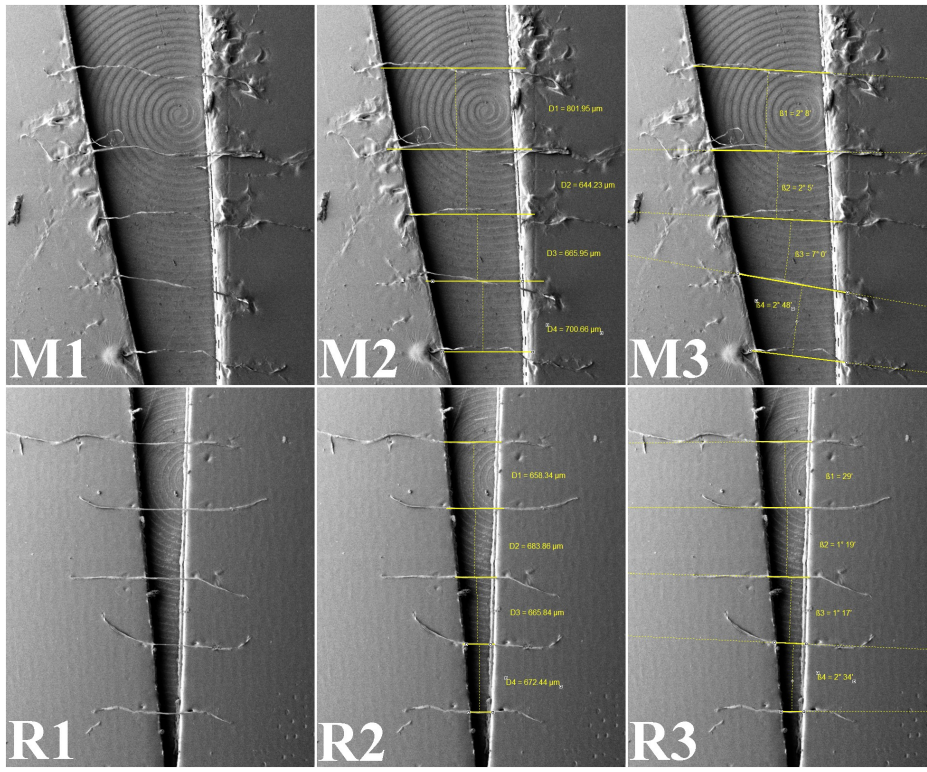

Figure 3.10: Representative images comparing the results of mounting of paper fibers manually with the results of mounting of paper fibers using microrobotic platform [4]. © *John Wiley and Sons* Reprinted, with permission, from [P. Saketi, et al., A flexible microrobotic platform for handling micro-scale specimens of fibrous materials for microscopic studies, 10/2012] - Courtesy of Manuel Mikczinski, AMiR, University of Oldenburg.

Table 3.1: Comparing the results of manual approach with the microrobotic approach.

Approaches	Manual	Microrobotic
Average Time per Stub ($minutes$)	20	14
Average Gap Between the fibers (μm)	824.3 ± 150.3	670.0 ± 10.9
Average Angle between the fibers (°)	5.1 ± 3.1	1.4 ± 0.8
Average Curliness of the fibers (μm)	90.7 ± 28.1	30.1 ± 3.1

3.3 Making Bonds using Microrobotic Platform

By reconfiguring the microrobotic platform and changing the probe connected to the manipulator C.3-F.3.2 of Figure 3.2 and Figure 3.4A with a microgripper, the microrobotic platform presented in Figure 3.4A is able to make artifact-free bonds by following the sequential chart presented in Figure 3.11 [2].

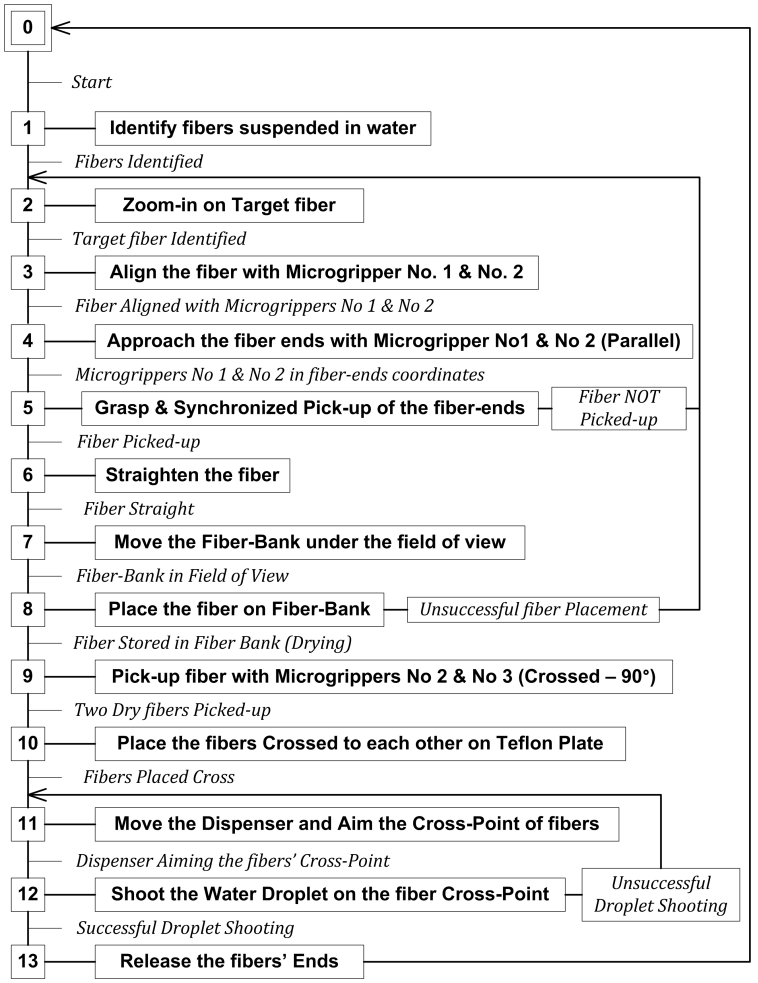

Figure 3.11: Sequential function chart of making bonds. [2]

The disintegrated pulp fibers are placed on the rotary-table using a pipette. The operator identifies the fibers in the suspension using the vision system, and selects one of them as a target, as illustrated in Figure 3.12A. Then he aligns the target fiber with microgripper C.1- F.3.4 and microgripper C.2- F.3.4. The microgrippers grasp the target fiber in the suspension Figure 3.12B. The dark shadows around the microgrippers in Figure 3.12B are caused by the water meniscus due to capillary effects. The platform picks disintegrated pulp fibers from the rotary-table by synchronizing the microgripper C.1- F.3.4 and microgripper C.2- F.3.4 [see Figure 3.12C]; straightens a fiber [see Figure 3.12D] and keeps it for a minute in order to lose enough humidity to keep its shape. Then it places it on the fiber-bank for drying in room temperature. The fiber-bank is made of SU-8, a common epoxy-based negative photoresist polymer used in lithography, with the height of 200 μm. The fiber-bank is a place to store and sort the fibers based on their dimensions. The sequential chart presented in Figure 3.11 is only a case study and it can be modified to address the needs of specific tests. For example, in order to compare the bonding properties of never-dried and dried pulp fibers it is possible to form the bonds directly from the wet state.

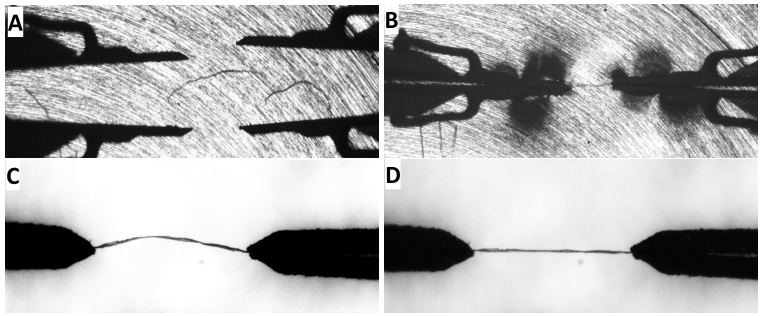

Figure 3.12: Picking-up disintegrated pulp fibers from the suspension using microgrippers. (A) Identifying the target fiber; (B) Grasping the target fiber; (C) Picking-up the fiber from rotary-table; (D) Straightening the fiber.

Next, the platform picks the fibers one by one [see Figure 3.13A], and places them crossed to each other on a Teflon-plate [see Figure 3.13B]. Water, heat and pressure are necessary factors to make a bond between

two paper fibers. The dispenser shoots a droplet of water on the cross-point of two fibers [see Figure 3.13 B & C]. Another Teflon-plate is used to cover the fibers, and the plates are placed in an oven for 45 minutes at 70 $^{\circ}C$ under 140 kN/m^2 pressure to bond the crossing fibers together [see Figure 3.13D]. The reason to choose 140 kN/m^2 pressure to form the bonds originates from the applied pressure on the last nip of a typical paper machine which is about 140 kN/m. After shooting the droplet on the crossing point of fibers, the fibers twist which leads to deviation from perfect perpendicular α-angle, this issue is addressed in Section: 3.4.

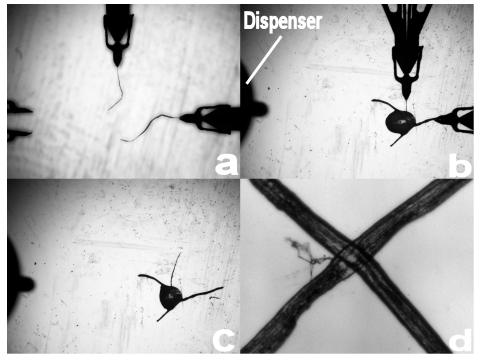

Figure 3.13: Process of making bonds. (a) Picking-up a fiber, (b) Placing the fibers perpendicular to each other on a Teflon-plate and shoot a droplet of water on the crossing point by using the dispenser, (c) Moving-out the microgrippers, and then cover the bottom the Teflon-plate with another Teflon-plate, and baking in an oven for 45 minutes at 70 $^{\circ}C$ under 140 kN/m^2 pressure (d) The produced bond [2].

3.4 Making Perpendicular Bonds using Microrobotic Platform

Even though the individual bonds made with the approach presented in Section 3.3 have a controlled crossing angle of about 90 °, it is challenging to reproduce exactly the orthogonal crossing angles because of the curliness in the fibers [5]. To address this challenge, an SU-8 structure

to hold the fibers orthogonally while pressing them is introduced in this thesis. The SU-8 structure, which is developed on a silicon wafer and used for holding the fibers orthogonally, is here called a holding-plate. The holding-plate includes a 5 × 5 matrix of star-shape fiber holders with a gap of 100 μm to hold the fibers in place (see Figure 3.14). The microrobotic platform with the configuration presented in Figure 3.2 is used for this application.

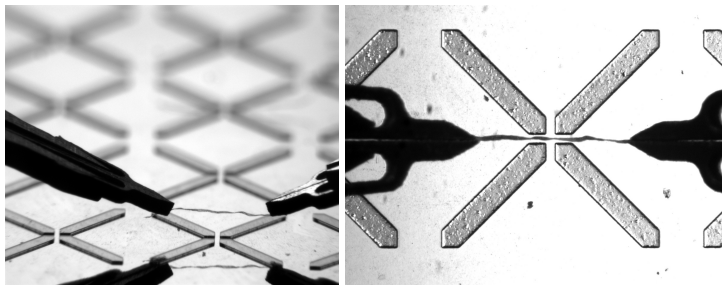

Figure 3.14: Left: Side-View; Right: Top-View. The holding-plate SU-8 structure includes a 5 × 5 matrix of star-shape fiber holders with a gap of 100 μm to hold the fibers in place [5].

In order to have a tool to press the orthogonally placed fibers, a micro-cross is fabricated on a glass substrate using SU-8 polymer. Later, the cross is detached from the substrate using tweezers. The micro-cross is formed by two orthogonal square bars with the dimensions of 480 μm × 80 μm. The 80 μm width of the micro-cross allows 20 μm tolerance for fitting the micro-cross into the 100 μm star shape holding-plate. The height of the star shape structures on the holding-plate is 45 μm, while the height of the micro-cross is 85 μm. This 40 μm height difference between the star shape holding-plate and the micro-cross ensures a proper pressing of the fibers against each other.

Figure 3.15 shows the process of making individual bonds with the orthogonal crossing angle. The microgrippers pick up an individual fiber from the water suspension and pull it to make it straight. Then the microgrippers place the fiber in the 100 μm gap of the star shape fiber holder (Figure 3.15A). While the probe keeps the fiber inside the gap, the

microgrippers release the fiber ends (Figure 3.15B).

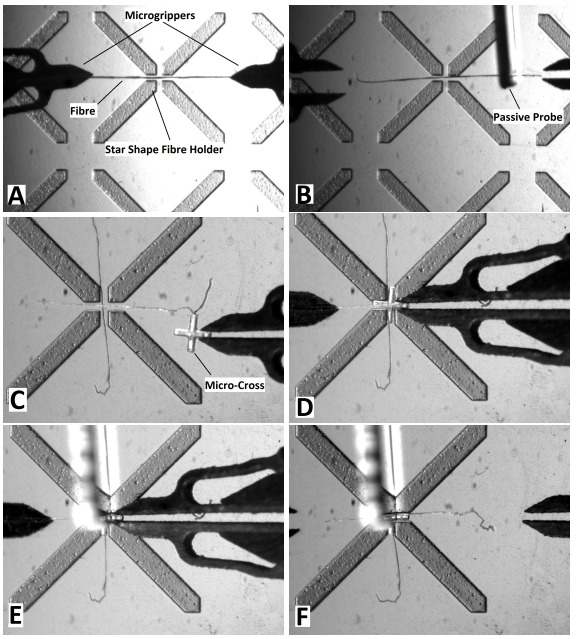

Figure 3.15: The process of making individual bonds with orthogonal crossing angle [5]. © *FRC 2013* Reprinted, with permission, from [P. Saketi, et al., Method for investigation of aged fibre-fibre bonds with micro and nanorobotic tools, 9/2013].

After placing a horizontal fiber in all the gaps over the entire matrix, the holding plate is rotated 90 ° and the aforementioned fiber placing process is repeated in order to place the second fiber perpendicular to the first one (Figure 3.15C). In order to press the fibers a microgripper grasps the micro-cross and aligns it with the trenches on the star shape substrate (Figure 3.15C & D). Since the pre-pressed fibers act like a spring, the probe is used to secure the micro-cross in its place (Figure 3.15E). The microgripper releases the micro-cross while the probe keeps it in place (Figure 3.15F). In order to create the hydrogen bonds between the fibers, a small droplet of water is placed next to the micro-cross manually using a syringe. The water flows into the cross section area of the fibers due to capillary forces. Then the probe pushes the micro-cross against the substrate and presses the fibers together with 3 N force for 15 minutes. The same process is repeated to create the rest of the bonds. Finally, the individual bonds are picked and placed on glass slides, and

the glass slides are stored inside Petri dishes.

3.5 Discussions

A modular microrobotic platform for manipulation and specimen preparation of micro-scale fibrous materials is designed and developed. Its features and performance were demonstrated by preparing specimens for SEM and NT, and also making individual fiber bonds. The presented bond making methods in this chapter were aimed to demonstrate the feasibility of the developed methods. Therefore, parameters such as the dry content, swelling degree of the fibers and drying times were not analyzed in the procedures. In order to perform these methods as routine sample preparation procedures, strict protocols should be defined and followed during the experiments. These protocols can now be created as a result of this work. In addition, the sequential charts of the processes should be modified according to the requirements of the tests.

Comparison of the manual approach and the microrobotic approach indicates that the specimen preparation time for SEM was reduced by 30%.The coefficient of variance for the gaps between the fibers with the manual approach was 18.2% and with the microrobotic approach was 1.6% which indicates that the microrobotic approach is much more precise than the manual approach.

In handling specimens for nanotomography, the mounting of a strand of human hair and an individual paper fiber bond on a specimen holder (an STM probe) was successfully demonstrated using the microrobotic platform. The inspection of paper fiber bonds using NT provides important information regarding their bonding mechanism, illustrates the interaction between the two fibers in the bonded area, and measures the real bonded area. Taking into account the small force which bonds two individual paper fibers together, mounting an individual paper fiber bond on the sample holder without damaging it was a distinctive achievement.

Making of individual fiber bonds was demonstrated successfully [2, 5]

and the use of the platform can minimize the artifacts of the conventional bond making process. Since the individual paper fiber bonds are made using the microrobotic platform, the bonds have the desirable crossing angle (α) of 90 °, and also the desirable vertical angle (β) of zero. The demonstrated bond making methods lack the force control feature during the pressing step. This shortcoming can be solved by integrating the available tools such as the force controlled piezoelectric fiber press [122] into the microrobotic platform in the future.

4 Force Sensing Microgrippers

The aim of this section is introducing novel force sensing microgrippers for mechanical characterization of micro-scale fibers. Since the case study in this thesis focuses on paper fiber bonds, and because of lack of conclusive information on bond strength of paper fibers in the literature, especially before 2011, the required force range for the force sensor is estimated and reported in Section 4.1. Then three force sensing microgrippers are developed for different force ranges. Two of the force sensing microgrippers are based on PVDF, and they are developed for the force ranges of 1 $mN - 10$ mN. Another force sensing microgripper, based on microsprings, is developed for the force ranges of 4.5 $mN - 20$ mN.

A PVDF force sensor with passive specimen holder is developed for Z-directional bonding force measurement. Low Z-directional bonding strength results in delamination and splitting of paper during printing and coating operations [30]. Therefore, paper and board industry is interested in measuring Z-directional bonding forces between pulp fibers. Design and development of the PVDF force sensor with passive specimen holder is described in Section 4.2.2.

Another PVDF force sensor is integrated into a microgripper for shear-mode bonding force measurement. The shear-mode bonding forces

affect the tensile and tear strength of paper hand-sheets which makes it an important parameter for the paper industry. Design and development of the PVDF based force sensing microgripper is presented in Section 4.2.3.

The mentioned PVDF force sensing microgrippers can measure the force but they can not measure the strain. The microspring based force sensing microgripper is capable of measuring both the force and the strain, which makes it suitable for micro-tensile testing applications.

4.1 Force Range Estimation

The microrobotic platform presented in Chapter 3 is reconfigured to estimate the required forces to break the bonds of various pulp fiber samples. Figure 4.1 illustrates the reconfiguration and implementation of the platform. In order to grasp and manipulate the fibers in the XYZ directions, microgrippers C.1-F.4.1 and C.2-F.4.1 are used. In this configuration, the probe attached to microgrippers C.3-F.3.4 in Figure 3.4 is replaced with a glass-slide C.4-F.4.1 in Figure 4.1. The glass-slide is used both for gluing and glue removal purposes. The rotary-table C.5-F.4.1 and a 10 mN force sensor C.7-F.4.1 (FemtoTools AG, Switzerland) are mounted on the top of the XY-table C.6-F.4.1. The sensitivity and resolution of the force sensor are 5000 $\mu N/V$ and 2 μN, respectively. A syringe pump (New Era Pump Systems Inc., USA) with a silicon tube C.8-F.4.1 is used for supplying glue-removing Acetone onto the glass-slide C.4-F.4.1. A PCI-6259 (National Instruments, USA) measurement board is used for acquiring data from the force sensor. An Acetone-soluble glue is used to attach the free end of fibers to the force sensor probe. From this point, the rest of the experiment is performed in a tele-operated process using the microrobotic platform. The XY-table moves the rotary-table under the field-of-view (FOV). The rotary-table orients the fibers. After imaging the bonding area, one of the bonds is grasped and picked-up with two microgrippers in synchronized mode. Most of the bonds flip during the grasping and form a vertical cross between the microgrippers.

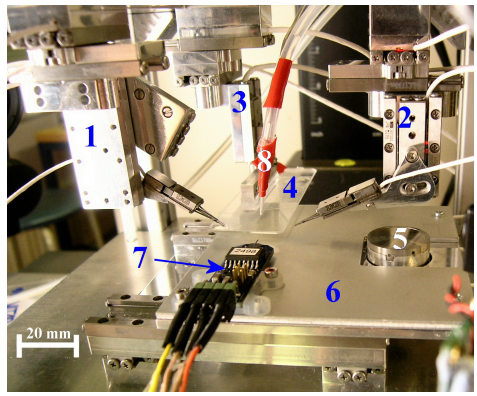

Figure 4.1: Implementation of the microrobotic platform for estimation of bond breaking forces. (1) and (2) XYZ-microgrippers, (3) Glass-slide-micromanipulator, (4) Glass-slide, (5) Rotary-table, (6) XY-table, (7) Force sensor, (8) Tube of the syringe pump [6].

Figure 4.2 illustrates the tele-operated process of bond strength measurement using the microrobotic platform. A droplet of glue is placed on the edge of the glass-slide. The glass-slide is moved to the FOV and aligned with the force sensor probe using the visual feedback [see Figure 4.2A]. The force sensor probe is dipped into the glue [see Figure 4.2B] and is then aligned with the free end of the bond both horizontally and vertically [Figure 4.2C]. After waiting three minutes the glue is cured. The distance between the bonded area and the end of the crossing fiber is far enough in order to secure the bonded area from getting contaminated with the glue.

To measure the bond strength, the XY-table moves the force sensor and thus the crossing fiber in continuous 5 μm steps backwards until the bond breaks [see Figure 4.2D]. To use the force sensor in the next measurement, the glue contamination on the probe should be removed. The syringe pump infuses droplets of Acetone onto the edge of the glass-slide and then the force sensor probe is dipped into Acetone to remove the remaining glue. It is necessary to calibrate the force sensor after glue removals to verify that the performance parameters of the force sensor have not changed. The first set of bonds was made from untreated refined bleached Kraft softwood pulp sample using the traditional bond

making approach explained in Section 2.1.2. Therefore, the fibers in the bonds were not perpendicular and they had randomly formed α angles.

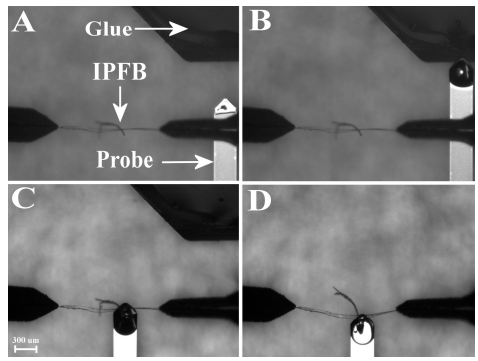

Figure 4.2: Top-View: Process of bond strength measurement to estimation the bond breaking forces. (A) Placing the glue onto the glass-slide and moving the glass-slide under the FOV. IPFB: Individual Paper Fiber Bond. (B) Dipping the force sensor probe into the glue. (C) Aligning the free end of the bond with the force sensor probe and curing the glue. (D) Moving the force sensor backwards and breaking the bond while measuring the force [6].

Table 4.1 shows the results of bond strength measurements to estimate the breaking force range for the bonds made with the traditional approach. In order to estimate the bonded area, the number of pixels on the cross point of the fibers which form the visible bonded area are counted, and the bonded area is calculated using the zoom information from top-view.

Table 4.1: Bond strength measurement results to estimate the breaking force range for the bonds made with traditional approach [6].

Test No.	Force (μN)	Area (μm^2)	Strength (N/mm^2)
1	2349.1	929.4	2.5
2	943.3	685.3	1.4
3	9877.0	523.4	18.9
4	9989.5	626.2	16.0
5	1726.8	1076.8	1.6

The known reasons for the high variation in the results are as follows: random crossing angle; uncertainty in the estimation of real bonded area; the softwood pulp sample contains multiple species; the fibers were a mixture of late-wood and early-wood.

4.1.1 Effect of aging on bond strength

The second set of bonds were made perpendicularly from unrefined bleached Pine Kraft pulp sample using the novel approach presented in Section 3.4. In order to get more information on bonding forces and the parameters affecting them, after forming the bonds, some of the bonds are artificially aged using an accelerated thermal aging process at 100 $^{\circ}C$ under dry conditions for 72 $hours$. While it is generally believed that aging the paper fibers for three days at 100$^{\circ}C$ is equivalent to 25 years natural aging [123], a standard condition for aging paper fibers does not exist in the literature [124]. It is reported that the thermal aging of paper fibers in dry conditions leads to more reproducible results compared to aging under humid conditions [125]; thus in this study the thermal aging is performed under dry conditions [5].

The process of bond strength measurement is almost the same as the one explained in the beginning of this section with the following changes. In the previous study, prior to the bond strength measurement the fiber was stretched by using the microgrippers. Therefore, the fiber was under axial tension, which led to uncertainties in the bond strength measurements. In this study, after grasping the fiber bond from one end, the other end of the fiber was grasped without relocation. If the fiber-end grasping has led to relocation of the fiber-end, this relocation is detected by matching the current location with the prior images, and it is compensated by moving the fiber-end to the original location using the microgripper. Therefore, the influence of axial tension on the bond strength measurement was reduced. Figure 4.3 illustrates the process of bond strength measurement to estimate the breaking force range of perpendicularly formed bonds. In order to study the de-bonded areas, the fiber which is left between the microgrippers is mounted on an SEM

stub and the area is marked to be retrieved in the SEM. The detailed process of using the microrobotic platform for SEM specimen preparation was reported in Section 3.2. Since the other fiber which was glued to the force sensor probe is washed away by Acetone during the cleaning process of the force sensor, it is therefore not recoverable for further studies.

Figure 4.4 shows a representative graph of the bond strength measurements of a reference sample (Test No. 3 - in Table 4.2). The force-displacement curve in Figure 4.4 shows the superposition of three forces: the force required to bend the grasped fiber and the force required to rotate the bond plane and consequently the grasped fiber, as well as the force required to break the bond. Therefore, the initial part of the graph is not linear, but the last part of the curve before the bond rupture shows a linear behavior. The peak point represents the maximum force required to break the bond. Besides force-displacement, Figure 4.4 indicates that after the bond breaks there is a friction force between the two fibers, which is the reason that the force does not drop to zero [5].

An important finding during these measurements is the non-linear behavior of the entire bond structure prior to the breaking point. It was shown in Figure 4.4 that the force measured during the bond breaking process is the superposition of three forces: (1) the force required to bend the grasped fiber; (2) the force required to rotate the bond plane and consequently the grasped fiber; (3) the force required to break the bond. It was shown that only the last part of the force-displacement curve, before the bond rupture, behaves linearly which represents the stiffness of the bond.

In the mentioned experiments three types of bonds were measured: (i) bonds that were made using the traditional approach; (ii) perpendicular bonds that were made using the microrobotic platform; (iii) artificially aged perpendicular bonds that were made using the microrobotic platform. The results of bond breaking force range estimation experiments indicates that the forces are in the range of $0.1\ mN - 13\ mN$.

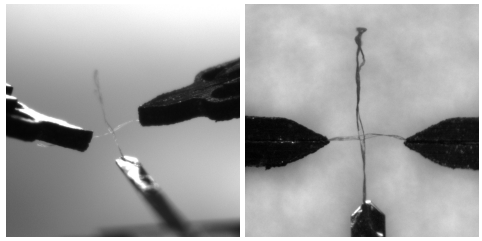

Figure 4.3: Left: Side-View; Right: Top-View. Process of bond strength measurement to estimate the breaking force range of perpendicularly formed bonds. [5].

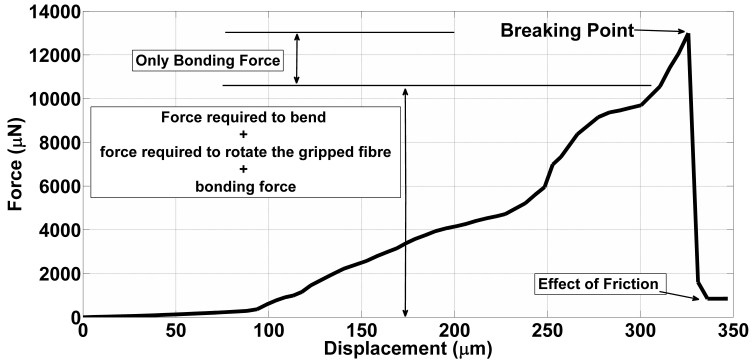

Figure 4.4: Representative graph of a bond strength measurement [5].

Table 4.2: Individual Bond Strength Measurement Results (Not-Aged vs. Aged) [5].

Test No.	Force (μN)	Area (μm^2)	Strength (N/mm^2)	Force (μN)	Area (μm^2)	Strength (N/mm^2)
1	3181	2040	1.56	179	1318	0.14
2	2832	1444	1.96	478	1596	0.30
3	12995	2862	4.54	< 100	1824	0.05
4	12683	1642	7.72	< 100	924	0.11

4.2 Development of PVDF based Force Sensing Microgripper

This section presents two force sensors based on PVDF for the force ranges of 1 $mN - 10\ mN$. The first one is a PVDF sensor with a passive specimen holder for Z-directional bonding force measurement. The second one is a PVDF based force sensing microgripper for bonding force measurement in shear and peeling modes.

4.2.1 Proof of Concept

The main component of the proposed force sensor is a PVDF element, in this case the LDT0-028K model (Measurement Specialties Inc., USA). The PVDF element is made of a 28 μm thick piezoelectric PVDF polymer film with screen-printed Ag-ink electrodes laminated between two 0.125 mm polyester substrate films. The film element produces more than 10 $mV/\mu Strain$, about 60 dB higher than the voltage output of a foil strain gauge [96]. The piezoelectric coefficients provided by the manufacturer are $d_{33} = -33\ pC/N$ (compression) and $d_{31} = 23\ pC/N$ (stretching) [96]. The reason for selecting this particular PVDF element is that in its simplest mode the film behaves like a dynamic strain gauge except that it requires no external power source and generates signals greater than those from conventional foil strain gauges after amplification [3].

In order to check if the sensitivity, linearity and repeatability of the PVDF film is sufficient for bonding force measurement applications, an FT-S10000 force sensor (FemtoTools AG, Switzerland) is used as a reference force sensor to calibrate the PVDF film sensor in a bending mode. Figure 4.5 illustrates the schematic setup for calibrating the PVDF film in the bending mode. Figure 4.6 is a schematic of the measurement electronics and the measurement set-up. Figure 4.6 also shows that the reference sensor, the linear actuator and its controller are a separate system from the PVDF sensor and its measurement electronics which also form a separate system. They are, however, in a mechanical contact

to each other [3].

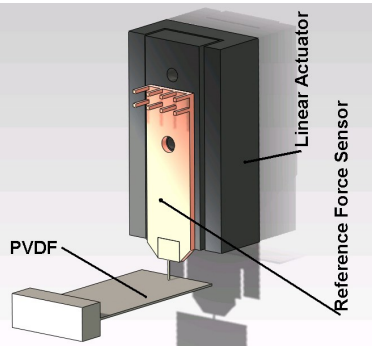

Figure 4.5: The schematic setup for calibrating the PVDF film in bending mode.

A 9 V battery, regulated to 5 V, is used as a power supply in order to minimize the noise in the measured output voltage. The signal produced by the PVDF sensor is conditioned using a charge amplifier. The feedback of charge amplifier includes a 5.6 nF capacitor and a 500 $M\Omega$ resistor, which leads to a high-pass cut-off frequency of 0.06 Hz, and corresponding to a time constant of 2.8 s. The feedback capacitor sets the gain of the charge amplifier at 0.18 V/nC. In order to avoid aliasing, the signal is low-pass filtered with a 1^{st} order filter having a 40 Hz cut-off frequency, which is sufficient for the applied velocity of the displacement. The charge amplifier is integrated into a data acquisition device with a 16 bit A/D-converter. The data acquisition device is controlled and powered through a USB connection. A 1 kHz sampling frequency is used to acquire the measurement data. An NI PCI-6259 measurement board (National Instruments, USA) is used to measure the output voltage of the FemtoTools reference force sensor.

In order to apply repeatable loading and unloading cycles to the PVDF film during the calibration process, the linear actuator is controlled using a closed-loop position controller which provides 100 nm resolution and ± 1 μm repeatability. Due to the mechanical contact, it is possible to track their common displacement using the displacement sensor of the actuator. Therefore, the sensor readings can be synchronized using the

displacement measurement and the Force –Voltage calibration curve can be derived [3].

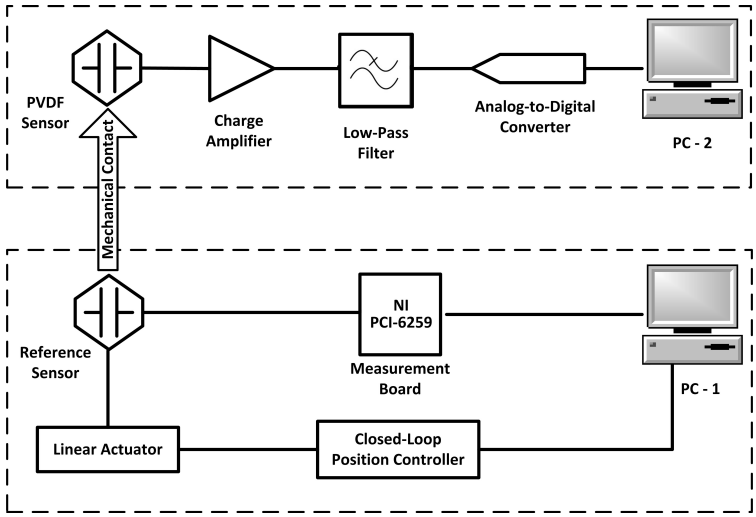

Figure 4.6: Schematics of the measurement electronics and the calibration set-up [3]. © *ELSEVIER 2015* Reprinted, with permission, from [P. Saketi, et al., PVDF microforce sensor for the measurement of Z-directional strength in paper fiber bonds, 2/2015].

The linear actuator is controlled by an SCU controller (Smaract GmbH, Germany) which is connected to a computer user interface. A series of nine square pulses with increasing amplitude are used to calibrate the PVDF sensor. The pulse amplitude is increased by 50 μm each time, with the actuator being returned to its initial position between the pulses. The pulse width and period are 3 s and 6 s, respectively [see Figure 4.8], and the actuator velocity is 4 mm/s. This input signal is selected because of the properties of the PVDF sensor. The PVDF sensor is a dynamic sensor and its previous state does not affect the signal. Therefore, in order to improve the accuracy of the calibration, the zero-load had to be secured. Thus, the actuator must return to its initial position after each pulse. Although the bonding force measurements are performed at a specific rate, because the PVDF is a dynamic sensor, it is possible to calibrate it for that specific rate and thus adapt it to this specific application. The selected FemtoTools force sensor, with a resonance frequency of 12 kHz and maximum capacitance-to-voltage conversion sampling rate

of 8 kHz, provides sufficient frequency range for calibration of the PVDF film [3].

Figure 4.7 illustrates the raw data and the filtered data of the reference sensor and PVDF sensor for one of the applied pulses of the input signal in Figure 4.8 [3]. In order to perform the calibration experiment, the input signal in Figure 4.8 is repeated ten times. Figure 4.7 indicates that, after peaking, the PVDF sensor signal attenuates much faster than the reference sensor signal. This is because the PVDF sensor measures dynamic force, so when there is no change in the force, the signal attenuates much faster and it will not show the existence of a constant force. Therefore, with the PVDF sensor, it was the first value around the peak that was used for calibration. Because the reference sensor measures static force, the slight attenuation in its signal was caused by stress relaxation, which will remain constant after the stress relaxation phase. However, because the reference sensor was a capacitive sensor, not only were the first values around the peak exaggerated due to the heavy load, but there was also a significant oscillation in the signal around the peak point. In order to eliminate these issues, a 2nd order Butterworth filter is applied to the reference sensor data. Even though the PVDF sensor signal behaves differently than the reference force signal, this does not hinder the application proposed here because the amount of force during loading can be gauged by observing only the sharp edges of the recorded waveform, as is explained below [3].

Figure 4.9 illustrates the filtered output of the reference force sensor for the first cycle of the input signal, and Figure 4.10 shows the corresponding filtered output of the PVDF film sensor. The loading and unloading directions in Figure 4.9 and Figure 4.10 are indicated with the letters “L” and “U”, respectively. During the loading of the PVDF film, the linear actuator is moved forward and the force in the reference sensor increases. This causes the PVDF film to bend downwards. The deformation in the PVDF film results in a voltage reduction in its output. During unloading, the linear actuator is moved backward and the force is reduced; the PVDF film moves back to its initial position resulting in a voltage increase in its output [3].

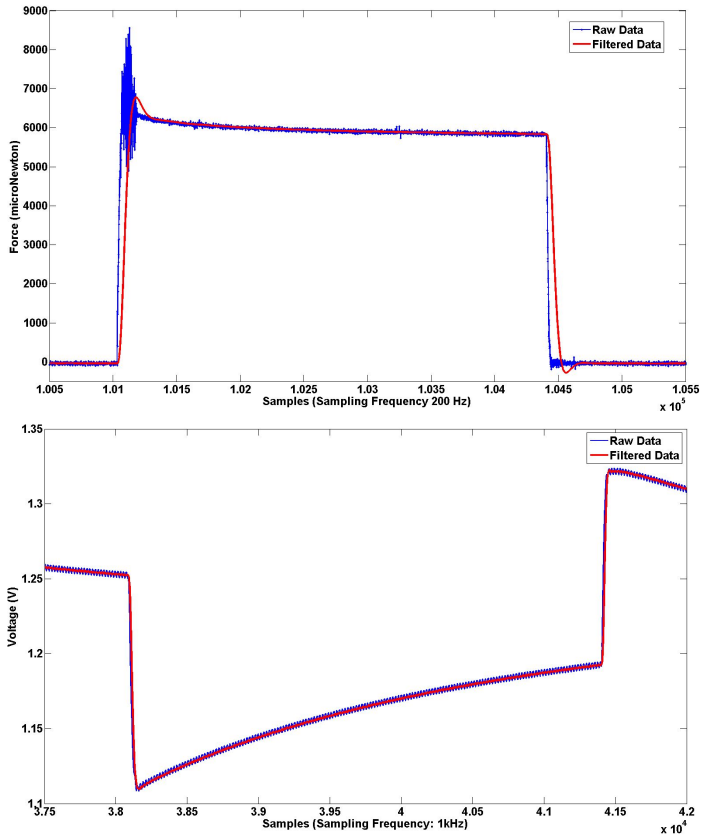

Figure 4.7: The raw data and the filtered data of the reference sensor (Top) and PVDF sensor (Bottom) for one of the applied pulses [3]

.

Figure 4.11 shows the mean and the standard deviation of the measured force values for the reference sensor when nine input pulses are repeated 10 times. The output of the reference sensor increases linearly in every cycle, and there is a small deviation between each cycle. The mean value and the standard deviation (STD) of the reference force sensor output are shown in Figure 4.11 and Table 4.3. The highest Relative Standard Deviation (RSD) is 8.16% for the first pulse with a 50 μm displacement and 972.59 μN force. Table 4.3 shows that the RSD decreases significantly when the force is increased, which corresponds to the general behavior of sensors and it means the measurements are more reliable at higher forces than at lower ones [3].

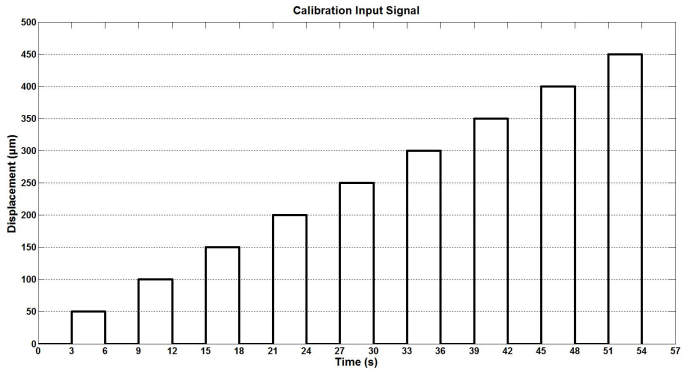

Figure 4.8: Input signal sequence for calibrating the proposed force sensor. A series of nine square pulses of increasing 50μm amplitude, with the displacement returning to the initial value after each pulse [3].

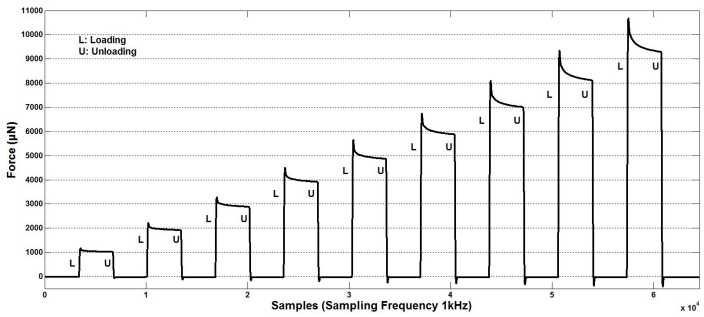

Figure 4.9: Filtered output of the reference sensor for an input of nine rectangular pulses of increasing 50 μm amplitude [3].

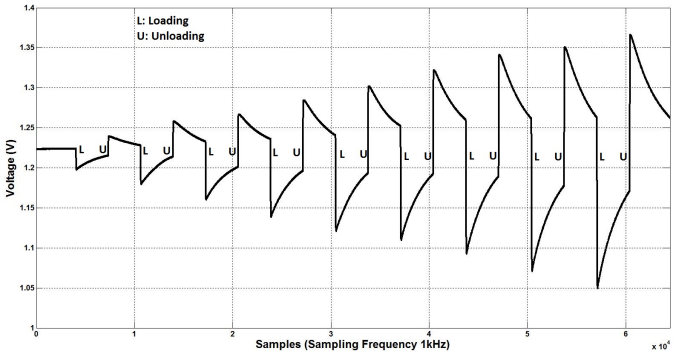

Figure 4.10: Filtered output of the proposed PVDF film sensor for an input of nine rectangular pulses of increasing 50 μm amplitude [3].

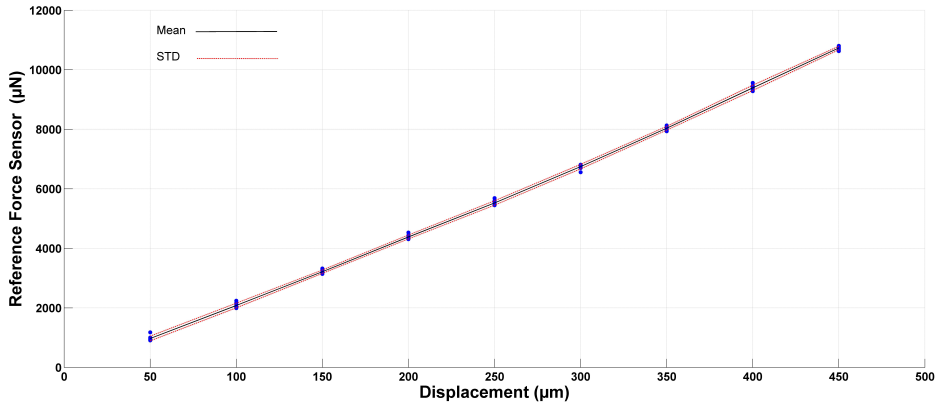

Figure 4.11: Mean and standard deviation of the reference sensor output for ten repetitions of the input signal sequence [3].

Table 4.3: Relative standard deviation for the output of the reference force sensor. The input signal sequence is repeated ten times [3].

Pulse No.	1	2	3	4	5	6	7	8	9
Mean (μN)	972.6	2081.7	3216.6	4384.6	5526.9	6747.6	8036.6	9394.8	10734.9
STD (μN)	79.38	78.53	56.90	65.67	74.16	75.53	63.60	87.27	59.62
RSD (%)	8.16	3.77	1.77	1.50	1.34	1.12	0.79	0.93	0.56

Figure 4.12 shows the voltage differences in the output of PVDF film sensor when nine input pulses are repeated 10 times. It illustrates that the voltage difference in the output of the PVDF film increases linearly in every cycle, and that there is a small deviation between each cycle. The mean value and the STD of the PVDF film output are presented in Figure 4.12 and Table 4.4. The highest RSD is 8.96% which corresponds to a 50 μm displacement and a 22.08 mV voltage difference. Table 4.4 indicates a significant decrease in RSD when the output voltage difference increases which also corresponds to the general behavior of sensors as it was mentioned before [3].

Figure 4.12 and Table 4.4 indicate sufficient linearity and repeatability for the PVDF film. The sensitivity of PVDF film is 0.47 $mV/\mu m$ which is equivalent of 23.9 $\mu N/\mu m$. Consequently, a similar PVDF film sensor

is combined with a passive specimen holder for Z-directional bonding force measurement which is explained in detail in Section 4.2.2. In Section 4.2.3 a PVDF film sensor is integrated into the microgripper for measuring the bonds in shear and peeling modes [see Figure 2.3].

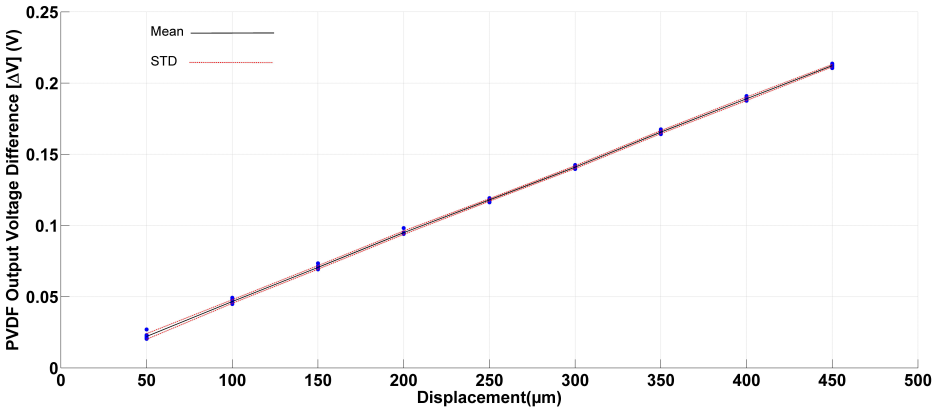

Figure 4.12: Mean and standard deviation of voltage difference of PVDF film sensor for ten repetitions of the input signal sequence [3]. © *ELSEVIER 2015* Reprinted, with permission, from [P. Saketi, et al., PVDF microforce sensor for the measurement of Z-directional strength in paper fiber bonds, 2/2015].

Table 4.4: Relative standard deviation for the output of the PVDF film sensor. The input signal sequence is repeated ten times [3].

Pulse No.	1	2	3	4	5	6	7	8	9
Mean (mV)	22.1	46.6	70.6	95.0	118.0	141.0	166.0	189.0	212.2
STD (mV)	1.98	1.27	1.23	1.20	0.89	1.00	1.08	1.22	0.89
RSD (%)	8.96	2.73	1.75	1.26	0.76	0.71	0.65	0.64	0.42

4.2.2 PVDF Sensor with Passive Specimen Holder for Z-directional Bonding Force Measurement

Figure 4.13 shows a schematic design of the sensor. The sensor includes the following components: C.1-F.4.13 is the PVDF element; C.2-F.4.13 is a bond-holder with the bond samples mounted on its tip; C.3-F.4.13 is a connecting-element which fixes the bond-holder in place on top of the PVDF sensor; C.4-F.4.13 is a mounting-stage which is used for integrating the PVDF sensor into the microrobotic platform and C.5-F.4.13 represents a bond [3].

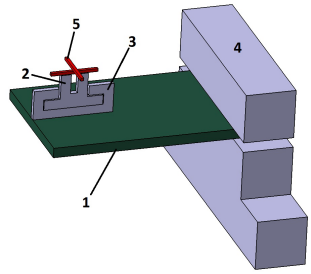

Figure 4.13: Schematic Design of the Sensor: (1) PVDF element; (2) Bond-Holder; (3) Connecting-Element; (4) Mounting-Stage, and (5) Individual Paper Fiber Bond [3].

Figure 4.14A shows the implementation of the sensor; the component numbers are the same as in Figure 4.13. The connecting-element and the bond-holder are shown in Figure 4.14B and Figure 4.14C, respectively. Since the bond-holders should be disposable, they were 3D-printed using white Polylactide. With regard to the Stacked Gantry Crane configuration of the microrobotic platform [5, 2, 6] and the integration of the PVDF sensor in it, instead of gluing the connecting-element, C.3-F.4.13, perpendicular to the length axis of the PVDF film which provides better sensitivity, it is glued along the length axis of the PVDF film at its free end. This design is enforced by the orientation of the microgrippers with regards to the final integration of the sensor which enables the Z-directional bond strength to be measured which will be described in Section 5.1. Basically, the procedure is that the bond-holders are remov-

able parts used for mounting the fiber bonds. A number of bond-holders are produced and placed in a stack [see Figure 4.14D]. The fiber bonds are mounted on the bond-holders with the same processes as reported in Chapter 3. Then, the bond-holders are placed on the connecting-element, one at a time, in order to measure the bond strength [3].

Figure 4.15 is a schematic of the calibration setup. It includes the following components: C.1-F.4.15, which is the proposed force sensor unit; C.2-F.4.15, the reference force sensor; C.3-F.4.15, which is an actuator connector that attaches the reference sensor to the linear actuator, C.4-F.4.15 [3]. Figure 4.16A shows the implementation of the calibration setup. The PVDF film sensor, C.1-F.4.16, is placed on the top of an XY-table. The XY-table, C.5-F.4.16 enables the PVDF film sensor to be aligned with the reference sensor. The reference sensor, C.2-F.4.16, is mounted perpendicularly on the PVDF film sensor using the actuator connector. The L-shaped actuator connector, C.3-F.5, allows parallel movements of the reference sensor and the linear actuator, C.4-F.4.16 [3].

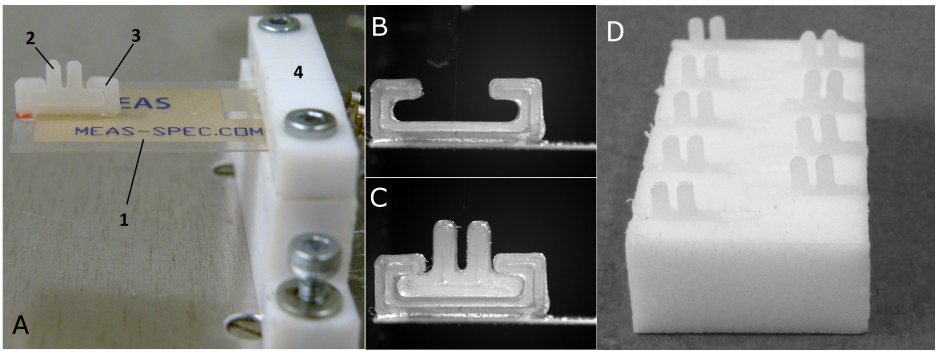

Figure 4.14: (A) Implementation of the Sensor: (1) PVDF film; (2) Bond Holder; (3) Connecting-Element and (4) Mounting-Stage. (B) Connecting-Element; (C) Bond-Holder placed inside the Connecting-Element; (D) Stack of Bond-Holders [3].

The calibration set-up was placed under a stereo computer vision system. Prior to starting the calibration, the bond-holder was placed inside the connecting-element [see Figure 4.16B]. Figure 4.16B also shows that the probe of the reference force sensor was aligned with both the

center-line of the PVDF film sensor and the center-line of the bond-holder using the XY-table. Since the length of the reference force sensor probe is 3 mm and the depth of the bond-holder gap is 2 mm, in order to keep the force sensor safe from accidental collisions, the bond-holder is removed from the connecting element, and the reference force sensor probe is then moved down till it reaches the connecting-element [see Figure 4.16C]. The perpendicularity of the reference sensor to the actuator connector is verified using the images acquired from the side-view camera. Since the loading direction in the bond strength measurement process is the same as the loading direction during the calibration process, only the data acquired during the loading of PVDF film is used for the calibration. When measuring the bond strength, the PVDF film is unloaded after the bond breaks. Consequently, the unloading data is of no further interest in this study, and has not been analyzed [3].

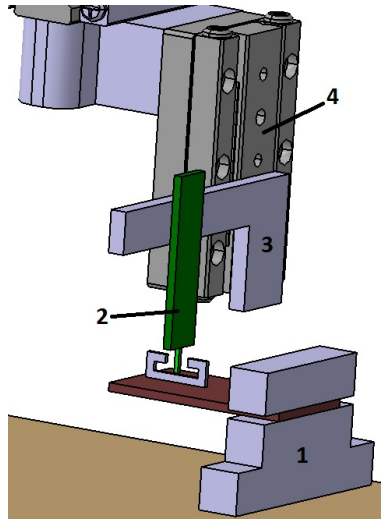

Figure 4.15: Schematic of the calibration setup: (1) Proposed PVDF force sensor; (2) Reference force sensor; (3) Actuator connector, and (4) Linear actuator [3].

The input signal presented in Figure 4.8 is used for the calibration process. Since the reference sensor probe and the PVDF film have been mechanically in contact throughout the measurements, the displacements in the sensors are identical. Thus the displacement axis in Fig-

ure 4.11 and Figure 4.12 are identical. Therefore, it is possible to plot the reference force sensor output versus the PVDF film output shown in Figure 4.17, which includes a linear calibration fit for the proposed force sensor. The slope of the linear calibration line is 51.25 $\mu N/mV$ and there is a -359.2 μN offset in the calibration curve [3]. The comparison of the RSDs between the reference sensor and PVDF sensor in Table 4.5 indicates that after the first pulse, the PVDF film sensor is even more repeatable than the reference sensor, thus it can be used reliably.

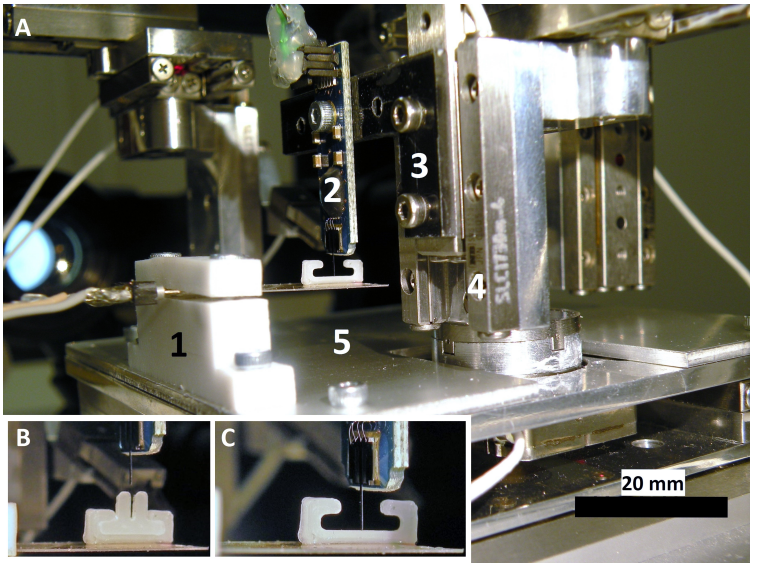

Figure 4.16: (A) Implementation of the calibration setup: (1) Proposed sensor unit; (2) FemtoTools reference sensor; (3) Actuator connector; (4) Linear actuator; (5) XY-table. (B) Alignment of reference sensor probe and the bond-holder. (C) Placement of the reference force sensor probe on the connecting element [3].

Table 4.5: Relative Standard Deviation for the output of the PVDF film sensor. The input signal sequence is repeated ten times.

Pulse No.	1	2	3	4	5	6	7	8	9
Reference Sensor	8.16	3.77	1.77	1.50	1.34	1.12	0.79	0.93	0.56
PVDF film Sensor	8.96	2.73	1.75	1.26	0.76	0.71	0.65	0.64	0.42

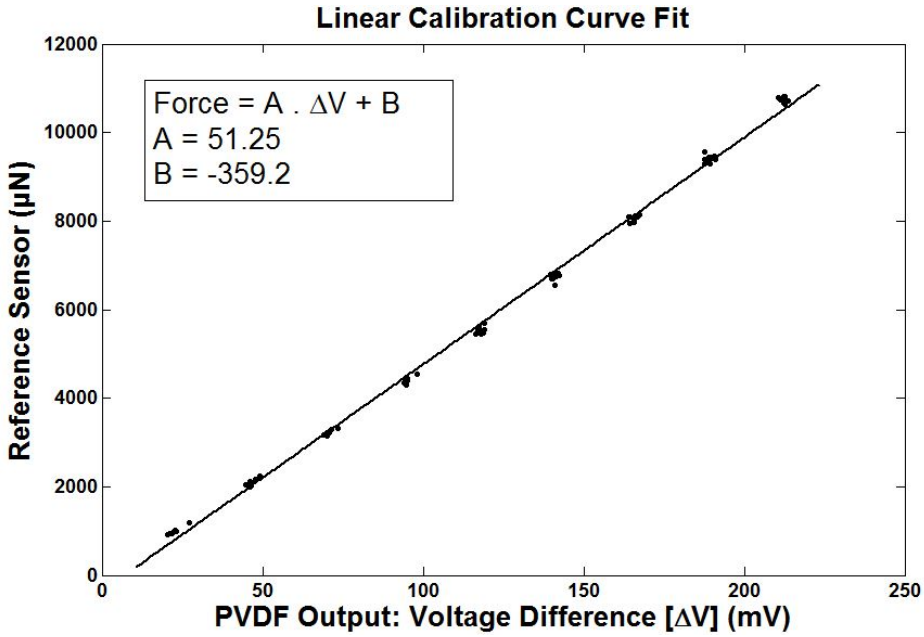

Figure 4.17: Linear calibration fit of the PVDF sensor with passive specimen holder for Z-directional bonding force measurement [3].© *ELSEVIER 2015* Reprinted, with permission, from [P. Saketi, et al., PVDF microforce sensor for the measurement of Z-directional strength in paper fiber bonds, 2/2015].

The calibration results indicate that the RSD for forces higher than 3 mN after the third input pulse is less than 2%, which is in an acceptable range. It also shows that the RSD decreases as the measured force increases. One source of error is the repeatability of the linear actuator, ± 1 μm, as this affects the repeatability of both the reference and PVDF sensors. The effect of the linear actuator repeatability on the first pulse, at 50 μm displacement, corresponds to a 2% error, while for the last pulse, at 450μm displacement, it corresponds to a 0.22% error. The higher the displacement, the lower the error in the actuator repeatability. The linear calibration fit in Figure 4.17 is used for the Z-directional bonding force measurements.

4.2.3 Integration of PVDF Force Sensor into Microgripper

For measuring the bond forces in shear and peeling modes a force sensing microgripper is required. Figure 4.18 shows the implantation of a PVDF film into a piezoelectrically actuated microgripper. The SG-06 microgripper (SmarAct GmbH, Germany) has a maximum jaw opening of 1 mm, a gripping force of 0.3 N, a resolution of few nanometers and it weighs 2 g. The microgripper C1.-F.4.18 is attached to the PVDF film C3.-F.4.18 using a gripper-connector C2.-F.4.18. The PVDF film is fixed on the mounting-stage C5.-F.4.18 using two M2 screws. The wires of microgripper are fixed to wire-stand C4.-F.4.18 using glue. The gripper-connector and the mounting-stage are fabricated using a 3D printer (miniFactory Oy, Finland).

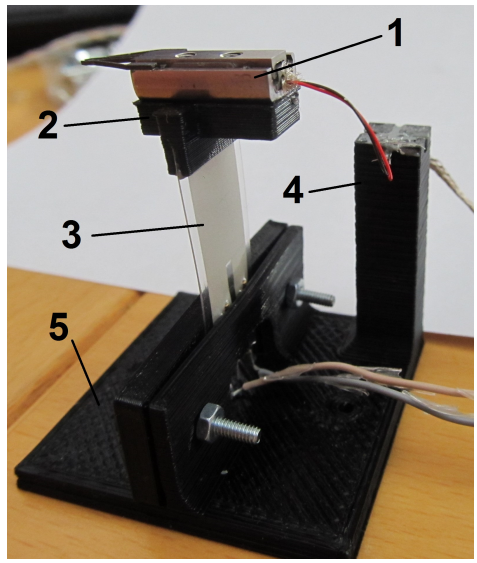

Figure 4.18: PVDF based force sensing microgripper. (1) Microgripper; (2) Gripper-connector; (3) PVDF film; (4) Wire-stand; (5) Mounting-stage.

Figure 4.19 shows the calibration set-up for the PVDF based force sensing microgripper. The PVDF based force sensing microgripper C.1-F.4.19 and the reference force sensor C.2-F.4.19 are aligned using a 3D-micromanipulator C.3-F.4.19. The 3D-micromanipulator and the refer-

ence force sensor are connected using a connecting-element C.4-F.4.19. The same measurement electronics as Figure 4.6 with a different input signal are used to calibrate the PVDF based force sensing microgripper. The new input signal is shown in Figure 4.20 which is a series of ten square pulses of increasing 100 μm amplitude, with the displacement returning to the initial value after each pulse. This new input signal with increasing 100 μm amplitude is different from the previous one used for the calibration of Z-directional sensor with increasing 50 μm amplitude. In order to calibrate the PVDF based force sensing microgripper, this input signal is repeated ten times. Figure 4.21 and Table 4.6 show the resulting calibration curve and the percentage of RSD for the output of the PVDF based force sensing microgripper, respectively.

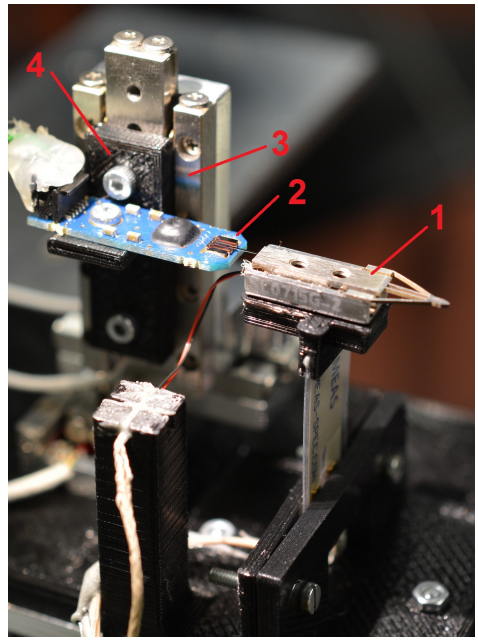

Figure 4.19: Implementation of the calibration set-up. (1) PVDF based force sensing microgripper; (2) Reference force sensor; (3) 3D-Micromanipulator; (4) Connecting-element

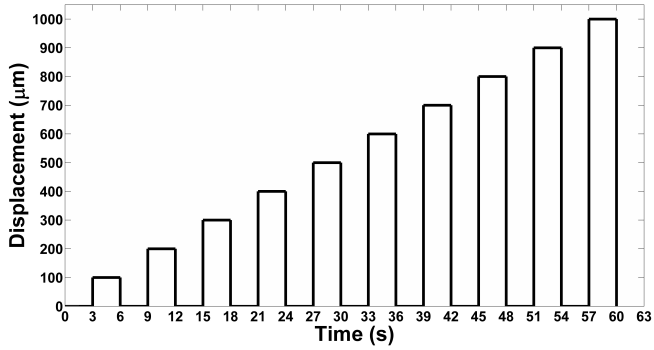

Figure 4.20: Input signal sequence for calibrating the proposed force sensor. A series of ten square pulses of increasing 100 μm amplitude, with the displacement returning to the initial value after each pulse.

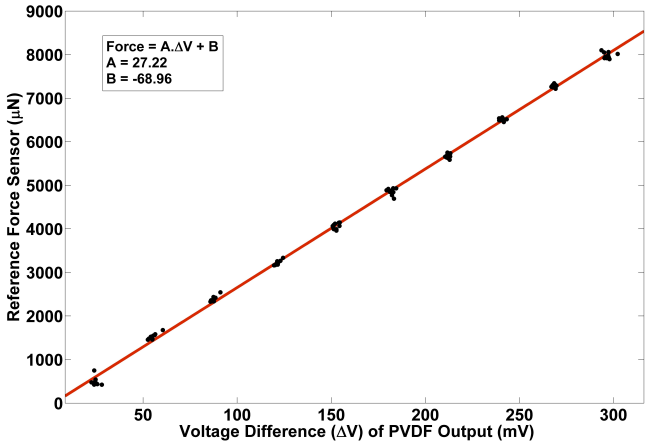

Figure 4.21: Linear calibration curve fit of the PVDF based force sensing microgripper for measuring bond breaking forces in shear-mode.

Table 4.6: Relative standard deviation for the output of the PVDF based force sensing microgripper. The input signal sequence is repeated ten times.

Pulse No.	1	2	3	4	5	6	7	8	9	10
Reference Sensor	19.45	5.89	3.74	2.60	2.14	1.90	1.55	1.21	1.00	0.97
PVDF film Sensor	5.94	4.32	2.54	1.76	1.37	1.17	0.91	0.79	0.66	0.69

Whereas the SG-06 microgripper weighs 2 g and the capacitive reference force sensor probe pushes this relatively heavy weight during calibration process, the first values in the output signal of reference sensor are exaggerated due to the quick and heavy load. Even though a 2nd order Butterworth filter is applied to the reference sensor output data to eliminate the exaggerated peaks, this heavy load leads to the RSD of 19.45% for the 1st input pulse around 0.5 mN. The corresponding RSD for the PVDF film output is 5.94% for the 1st input pulse [see Table 4.6 and Figure 4.21]. After the 2nd input pulse, for the forces higher than 1.5 mN, the RSD of reference force sensor and the PVDF film outputs are less than 5.89% and 4.32%, respectively. The RSD for both reference force sensor and PVDF film is descending while the force values are ascending. The RSDs of the reference and the PVDF sensor are in an acceptable range for forces higher than 2 mN. The linear calibration curve fit indicates 27.22 $\mu N/mV$ sensitivity for the developed force sensing microgripper for measuring bond breaking forces in shear-mode.

Comparing the RSDs of reference force sensor in Table 4.5 and Table 4.6 indicates that for the first input pulse, there is a significant difference between RSDs of the Z-directional sensor (8.16%) and the shear-mode sensor (19.45%). It is noteworthy that the first input pulse in the Z-directional sensor corresponds to 1 mN force while in the shear-mode sensor it corresponds to 0.5 mN. Therefore, regardless of the fact that the 2 g weight of the microgripper significantly contributes to this error, the trend of increase in the error matches the common behavior of the sensors. In order to use these sensors, in both cases, the acceptable force ranges are set so that the RSDs of reference sensors and PVDF film sensors are less than 4% and 3%, respectively. The acceptable force ranges are 3 $mN-10$ mN for the Z-directional sensor and 2 $mN-10$ mN for the shear-mode sensor.

4.3 Development of Microspring based Force Sensing Microgripper

Tensile testing of MF do not need a lot of force to manipulate, but their ultimate tensile strength is very high and relatively large forces are required to perform a micro-scale tensile test, e.g. CNTs require 0.5 mN – 30 mN [116, 117], wood fibers require 40 mN – 370 mN [118] and paper fiber bonds require 0.2 mN – 20 mN [5, 24, 6]. In this section a novel force sensing approach for grippers used in micro-tensile testing applications is proposed.

Even though the proposed force sensing approach in this section is adaptable for the forces in the range of few milliNewtons upto tens of milliNewtons, but considering the required force range for the case study on paper fiber bonds, the developed ElNi microspring based force sensing microgripper is designed to cover the forces up to 20 mN. The working principle of the proposed sensor is based on the hypotheses that the rolling-resistance of a low-friction precision linear slider (PLS) is small enough to allow force measurements in the milli-Newton force range.

4.3.1 Proof of Concept

The force sensing concept is based on exploiting a linear force - displacement range of a microspring, which is constrained to move unidirectionally using a guide-way. In this case the guide-way is a low-friction precision linear slider. The goal of the experiments explained in here is studying the friction behavior of the PLS and proof the concept of the proposed microspring based force sensor. Figure 4.22A illustrates the proposed force sensor. The low-friction precision linear slider (IKO, Japan) C1.-F.4.22A has a coefficient of rolling-resistance of 0.001. Two pins C2.-F.4.22A with a diameter of 0.9 mm are used to mount the microspring C3.-F.4.22A. One pin is mounted on the fixed part of the PLS, a so called stopper C.4-F.4.22A, and another pin on the moving part of the PLS. The stopper is an in-house made component and it is not an

original part of the PLS. Using the mounting rings, the microspring is mounted on the PLS pins by using magnetic tweezers. Figure 4.22B shows the implementation of the proposed force sensor.

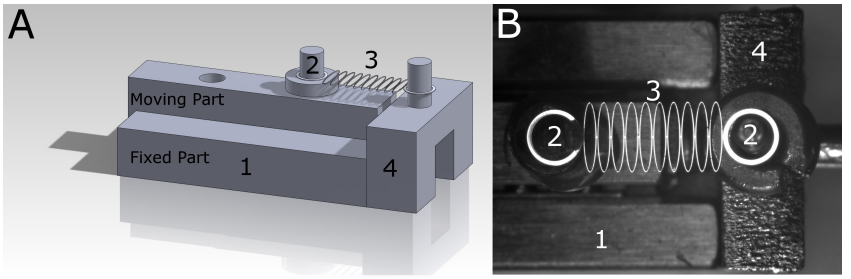

Figure 4.22: (A) Schematic of the force sensor. (B) Top-view of the microspring mounted on the PLS. (1) PLS; (2) Mounting pin; (3) ElNi Microspring; (4) Stopper [7].

Friction Force Study

In order to study the static and dynamic friction forces which resist the movement of the PLS, a test set-up presented in Figure 4.23 is used. A reference force sensor, FT-S10000, is mounted on a linear actuator and it is aligned with the PLS slider. The moving part of the PLS slider and the reference force sensor probe are connected using a small rod. The linear actuator has an integrated position sensor, an optical encoder, with the resolution of 100 nm. Since the reference force sensor probe and the PLS slider are connected, the change in the position of the reference force sensor probe represents the displacement of the microspring. Another option to measure the displacement of the microspring is using a sequence of images from top-view. The first approach, however, offers higher resolution, thus it has been used in these experiments. The microspring is removed from the test set-up, therefore the only present force to resist the movement of the slider is the rolling-resistance. The slider is pushed forward with different velocities. Whereas the tests including the microspring are planned to be performed with velocities of 40 $\mu m/s$, the friction measurements were performed with 40 $\mu m/s$ and 400 $\mu m/s$ velocities. In order to make sure that the friction forces

affect only the lower range of the force measurements, the maximum velocity of the friction measurement experiment was set ten times higher than the maximum velocity of the tests including the microspring. It is noteworthy that since the proposed force sensor is designed for tensile testing and it will be used for unidirectional measurements, only the forward motion of the slider is in the interest of this study. The force is measured using a NI PCI-6259 measurement board (National Instruments Corporation, Texas, USA). Figure 4.24 shows the results of friction measurements. The continuous line and the dotted line illustrate representative friction measurements with velocities of 40 $\mu m/s$ and 400 $\mu m/s$, respectively. The highest peak in each measurement represents the static friction force which is continued with a plateau that represents the dynamic friction force.

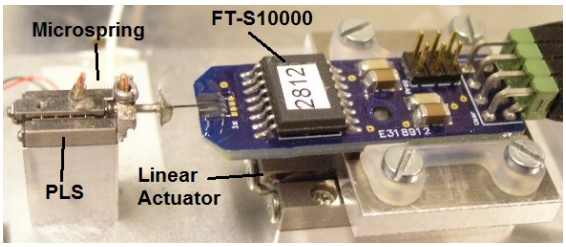

Figure 4.23: The performance characterization setup for the proposed force sensor [7].© *IEEE 2015* Reprinted, with permission, from [P. Saketi, et al., Electroplated Nickel Microspring and Low-Friction Precision Linear Slider: A Novel Micro-Force Sensing Tool, 05/2015].

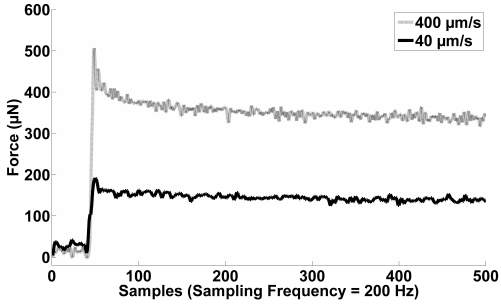

Figure 4.24: Friction measurements of the PLS. The highest peak in each measurement represents the static friction force which is continued with a plateau that represents the dynamic friction force [7].© *IEEE 2015* Reprinted, with permission, from [P. Saketi, et al., Electroplated Nickel Microspring and Low-Friction Precision Linear Slider: A Novel Micro-Force Sensing Tool, 05/2015].

Table 4.7 shows the results of the friction force measurements of the PLS with 40 $\mu m/s$ and 400 $\mu m/s$. The result indicates that the friction inside the PLS leads to uncertainties in the measurement of forces smaller than $500\mu N$; the lower the velocity, the smaller the influence of friction forces on the measurements.

Table 4.7: The results of friction force measurements of PLS with different velocities [7].

Velocity ($\mu m/s$)	40	400
Static Friction Force (μN)	190	510
Dynamic Friction Force (μN)	140	340

Microspring Design and Fabrication

In order to verify if a microspring with a linear force-displacement range is usable for force sensing applications at micro-scale, a microspring is designed, fabricated and integrated into the PLS. Figure 4.25 illustrates the schematic design of the microspring which is made of a chain of elliptical rings. The transverse diameter and the conjugate diameter of the ellipses in the microspring are called ring height (RH) and ring width (RW), respectively. The vertical cross section area of the ring is called microspring gauge and its dimensions are named as gauge width (GW) and gauge height (GH). The links which connect the elliptical rings together have the same cross section dimensions as the microspring gauge.

The elliptical shape of the microspring design is different from the U-shaped and S-shaped reported microsprings [119]. The initiative to select elliptical rings instead of U-shaped and S-shaped ones is the axisymmetry in their geometry, which leads to axisymmetrical distribution of stress in the structure. Therefore, it minimizes the risk of bulging and buckling in the spring structure during loading (tension) and unloading (compression), respectively. Based on the values reported in the literature [60] for the Young's modulus (E =171.5 GPa) and for the Poisson's ratio (ν = 0.3) of ElNi, the effect of variations in RH, RW, GH, GW, the

number of rings and the length of the connection between the rings on the maximum stress and the displacement were studied using ANSYS.

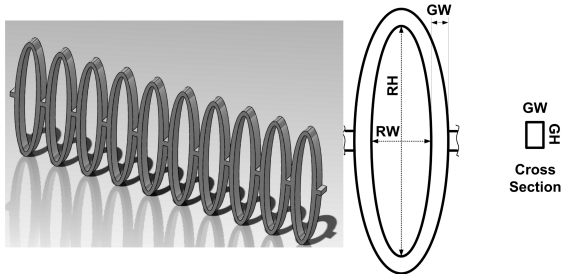

Figure 4.25: Schematic of a microspring. RH: Ring Height, RW: Ring Width, GW: Gauge Width, GH: Gauge Height [7].© *IEEE 2015* Reprinted, with permission, from [P. Saketi, et al., Electroplated Nickel Microspring and Low-Friction Precision Linear Slider: A Novel Micro-Force Sensing Tool, 05/2015].

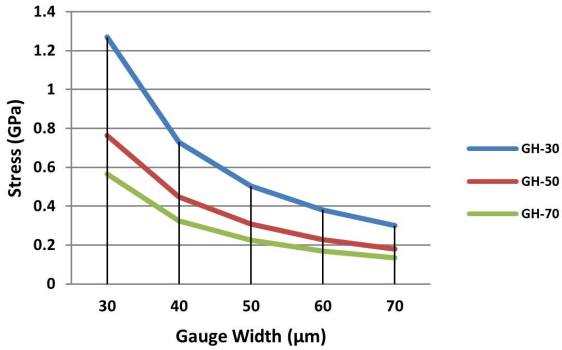

Figure 4.26: Simulation results for 20 mN applied force on the microspring with RH of 1600 μm and RW of 250 μm as a function of GW and GH [7].© *IEEE 2015* Reprinted, with permission, from [P. Saketi, et al., Electroplated Nickel Microspring and Low-Friction Precision Linear Slider: A Novel Micro-Force Sensing Tool, 05/2015].

Based on the simulation results, the RH of 1600 μm, RW of 250 μm, GH of 50 μm and GW of 30 μm are the selected dimensions for the fabrication of the microspring. Figure 4.26 shows simulation results for a 20 mN applied force on the microspring with RH of 1600 μm and RW of 250 μm as a function of GW and GH. It is desirable to achieve the maximum possible elastic range for a microspring under a 20 mN load, which leads to maximum possible linear deformation, and therefore maximum possible sensitivity for the sensor. The maximum stress in a

microspring with GH of 50 μm and GW of 30 μm under a 20 mN load is 0.77 GPa. Considering 1.1 GPa yield strength for the ElNi, the stress value of 0.77 GPa for the selected geometry allows a reasonable linear range for the microspring with a 30% safety threshold that keeps away the microspring from plastic deformations. Simulations also indicate that the effect of the length of connections between two rings on the displacement is negligible, and increasing the number of rings increases the displacement linearly. A microspring is fabricated using UV-LIGA in Research Institute of Micro/Nanometer Science and Technology at Shanghai Jiao Tong University. The fabrication process was explained in Section 2.5 and illustrated in Figure 2.4.

The geometry of the fabricated microsprings is measured using an SEM. Figure 4.27 shows the SEM images of a fabricated ElNi microspring and its cross sections. The SEM images in Figure 4.27B and Figure 4.27C illustrate that the cross section of the fabricated microspring specimen is a trapezoid instead of an ideal rectangle. The trapezoidal cross section is caused by the scattering of the UV light during the lithography process.

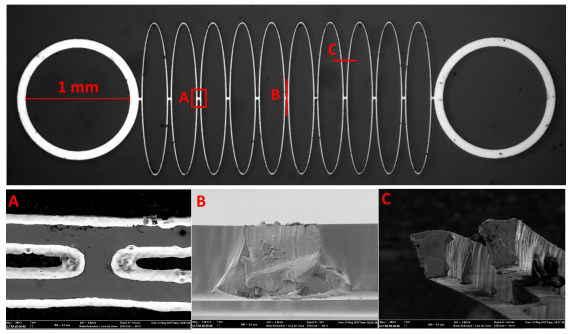

Figure 4.27: SEM images of a fabricated ElNi microspring and its cross sections. (A), (B) and (C) images in the bottom represent the points of interest on the top image [7].© *IEEE 2015* Reprinted, with permission, from [P. Saketi, et al., Electroplated Nickel Microspring and Low-Friction Precision Linear Slider: A Novel Micro-Force Sensing Tool, 05/2015].

The side walls of the trenches in the photoresist are not parallel, which is a drawback of using AZ®50XT thick photoresist in UV-Lithography. Even though microsprings are not ideal because of these geometrical defects, it is still possible to use them to proof the proposed force sensing

concept. The spring fabricated is composed of ten elliptic sensing rings and two circular mounting rings (1 mm in diameter) in the ends of the spring.

Validation of the Concept

In order to validate the proposed force sensing concept, an ElNi microspring is placed between the mounting pins and the slider was moved 150 μm forward and backward ten times, without changing the location of 150 μm travel range. Thus, from the entire 3 mm travel range of the slider only a 150 μm section is used for all of the experiments. In order to have as close conditions as possible to the final microgripper prototype, a 4 g weight is added on the top of the PLS during these experiments. This mass is the equivalent to the mass of the SG-06-EX (SmarAct GmbH, Germany) microgripper. The integration of the SG-06-EX microgripper into the proposed force sensor is presented in Section 4.3.2.

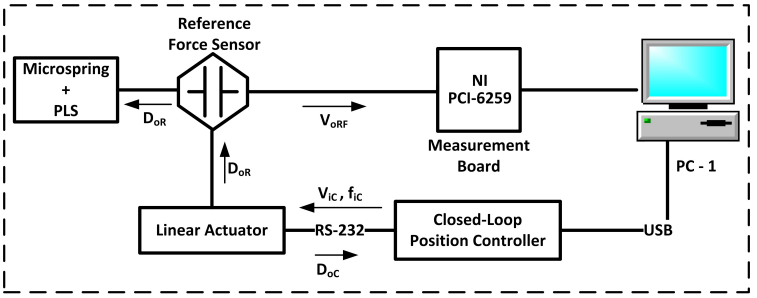

Figure 4.28: Schematic of measurement electronics for validating the concept of microspring based force sensor.

Figure 4.28 illustrates the schematic of measurement electronics for validating the concept of the microspring based force sensor. A CU-3DM control module (Smaract GmbH, Germany) is used to control the linear actuator, which is connected through a USB port to a computer. The linear actuator is controlled by tuning the actuation voltage, V_{iC}, and actuation frequency, f_{iC}, of a piezo-drive. An optical encoder is used as a position feedback sensor, D_{oC}. The linear actuator, the reference force sensor and the microspring are in mechanical contact. Thus, the

displacement of linear actuator, D_{oR}, and the microspring are identical. The force is acquired by measuring the reference force sensor output voltage, V_{oRF}, times the sensor gain. The force-displacement measurements are acquired by synchronized measurement of (i) force, V_{oRF}, using the NI PCI-6259 measurement board and (ii) displacement, D_{oC}, using the CU-3DM control module.

Figure 4.29 shows the results of force-displacement measurements when an ElNi microspring is integrated into the PLS. The measurements are performed with the velocity of $40\mu m/s$. As the proposed force sensor is unidirectional, only the tension forces are shown in Figure 4.29, and the measurements from the release of the forces are not presented.

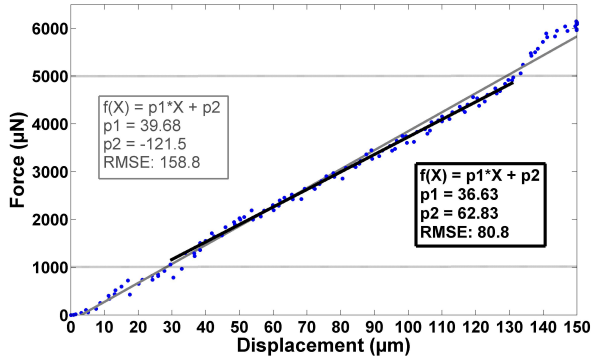

Figure 4.29: Force – Displacement measurement of an integrated ElNi microspring inside a PLS. The grey line includes all data points while the black line includes only the data points in the range of 1000 μN – 5000 μN [7].© *IEEE 2015* Reprinted, with permission, from [P. Saketi, et al., Electroplated Nickel Microspring and Low-Friction Precision Linear Slider: A Novel Micro-Force Sensing Tool, 05/2015].

The gray line in Figure 4.29 is fitted to the all data points from the measurement having a slope of 39.68 N/m and the root-mean-square-error (RMSE) of 158.8 μN. While the force measurements below 500 μN are influenced by friction forces, both static and dynamic friction, the force measurements below 1000 μN are influenced by the acceleration of the actuator starting from zero velocity. Considering the last part of the measurement in Figure 4.29, for forces higher than 5000 μN, the deceleration of the actuator reaching the stop point at 150 μm also

causes non-linearity in the results. Therefore, in the force range of 1000 μN – 5000 μN only the dynamic friction of PLS influences the measurement result. The black line in Figure 4.29 is fitted only to the data points in the range of 1000 μN – 5000 μN with the slope of 36.63 N/m and the RMSE of 80.8 μN. Thus, the line fitting error in the force range of 1000 μN – 5000 μN is half of the full range error.

Table 4.8 illustrates the uncertainty in the force – displacement measurements of the ElNi microspring integrated inside the PLS calculated from ten measurements. In order to measure the uncertainties in the exact displacement points, the linear actuator moves the slider to the exact position, pauses and comes back to the zero position. This means that the reported force values and the standard deviations (STD) include the deceleration non-linearity error caused by the stopping of the linear actuator. Therefore, technically the measured STD in the constant velocity zone can be smaller than the reported STDs in Table 4.8 .

Table 4.8: Uncertainty in the Force - Displacement measurements of ElNi microspring integrated inside the PLS [7].

Target Displacement [$Measured$] (μm)	Displacement STD (μm)	Displacement RSD (%)	Mean Force (μN)	Force STD (μN)	Force RSD (%)
30 [29.9]	0.2	0.6	1096.6	142.0	13.0
60 [59.9]	0.3	0.4	2104.9	109.5	5.2
90 [89.8]	0.2	0.2	3252.9	105.4	3.2
120 [120.0]	0.1	0.1	4476.1	138.1	3.1
150 [149.9]	0.2	0.1	6052.7	77.3	1.3

The reason for measuring the uncertainties by moving the slider to the exact position and pausing instead of measuring the uncertainties directly from the constant velocity zone is the control module of the linear actuator which is connected through the USB port to the computer. The USB port causes a bottle-neck of few hundred Hertz sampling frequency to the position measurement which is not sufficient to extract high sampling frequency real-time data on a moving actuator. The highest measured RSD for the displacement measurement is 0.6% which is the result of using the linear actuator with 100 nm resolution. The measured RSDs for the force values indicate that the higher the measured force the

better the accuracy is. Even though a RSD of 13% for the force measurements around 1000 μN is far from ideal, a RSD of around 3% or less for the forces higher than 3000 μN is acceptable in the micro-tensile testing applications. It should be noted that the linear actuator is working using a stick-slip piezo-drive and therefore, in addition to the aforementioned sources of error, the error caused by the stick-slip phenomena is present in the entire experiments.

The results from the experiments demonstrate that the proposed force sensor using ElNi microspring and the PLS can be used as a new tool in micro-force sensing applications for forces higher than a couple of thousands of micro-Newton, and the hypothesis that the rolling-resistance of a PLS is small enough to allow force measurements at micro-scale is a valid argument for a specific force range. In the proposed force sensing approach, the side effects of friction forces on the force measurements are small enough to make this approach reasonable.

Even though the force range of the fabricated microspring is limited to 6 mN, the proposed approach allows for the fabrication of ElNi microsprings for the forces up to tens of milliNewtons for micro-tensile testing of various materials. There are three methods to increase the linear force range of ElNi microsprings: changing the plating temperature, changing the current density and changing the GW. According to reported results in [110], 20 $^{\circ}C$ change in plating temperature affects Young's modulus by 15%, and 25 mA/Cm^2 change in current density affects Young's modulus by more than 50%. The benefit of changing the force range of ElNi microspring by either the plating temperature or the current density is the possibility of keeping the microspring geometry constant [7]. Thus, when a change in the force range is required only the spring should be changed and the rest of components in the micro-force sensor can remain the same. Considering the rectangular cross-section area and its corresponding moment of inertia of a microspring, the most effective way to change the linear force range of the microspring is changing the GW which affects the force range by three orders of magnitude.

4.3.2 Electroplated Nickel Microspring based Force Sensor

In the next phase of this study, an ElNi microspring for the force range of 0 $mN - 20$ mN is modeled using ANSYS and fabricated using UV-Lithography.

Microspring Design Optimization

The goal is to design a sensor with a sensitivity of 40 $\mu N/\mu m$. Therefore, a microspring with 500 μm linear deformation under 20 mN load should be designed. The microspring should tolerated 20% of overloading for safely. In order to optimize the design of the microspring in ANSYS, *subproblem approximation method* is used to solve a constrained optimization problem. Subproblem approximation is a very well established method [126, 127, 128, 129] which is only used as a tool in this thesis. In the optimization algorithms, the constrained optimization problem is converted to an unconstrained problem using penalty functions [129]. In order to optimize a design, the objective function which contains the state variables and the design variables is minimized.

$$Min.\ F = F(x) \tag{4.1}$$

The dependent variables can be expressed by approximations, and a fully quadratic representation including cross terms approximates the objective function [129].

$$\hat{F} = a_0 + \sum_{i}^{n} a_i x_i + \sum_{i}^{n} \sum_{j}^{n} b_{ij} x_i x_j \tag{4.2}$$

A weighted least squares technique is used to calculate the a_i and b_{ij} coefficients [129]. The constrained minimization problem in Equation. 4.2 is converted to an unconstrained problem using penalty func-

tions shown in Equation 4.3. In order to apply the design variable constraints, X is used as the penalty function. Similarly, G, H and W are penalty functions for state variable constraints. The penalty functions are minimized until the solution converges, or the iterations are terminated [129].

$$F(x,P_k) = \hat{F} + F_0 P_k \left(\sum_{i=1}^{n} X(x_i) + \sum_{i=1}^{m_1} G(\hat{g}_i) + \sum_{i=1}^{m_2} H(\hat{h}_i) + \sum_{i=1}^{m_3} W(\hat{w}_i) \right) \quad (4.3)$$

The goal of this study is to find the GH and the GW of the microspring under the following conditions:

- Based on the fabrication limitations, GH and GW should be in the range of 5 μm – 150 μm.
- The acceptable maximum stress in the entire spring structure should be less than 80% of the yield strength 1.1 GPa.
- 500 ± 10 μm displacement for the applied force of 20 mN

Table 4.9 summaries the parameters for the optimization of the microspring. In order to decrease the computation load and time, since the elliptical rings in the microspring are axisymmetric, only a quarter of an entire ring is modeled. Table 4.10 summarizes the feasible sets of the optimization results. In order to fabricate the microsprings, it is possible to either use UV-lithography or X-ray lithography. The X-ray lithography provides higher certainty on the geometry of the fabricated microsprings than UV-lithography, but the mask for X-ray lithography is ten times more expensive than the mask for UV-lithography. Therefore, despite the fact that X-ray lithography provides higher quality, the microsprings were fabricated using UV-lithography in Microworks GmbH, Germany.

Table 4.9: Summary of parameters for optimization of microspring.

Variables	**Parameter**	**Minimum**	**Maximum**
Design Variable	Gauge Width (GW)	5 μm	150 μm
Design Variable	Gauge Height (GH)	5 μm	150 μm
State Variable	Maximum Displacement (U_{max})	490 μm	510 μm
Objective Function	Maximum Stress (σ_{max})	–	0.88 GPa
Constants	**Value**	–	–
Young's Modulus (E)	180 GPa	–	–
Yield Strength (σ_y)	1.1 GPa	–	–
Poisson's Ratio (ν)	0.3	–	–
Ring Height (RH)	1600 μm	–	–
Ring Width (RW)	250 μm	–	–

Table 4.10: Summary of optimization results.

Feasible Set No.	1	2	3	**4**
GW (μm)	23.5	24.8	24.4	**26.8**
GH (μm)	147.8	126.2	131.3	**99.7**
$\sigma_{max}(GPa)$	549.7	577.1	575.4	**625.5**

Since the maximum recommended height for structures fabricated using UV-lithography is 100 μm, the design values of Column 4 in Table 4.10 are used. During fabrication of the microspring for proof-of-concept in Shanghai Jiao Tong University positive photoresist was used, but for fabricating the microsprings with optimized design in Microworks GmbH negative photoresist is used. After releasing the microsprings from the substrate, the side which has been in contact with the substrate is called "bottom" and the side which has not been in contact with the substrate is called "top". Consequently, the width, GW, of the microspring on the side that has been in contact with the substrate is called "bottom value" and the other side is called "top value". From prior fabrication experiments [130], it is known that compared to the design values, there is about 37% width reduction for the mean value of Ni; about 20% width reduction on the top value and about 53% width reduction on the bottom value. In order to achieve the desired GW, four

microsprings with GW's of 27 μm, 32 μm, 37 μm and 42 μm are designed as it is shown in Figure 4.30. Since all of these four designs are fabricated in one batch, in order to differentiate between the microsprings with the naked eye, small wings are added to the mounting rings.

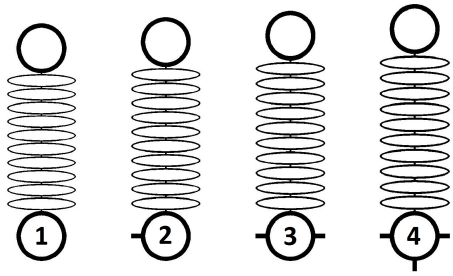

Figure 4.30: Designed microsprings. (1) GW = 27 μm; (2) GW = 32 μm; (3) GW = 37 μm; (4) GW = 42 μm.

Microspring Validation

Figure 4.31 represents a fabricated microspring with optimized design. The rough geometry of the upper edges is caused by the wet chemical removal of the seed layer which can be minimized in future [8]. There is also a small deviation in line width between individual lines of the spring elements which most likely it is due to a periodic error in the repeatability of the patterning system [8]. As it was mentioned above, a difference in line width between the upper and lower surface of the microspring can be observed [8] which are reported in Table 4.11. Consequently, the microspring with the GW design value of 42 μm, and the fabricated GW mean value of 36.5 μm is used to build the force sensor.

The ElNi Young's modulus used during the modeling phase was 180 GPa. In order to validate the Young's modulus of ElNi, five specimens with the dimensions of 13 $mm \times 1.2\ mm \times 0.1\ mm$ have been integrated into the UV-lithography mask of microsprings and fabricated with the same batch. These five specimens were distributed evenly over the mask to provide a reliable average value of Young's modulus. The tensile testing of the specimens were performed in the laboratory of Department of Solid Mechanics at KTH, Sweden. The results indicate that the average

Young's modulus of fabricated ElNi microsprings is 172 $GPa \pm 5\%$ which is 4.4% less than the 180 GPa used in the ANSYS model.

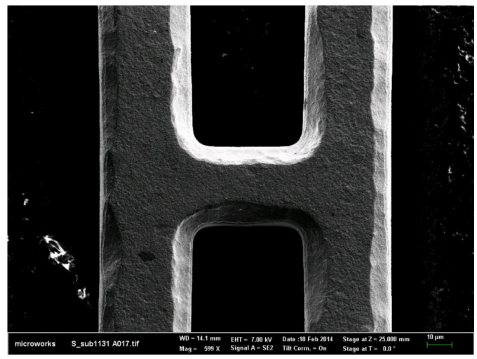

Figure 4.31: SEM image of a fabricated microspring for the measurement of the top values and the bottom values of GW. The rough geometry of the upper edges is caused by the wet chemical removal of the seed layer [8]. © *Courtesy of MicroWorks GmbH.*

Table 4.11: Summary of optimization results.

Spring Type	Mean Top	Width Reduction	Mean Bottom	Width Reduction
GW = 27 μm	21.9 μm	19%	14.8 μm	45%
GW = 32 μm	26.5 μm	17%	21.3 μm	33%
GW = 37 μm	31.5 μm	15%	28.5 μm	23%
GW = 42 μm	38.2 μm	9%	34.8 μm	17%

Integration

Figure 4.32 illustrates a schematic design of the microspring based force sensing microgripper. The microgripper SG-06-EX (SmarAct GmbH, Germany), C.5-F.4.32, is attached to the PLS, C.1-F.4.32, using a connecting-element, C.6-F.4.32. In order to measure the displacements of the PLS, a magnetic encoder (NSE-5310, AMS, Austria), C.7-F.4.32, with 0.488 μm resolution is used. A multipole magnet strip (AS5000-MS10-300, AMS, Austria), C.8-F.4.32, with pole pair length of 2 $mm \pm 1.2\%$ is attached under the connecting-element to derive the incremental position of the magnetic strip using a Hall element array on the chip of NSE-5310 magnetic encoder. This Hall sensor array detects the ends of the magnetic

strip to provide a zero reference point. It also provides absolute position information over the length of the magnet pole pair. It is possible to achieve absolute position information over the entire length of the magnetic strip by counting the pole pairs [131].

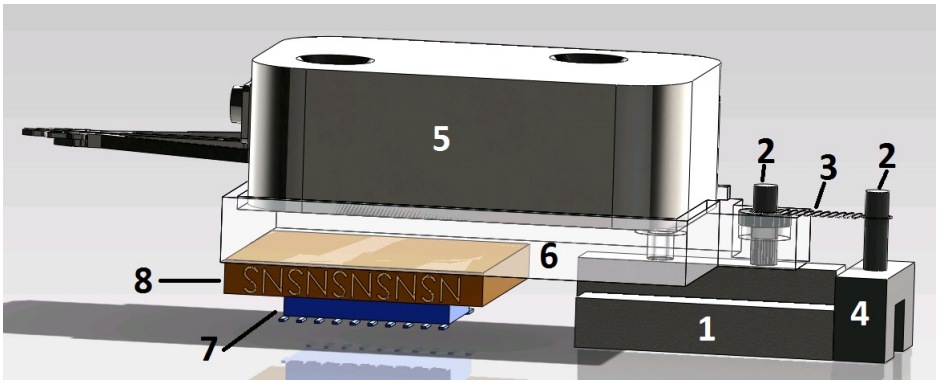

Figure 4.32: Schematic design of microspring based force sensing microgripper. (1) PLS; (2) Mounting pin; (3) ElNi Microspring; (4) Stopper; (5) Microgripper, (6) Connecting-element, (7) Magnetic Encoder, (8) Multipole magnet strip.

Figure 4.33 shows the implementation of the microspring based force sensing microgripper. The numbering is the same as Figure 4.32 with the exception of C.4-F.4.33 which is the stand and C.9-F.4.33 which is assigned to the adjusting screws. The adjusting screw in the back is used for fixing the zero point of the travel range and to secure the microspring from buckling. The adjusting screw in the front is used to fix the end point of the travel range and to secure the microspring from hypertension and plastic deformation. The NSE-5310 is soldered on the top of a PCB C.7-F.4.33. The gap between the multipole magnet strip, C.8-F.4.33, and the magnetic encoder is adjusted to be less than 300 μm as it was required [131].

Calibration

In order to evaluate the positioning repeatability of the NSE-5310 magnetic encoder, an SLC-1730 linear actuator is attached to the movable

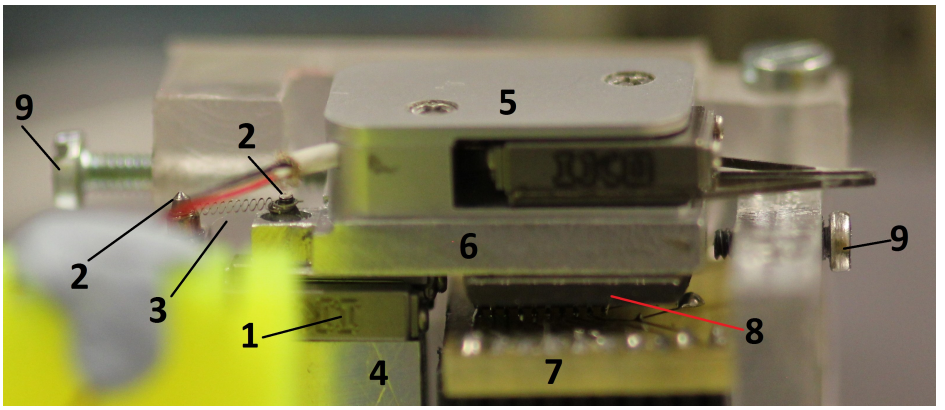

Figure 4.33: Implementation of microspring based force sensing microgripper. (1) PLS; (2) Mounting pin; (3) ElNi Microspring; (4) Stand; (5) Microgripper, (6) Connecting-element, (7) Magnetic encoder soldered on PCB, (8) Multipole magnet strip, (9) Adjusting screws.

part of the PLS using a solid connecting rod. The linear actuator has an integrated optical encoder with a 100 nm resolution and a ± 1 μm repeatability, which is used as a reference position sensor, D_{oC}. The linear actuator, the microspring, the connecting-element and the magnet strip are in mechanical contact. Thus, the displacement of the linear actuator, D_{oR}, and the magnet strip are identical. The output of the magnetic encoder, D_{oM}, is recorded to a computer through a USB-I2C interface adapter (Devantech Ltd, UK). The linear actuator and its optical encoder are connected to another computer using an SCU-3DM control rack and a USB connection [see Figure 4.34]. In order to validate the performance of the magnetic encoder, D_{oC} and D_{oM} are recorded and studied. In order to check the repeatability of the magnetic encoder, the magnetic strip which is connected to the PLS is moved from zero position to 50 μm, 250 μm and 500 μm one hundred times and they are compared with the reference position sensor. The results are summarized in Table 4.12. The results show that the offset values of the magnetic encoder from target positions for 50 μm, 250 μm and 500 μm are 0.58 μm, 2.75 μm and 4.87 μm, respectively. Since the offset at all three target positions is around 1%, it implies that there is a small misalignment between the magnetic strip and the magnetic encoder because of mechanical

tolerances during fabrication and installation.

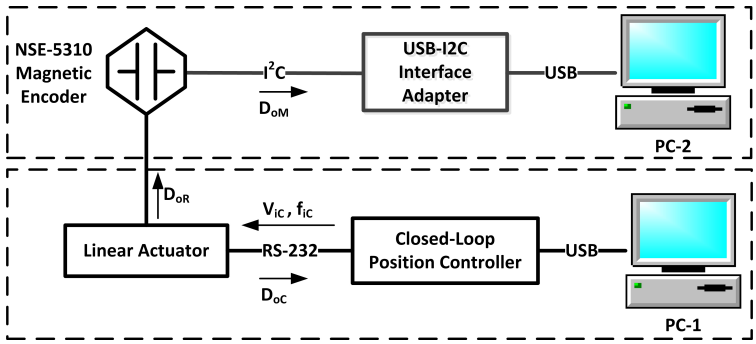

Figure 4.34: Schematic of the measurement system for evaluating the positioning repeatability of NSE-5310 magnetic encoder.

Table 4.12: Repeatability of NSE-5310 magnetic encoder (D_{oM}) compared to the reference SLC-1730 optical encoder (D_{oC}).

Target Position	Reference (Mean)	Reference (STD)	Offset	NSE-5310 (Mean)	NSE-5310 (STD)	Offset
0	0.06	0.09	0.06	0.08	0.17	0.08
50	49.98	0.09	0.02	49.42	0.26	0.58
250	249.99	0.18	0.01	252.75	0.51	2.75
500	499.96	0.09	0.04	504.87	0.34	4.87

A calibration setup similar to Figure 4.23 is used to calibrate the microspring based force sensing microgripper. The linear actuator moves the microgripper forward and backward with a ramp input ten times to calibrate the sensor. Figure 4.35 shows the schematic of measurement system for calibrating the microspring based force sensing microgripper. The reference force ($V_{oRF} \times SensorGain$) and reference displacement (D_{oC}) are measured synchronously using an FT-S10000 reference force sensor and the optical encoder of linear actuator, respectively. The magnetic encoder output (D_{oM}) is acquired using a USB-I2C interface adapter (Devantech Ltd, UK). Figure 4.36 shows the calibration curve of the microspring based force sensing microgripper. Whereas the force range of the reference sensor is 10 mN, the forces higher than this value

can not be measured. The forces less than 4500 μN can be measured but they are left out of the calibration data due to non-linearity and offset that the wiring causes. In Section 4.3.1 it was shown than the friction in the PLS contributes to about 500 μN of the error, therefore it is possible to contemplate that the error caused by wiring is about 4000 μN. The sensitivity of the microspring based force sensing microgripper is 91.17 $\mu N/\mu m$. The RMSE of the curve fit is 184 μm which means that the error at the lower end of calibration curve is 4% and at the higher end of calibration curve is less than 2%. Repeatability of the sensor is calculated according to Equation 4.4, and defined in [132] as follows: repeatability is the ability of a sensor to give the same output for repeated applications of the same input value [132]. In this case the number of repetitions are 10 times and the repeatability in the middle of the sensor's force range is 5.6%.

$$Repeatability = \frac{max. - min.\ values\ given}{full\ range} \times 100 \tag{4.4}$$

Since the force range microspring was designed for up to 20 mN force range, it can not be experimentally calibrated for the entire force range due to lack of a proper reference force sensor. Assuming that the microspring behaves linearly, it is possible to extrapolate the calibration curve up to 20 mN. Figure 4.37 illustrates the extrapolated calibration curve. It shows that for 180 μm displacement the corresponding force value is 20 mN. The optimized design of microspring was aimed at 500 μm displacement for 20 mN force to achieve a sensitivity of 40 $\mu N/\mu m$. There are three main reasons which deviate the fabricated microspring based force sensing microgripper from its optimized design values:

- The wiring of the microgripper is introducing a major offset to the force range and also it decreases the sensitivity of the sensor significantly.
- The side wall angles of fabricated ElNi microspring result in a

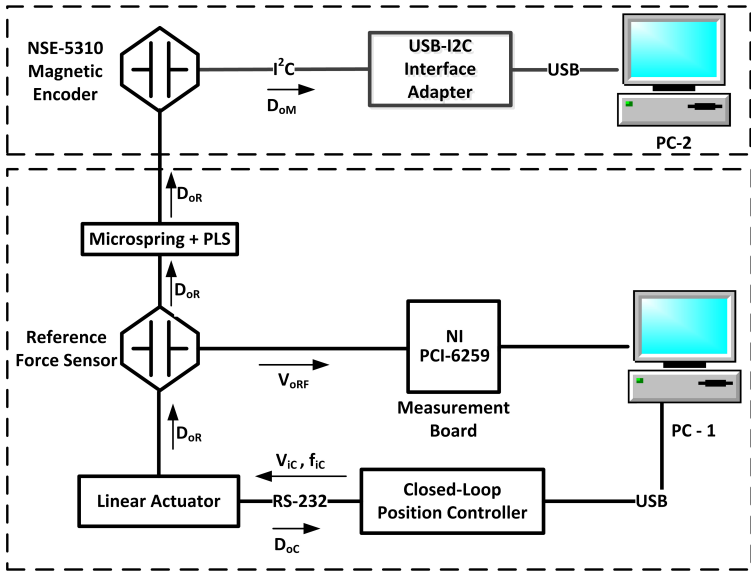

Figure 4.35: Schematic of measurement system for calibrating the microspring based force sensing microgripper.

trapezoid cross section instead of a rectangular one, which affects the area moment of inertia, and ultimately the displacement.

- The mounting pins are custom-made without micro-machining tools. Miss-alignments of microspring between the mounting pins affects both the force range and displacement.

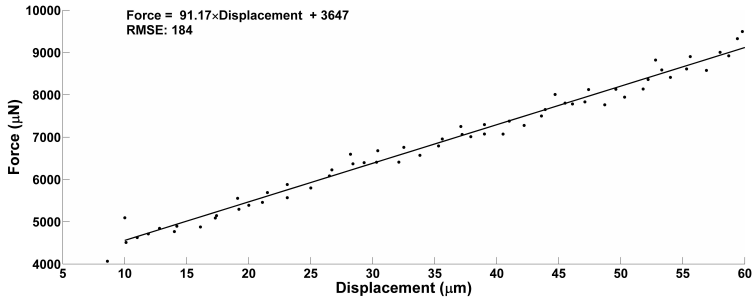

Figure 4.36: Calibration curve of microspring based force sensing microgripper.

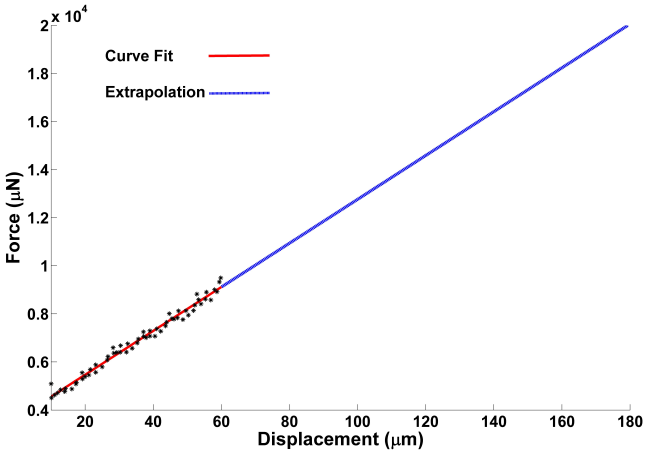

Figure 4.37: Extrapolated calibration curve of microspring based force sensing microgripper.

4.4 Discussions

The bond breaking force range estimation in 4.1 implies that the forces are in the range of 0.1 $mN - 13$ mN which is in a good agreement with the results reported in the literature [27, 26]. In some studies [24, 26], the reported bond breaking force range is as high as up to 20 mN for some samples. Therefore, the required force range to design the force sensing microgripper is 0.1 $mN - 20$ mN.

After the force range estimation two microgrippers were developed; one with a passive specimen holder for Z-directional bonding force measurement and another one with an active microgripper for shear-mode bonding force measurement. These two PVDF based sensors lack the capability of reporting the strain independently, but they can report the force-displacement curves.

A third force sensitive microgripper was also developed for micro tensile-testing of fibrous materials utilizing an elliptical microspring which can report the strain values as well as the force values. Therefore, if the cross section area of the specimen is known it can report the stress-strain curves. During the development phase of this microgripper, it was

shown that rolling-resistance and friction of a PLS can be small enough to allow force measurements in micro-scale.

Table 4.13 summarizes the performance of the developed force sensing microgrippers. The repeatability of the force sensors are calculated according to Equation 4.4 in the middle of their force range. Since these sensors are developed as prototypes for proof of concept, it is acceptable to use this approach to report their repeatability. If these sensors are going to be developed further as products, it is required to perform an uncertainty analysis according to Guide to the Expression of Uncertainty in Measurement (GUM) published by International Bureau of Weights and Measures (BIPM) and ISO 5725.

Table 4.13: Summary of Performance of the Developed Force Sensing Microgrippers.

Microgrippers	Sensor Technology	Acceptable Range	Sensitivity	Repeatability
Z-directional	PVDF	3 mN – 10 mN	51.25 $\mu N/mV$	2.7%
Shear-mode	PVDF	2 mN – 10 mN	27.22 $\mu N/mV$	1.9%
Micro-Tensile Testing	Microspring	4.5 mN – 20 mN*	91.17 $\mu N/\mu m$	5.6%

*Validated range: 4.5 mN – 10 mN

The integration of these three microgrippers into the microrobotic platform is explained in the next chapter.

5 Microrobotic Platform for Characterization of Fibers

In this section, the tools and devices which were developed in Chapter 4 are used to characterize fibrous materials such as pulp fiber bonds and textile fibers. First, the PVDF force sensor with passive specimen holder developed in Section 4.2.2 is used for Z-directional bonding force measurement. Then PVDF based force sensing microgripper developed in Section 4.2.3 is used for shear-mode bonding force measurement. Finally, the microspring based force sensing microgripper developed in Section 4.3 is used for characterizing regenerated cellulose fibers.

5.1 Z-directional bonding force measurement

In order to measure the Z-directional bonding force of pulp samples, a stack of the bond-holders is placed on the microrobotic platform described in Chapter 3 and reported in [2, 4]. This is used for mounting the fiber bonds on the bond-holders. A microgripper with a 3D-micromanipulator is used to grasp a fiber bond and bring it close to the bond-holder [see Figure 5.1A]. UV-curable glue is added to one side of the bond-holder, the end of the fiber bond is placed inside the glue and then the glue is cured [see Figure 5.1A and B]. The microgripper releases the fiber bond, after which a probe which is attached to

a 3D-micromanipulator places the other end of the fiber bond in the UV-curable glue [see Figure 5.1B], and then the glue is cured [see Figure 5.1C].

The PVDF film force sensor is placed on the XY-table of the microrobotic platform described in Chapter 3 and reported in [5, 6]. The bond-holder is placed manually inside the connecting-element using tweezers. Both free ends of the fiber bond are grasped using two microgrippers [see Figure 5.1] and moved synchronously in the loading direction of the PVDF film until the bond breaks. The calibration curve shown in Figure 4.17 is rate-dependent, and the fiber bond is therefore broken using the same velocity as the calibration velocity, 4 mm/s.

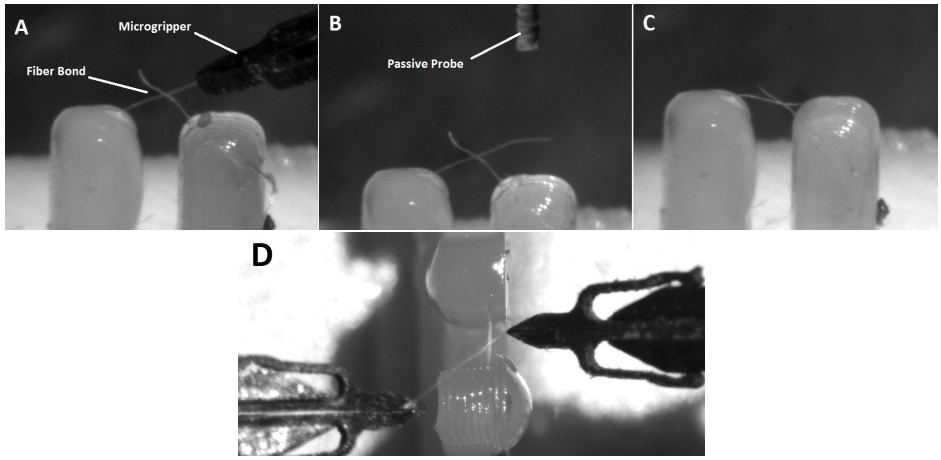

Figure 5.1: Fiber bond mounting and Z-Directional fiber bond strength measurement processes. (A) One end of the fiber bond is placed inside the UV-curable glue using a microgripper. (B) The glue is cured using a UV torch. The other end of the fiber bond is placed inside the glue using a probe. (C) The glue is cured using a UV torch. The fiber bond is mounted on the bond-holder successfully. (D) Z-Directional fiber bond strength measurement.

The voltage out put of the PVDF film is used to calculate the breaking force as described in Equation 5.1 according to Figure 4.17. The displacement is measured based on the microgripper displacement using the in-built optical encoder of linear actuators. Therefore, it is possible

to plot the force-displacement curve for Z-directional bond strength measurement, but it is not possible to report the strain values using this setup.

$$Force = 51.25\Delta V - 359.2 \tag{5.1}$$

Figure 5.2 shows a representative result from a Z-Directional bond strength measurement. The bonds were made using the traditional approach mentioned in Section 2.1.2. The offset of the PVDF film sensor has been removed from the results. Since there is no plastic deformation before the failure point, it is concluded that the fiber bond has failed under brittle conditions. Using this measurement set-up, a set of measurements were done using two types of softwood pulp samples (5 bonds per sample): unrefined bleached softwood Kraft pulp, and refined bleached softwood Kraft pulp with 100 kWh/t specific refining energy [133]. The bonded areas were measured based on the pixel counts from the bond images taken from the top-view. The results indicate that the Z-directional bond strength values for the first sample is 1.44±0.49 N/mm^2 and for the second sample is 2.76±0.64 N/mm^2 [133]. This result suggests that refining with 100 kWh/t specific energy can increase the Z-directional bonding strength of bleached softwood Kraft pulp by 47.8%.

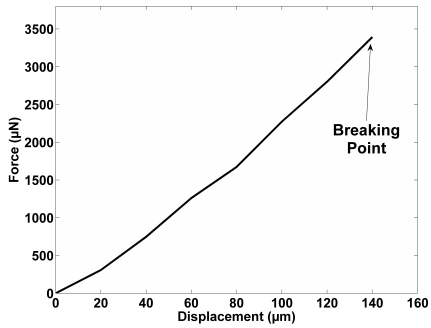

Figure 5.2: A representative graph of Z-directional bond strength measurement.

Since the 4 mm/s deformation rate is close to the burst measurements rates, it is preferred to measure the Z-directional bond strength with smaller deformation rates. In addition, studying the effect of deformation rates on the Z-directional bond strength is of interest. Therefore, further studies were done in order to calibrate the PVDF sensor with smaller deformation rates down to 580 $\mu m/s$ [134]. The bottleneck of calibrating the PVDF film for the deformation rates of few micrometer per second is the bandwidth of the measurement board. This can be achieved by optimizing the capacitor and the resistor of the charge amplifier in the measurement board in future.

5.2 Shear-mode bonding force measurement

The PVDF based force sensing microgripper developed in Section 4.2.3 is integrated in the microrobotic platform as shown in Figure 5.3. C.1-F.5.3 and C.2-F.5.3 are the microgrippers attached to the 3D-micromanipulators. C.3-F.5.3 is the elevated rotary-table which facilitates approaching the samples by the microgrippers, and C.4-F.5.3 is the XY-table. C.5-F.5.3 is the PVDF based force sensing microgripper.

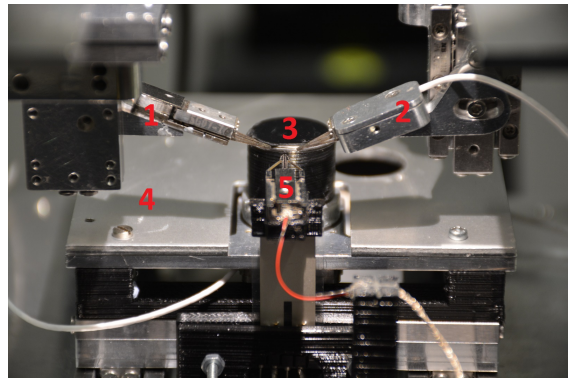

Figure 5.3: Microrobotic platform for shear-mode bonding force measurement. (1) and (2) the microgrippers; (3) the elevated rotary-table; (4) the XY-table; (5) the PVDF based force sensing microgripper.

In order to perform a bonding force measurement in the shear-mode,

the microgrippers take a fiber bond from the rotary-table and bring it to the proximity of the PVDF based force sensing microgripper as shown in Figure 5.4A. The PVDF based force sensing microgripper grasps the free end of the crossing fiber [see Figure 5.4B]. In order to break the bond, the microgrippers C.1-F.5.3 and C.2-F.5.3 move away from the force sensing microgripper synchronously [see Figure 5.4C]. The bonding forces are calculated based on the calibration curve given in Figure 4.21 and Equation 5.2.

$$Force = 27.22\Delta V - 68.96 \tag{5.2}$$

Similar to the Z-directional bonding force measurement, the displacement in this case is also measured based on the microgripper displacement using the in-built optical encoder of the linear actuators. Even though it is possible to report the force-displacement curve for shear-mode bond strength measurement as well, this set-up does not have the means to report the strain values independently.

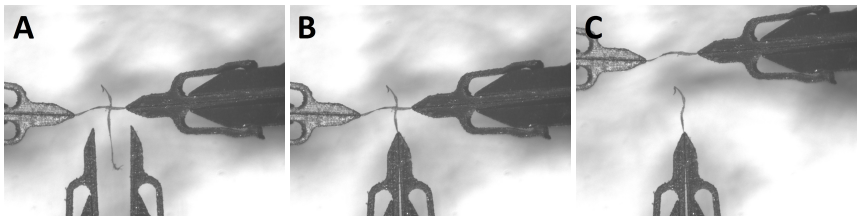

Figure 5.4: Shear-mode bonding force measurement process. (A) Microgrippers bring a fiber bond to the proximity of the PVDF based force sensing microgripper; (B) PVDF based force sensing microgripper grasps the free end of crossing fiber; (C) The microgrippers move away from the force sensing microgripper synchronously to break the bond.

Using this measurement set-up, bonding strength of the same two samples - unrefined bleached softwood Kraft pulp, and refined bleached softwood Kraft pulp with 100 kWh/t specific refining energy - were measured. The bonds were made using the traditional approach. Figure 5.5

illustrates the surface structure of a refined versus an unrefined samples. The fibrillated surface of the refined sample is visible in the image.

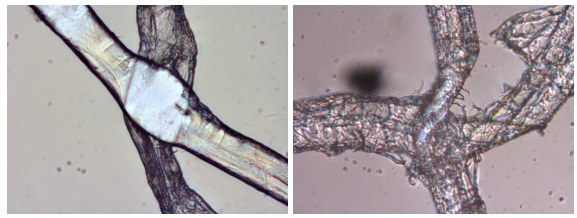

Figure 5.5: Left: A bond made of unrefined fibers. Right: A bond made of refined fibers.

In total, 25 bonds were measured per sample. The bonded areas were measured based on the pixel counts from the bond images taken from the top-view. The results indicate that the average shear-mode bond strength values for the unrefined sample is 0.83 N/mm^2 and for the refined sample is 0.96 N/mm^2. This result suggests that refining with 100 kWh/t specific energy can increase the shear-mode bonding strength of bleached softwood Kraft pulp by 13.5%. Figure 5.6 illustrates the distribution of the results. Since the bonds were made using the traditional approach, there is a possibility of torsional loading combined with loading in the shear direction. Therefore, it is highly recommended to use the perpendicular bond making approach described in Section 3.4 in the future.

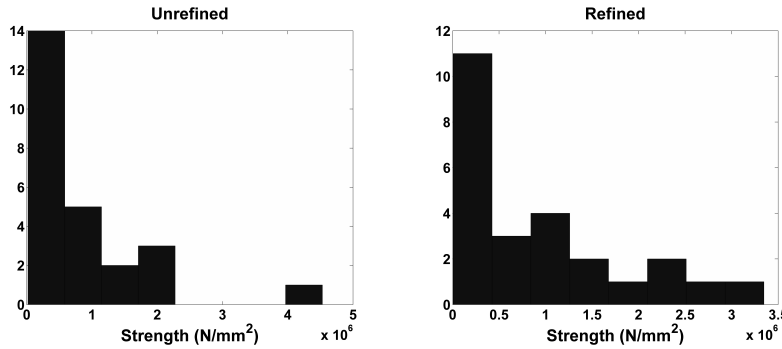

Figure 5.6: Distribution of shear-mode bond strength measurement results.

It is generally accepted that the force required to break a fiber is higher than the force required to break a bond. During the this experiment few controversial cases were seen such as the one in Figure 5.7 where the bond is stronger than a fiber. In Figure 5.7 the fiber is breaking due to a kink.

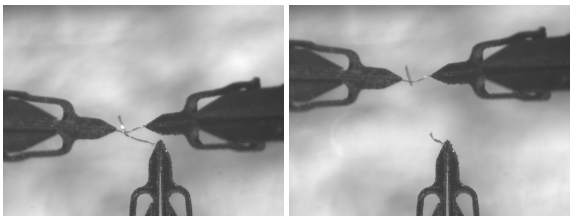

Figure 5.7: The controversial case of a bond which is stronger than a fiber.

5.3 Micro tensile-testing of fibrous materials

Figure 5.8 shows the microspring based force sensing microgripper, described in Section 4.3, integrated into the microrobotic platform described in Chapter 3. C.1-F.5.8 is the microspring based force sensing microgripper. C.2-F.5.8 is the ElNi microspring, C.3-F.5.8 is the magnetic encoder soldered on a PCB and C.4-F.5.8 is the adjusting screw. C.5-F.5.8 is the microgripper attached to a 3D-micromanipulator for pulling the sample during tensile testing.

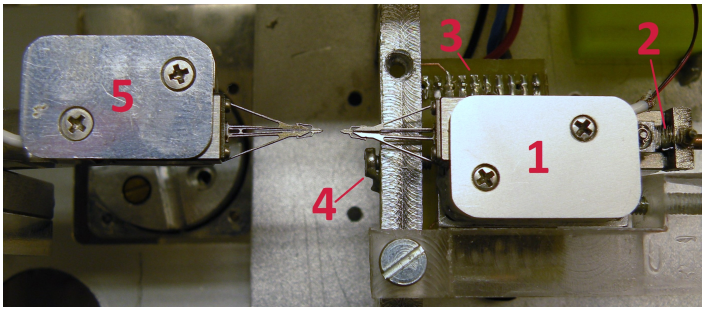

Figure 5.8: Micro tensile-testing setup. (1) Microspring based force sensing microgripper; (2) ElNi microspring; (3) Magnetic encoder soldered on a PCB; (4) Adjusting screw; (5) Microgripper for pulling the sample during tensile testing.

The main benefit of microspring based force sensing microgripper compared to the PVDF based force sensing microgripper is the capability of reporting the strain independently. Figure 5.9 illustrates how the strain is measured. The fiber is grasped between the force sensitive microgripper (SG) and the pulling microgripper (PG). During a tensile test, the displacement of SG is measured using the magnetic encoder, ΔL_S, and the displacement of PG is measured using the in-built optical encoder in the 3D-micromanipulator, ΔL_G. The initial length of the fiber, L_0, is measured using the top-view image. Therefore it is possible to calculate the fiber elongation, ΔL, and strain, ϵ, as follows:

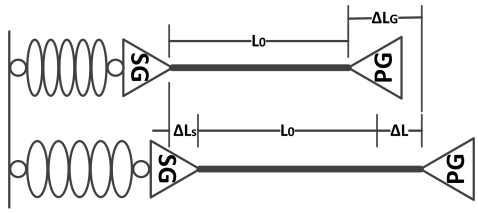

Figure 5.9: Strain Measurement.

$$\Delta L = \Delta L_G - \Delta L_S, \qquad \epsilon = \Delta L / L_0 \, . \tag{5.3}$$

Since the microgripper which was integrated into the microspring based force sensor is an out-of-shelf component with the gripping force of 0.3 N, it does not have sufficient gripping force to perform tensile tests on paper fibers. In order to expand the application of the microspring based force sensing microgripper, it is required to replace the current microgripper with another one which has sufficient gripping force. However, to demonstrate the capabilities of the developed force sensing microgripper in tensile studies, electrospun cellulose fibers were selected. The mechanical properties of the electrospun cellulose fibers can be measured without slippage of fibers from the microgrippers. The micro tensile-testing is performed with the rate of 1 $\mu m/s$ using a stair input signal by moving the PG 1 μm and pausing for 1 s continuously. Figure 5.10 shows a cellulose fiber during micro tensile-testing.

Figure 5.11 shows the force-strain curve of a micro tensile-testing of a cellulose fiber. The force-strain curve is plotted according to Figure 4.37 and Equation 5.4. The validated force range is marked according to Figure 4.36. The slope of the graph at validated force range is 53270 μN which represents the value of Young's modulus times the cross-section area. Since the cellulose fiber does not have a uniform cross section area it is not possible to plot the stress-strain curve.

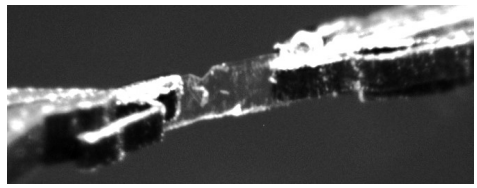

Figure 5.10: Micro tensile-testing of a synthetic cellulose fiber.

$$Force = 91.17 D_{oM} + 3647 \tag{5.4}$$

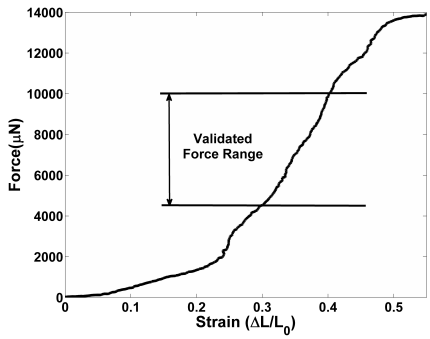

Figure 5.11: Force-Strain curve of a micro tensile-testing of a cellulose fiber.

5.4 Discussions

The aforementioned characterizing setups, provide the infrastructure to measure various types of fibrous materials as it was demonstrated. The PVDF based force sensing microgripper lacks a mean to measure strain during micro tensile-testing, but because of PVDF properties, if it is calibrated for its entire working frequency range, it can also work as a dynamic force sensor at micro-scale. Even at its current stage as a working prototype, the PVDF based force sensing microgripper is used to provide useful data for the industry such as the effect of refining on bond strength of pulp fibers in Z-directional and shear-mode.

The microspring based force sensing microgripper can measure the strain independently. Its main weakness is the insufficient gripping force, 0.3 N, for tensile testing of materials such as CNTs or glass fibers. The fiber slips away from the jaws and it is detectable in the force signal as a sudden drop. Yet its is possible to use this setup to characterize softer fibrous materials such as regenerated cellulose fibers.

6 Summary

This chapter summarizes the obtained results of this thesis and concludes them. The research questions stated in Chapter 1 are resolved and guidelines on how to improve and continue this work in the future are provided.

6.1 Thesis Summary and Conclusions

A microrobotic platform to address the challenges of handling and specimen preparation of micro-scale fibrous materials was developed. The platform was used to prepare fibrous material samples for SEM and NT [4]. The performed experiments demonstrate that using this platform makes it possible to prepare specimens from various fibrous materials without the introduction of artifacts. The samples can be placed on various holders to be used in a wide range of microscopy applications [4].

The capabilities of this platform were also demonstrated in making individual paper fiber bonds [2, 5]. In the conventional methods of making individual paper fiber bonds, the fibers are randomly oriented which leads to random crossing and vertical angles. Creating individual paper fiber bonds using the microrobotic platform, results in desirable cross-

ing and vertical angles [2, 5]. Controlling the quality of the specimens of individual paper fiber bonds in both the making and the mounting phases, can help paper fiber scientists to achieve better results in their experiments. From this, a better understanding and analysis of the true nature of bonding mechanisms between two paper fibers can be reached, than was previously possible. Considering all the aforementioned specimen handling processes, this level of accuracy on manipulating and mounting the micro-scale fibers is out-of-reach in manual specimen handling processes.

Two PVDF based force sensing microgripper were developed. The first one with the passive specimen holder for Z-directional bonding force measurement was successfully designed, fabricated and calibrated [3]. The PVDF film sensor was integrated into a microrobotic platform and its ability to measure fiber bond strength was demonstrated successfully [3, 133]. This micro-force sensor has a linear output and it can be reliably used. It appears that all of the values for Z-directional bond strength reported in the literature are for hand-sheets rather than for individual bonds. Therefore, it is only possible to compare our force values for the Z-directional bond strength with other loading modes such as shear or peeling. Nevertheless, the measured values for the Z-directional bond strength are in the expected range of 1 mN to 20 mN [27].

The development phases of a microspring based force sensing microgripper were described. As a proof of concept it was shown that rolling-resistance and friction of a PLS can be small enough to allow force measurements in milli-Newton force range [7]. Next, the design of the microspring was optimized, and it was fabricated. The elliptical microspring and a magnetic encoder were integrated into a microgripper attached to a PLS to form a force sensing microgripper for micro-tensile testing application. After calibration of the microspring based force sensing microgripper, it was integrated into a microrobotic platform and its capability to perform tensile testing on fibrous materials was demonstrated successfully.

6.2 Resolution of Research Questions and Future Work

The research questions stated in Chapter 1 were addressed in Chapters 3 and 4, and demonstrated in Chapter 5. In the following each research question is answered and the future steps to improve and continue this research are discussed:

RQ.1 Which microrobotic solution can address the challenges of handling and specimen preparation of micro-scale fibrous materials?

In Chapter 3, it was shown that a microrobotic platform with stacked gantry crane configuration can address the challenges for manipulation and specimen preparation of micro-scale fibrous materials [4]. It minimizes the human interaction with the specimens while decreasing the specimen preparation time. For the first time using the developed microrobotic platform perpendicular bonds were made and measured [5]. The requirement of flexibility and easy configurability for various micro-scale fibrous samples and specimen holders is typical in material research.

To facilitate flexibility, the specimen preparation processes described in this thesis were performed in a tele-operation mode. However, if a future industrial application requires less flexibility but higher speed, the platform provides an infrastructure to prepare stacks of micro-scale fibrous specimens automatically. Even though only paper fiber and human hair have been used in the experiments, the capabilities of the platform support the handling of other fibrous materials such as glass fibers in the same dimensional range. The design and fabrication of rotational piezo-actuators for the microgrippers is reported in [135]. In order to untwist the paper fibers, the rotational piezo-actuators should be integrated into the microgrippers in the future. In addition, a piezo fiber press can be integrated into the platform to monitor the pressing force on the fiber bonds. The design and fabrication of the piezo fiber press is reported in [122].

RQ.2 Which force sensing approach can measure bonding forces of paper fiber bonds in individual level?

In Chapter 4, a novel method for the measurement of individual bond breaking forces using a PVDF film in bending mode was developed. A passive specimen holder was attached to the PVDF film to form a force sensor for Z-directional bonding force measurement. Based on the same principle, a PVDF film was integrated with a microgripper to measure individual bond breaking forces in shear-mode.

The author recognizes that this micro-force sensor could be improved upon as follows: the geometry of the sensor should be optimized to achieve the highest possible sensitivity; the sensor should be calibrated with different deformation rates to be used as dynamic sensor, and it could also be calibrated for forces higher than 10 mN with a sufficiently high force range reference sensor. In order to perform the measurements with lower rates, it is necessary to optimize the charge amplifier of the PVDF based force sensor. In addition, the developed force sensing microgrippers should be integrated into the 3D-micromanipulators. This will allow measuring the tension on the crossing fiber while performing a bond strength measurement. In order to fully resolve the force components on a bond plane, a micro-torque sensor should be developed to measure the torque required to untwist the crossing fiber during bond strength measurements. This will significantly enhance the understanding of bond failure mechanisms.

RQ.3 Which force sensing approach can be used for micro-tensile testing of fibers using a microgripper?

In Chapter 4 of this thesis, a novel force sensing approach for microgrippers used in micro-tensile testing applications was proposed. Use of ElNi microsprings based force sensor for micro-tensile testing applications is a new approach. For the first time, in this thesis, an elliptical ElNi microspring is designed, fabricated and integrated into a PLS for force sensing applications.

Improving the wiring of microgripper and also fine tuning the

fabrication process of ElNi microspring to provide vertical sidewalls will increase the sensitivity of the sensor. It is possible to utilize the existing fabrication knowledge of ElNi to produce microsprings which behave linearly in arbitrary micro-Newton force ranges by controlling the plating temperature and the current density, as well as by designing a proper structure and dimensions for the microspring. Therefore, if a microgripper for a new force range is required, the wide range of values available for the Young's modulus of ElNi allows maintaining the other components of a microgripper same and only fabricating a new microspring for the new force range. It is required to develop a microgripper with sufficient gripping force in order to perform tensile testing on various fibrous materials.

Bibliography

[1] L. Kappel, U. Hirn, W. Bauer, and R. Schennach, "A novel method for the determination of bonded area of individual fiber-fiber bonds," *Jr. Nordic Pulp and Paper Research*, vol. 24, no. 2, pp. 199–205, 2009.

[2] P. Saketi and P. Kallio, "Microrobotic platform for making, manipulating and breaking individual paper fiber bonds," in *Assembly and Manufacturing (ISAM), 2011 IEEE International Symposium on*, 2011, pp. 1–6.

[3] P. Saketi, S. K. Latifi, J. Hirvonen, S. Rajala, A. Vehkaoja, T. Salpavaara, J. Lekkala, and P. Kallio, "Pvdf microforce sensor for the measurement of z-directional strength in paper fiber bonds," *Sensors and Actuators A: Physical*, vol. 222, no. 0, pp. 194 – 203, 2015.

[4] P. Saketi, M. v. Essen, M. Mikczinski, S. Heinemann, S. Fatikow, and P. Kallio, "A flexible microrobotic platform for handling microscale specimens of fibrous materials for microscopic studies," *Journal of microscopy*, vol. 248, no. 2, pp. 163 –171, 2012.

[5] P. Saketi, M. Mikczinski, S. Fatikow, and P. Kallio, "Method for investigation of aged fibre-fibre bonds with micro and nanorobotic tools," *The 15th Pulp and Paper Fundamental Research Symposium*, vol. 1, pp. 125–142, 2013.

[6] P. Saketi and P. Kallio, "Measuring bond strength of individual paper fibers using microrobotics," in *Progress in Paper Physics*, vol. 1, 2011, pp. 199–203.

[7] P. Saketi, P. Wangyang, H. Li, Q. Wang, and P. Kallio, "Electroplated nickel microspring and low-friction precision linear slider: A novel micro-force sensing tool," in *IEEE International Conference on Robotics and Automation (ICRA'15)*, Seattle, USA, May 2015.

[8] T. Duttenhofer and M. Walter, "Technical documentation, project: mw260 – parts from sub1131," MicroWorks GmbH, Germany, Tech. Rep., 2014.

[9] M. Kojima, H. Yamamoto, M. Yoshida, Y. Ojio, and K. Okumura, "Maturation property of fast-growing hardwood plantation species: A view of fiber length," *Jr. Forest Ecology and Management*, vol. 257, no. 1, pp. 15–22, 2009.

[10] L. Paavilainen, "Importance of particle-size fiber length and fines for the characterization of softwood kraft pulp," *Jr. Paperi ja Puu (Paper and Timber)*, vol. 72, no. 5, pp. 516–526, 1990.

[11] J. Raczkowski, L. Helinska-Raczkowska, and W. Molinski, "Relationship between lengthwise ultrasound transmission and tracheid length in wood of selected softwood species," *Jr. FOLIA FORESTALIA POLONICA*, vol. 1, no. 35, pp. 3–12, 2004.

[12] C. Ververis, K. Georghiou, N. Christodoulakis, P. Santas, and R. Santas, "Fiber dimensions, lignin and cellulose content of various plant materials and their suitability for paper production," *Jr. Industrial Crops and Products*, vol. 19, no. 3, pp. 245–254, 2004.

[13] W. Campbell, *The cellulose-water relationship in papermaking*, ser. Bulletin (Canada. Dominion Forest Service). Ottawa, Printer to the King's most excellent Majesty, 1933, no. 84.

[14] H. J. J. Allison, "The relation between surface activity and fiber-bond strength in papermaking pulp," Ph.D. dissertation, Institute of Paper Science and Technology, Georgia Institute of Technology, 1940.

[15] J. V. den Akker, "Structural aspects of bonding," *Tappi J.*, vol. 42, no. 12, pp. 940–947, 1959.

[16] D. Page, "Fibre-to-fibre bonds part 1 – a method for their direct observation," *Paper Technology*, vol. 1, no. 4, pp. 407–411, 1960.

[17] D. H. Page, "A theory for the tensile strength of paper," *Jr. Tappi*, vol. 52, no. 4, pp. 674–681, 1969.

[18] T. Lindström, L. Wågberg, and T. Larsson, "On the nature of joint strength in paper – a review of dry and wet strength resins used in paper manufacturing," in *13th Fundamental Research Symposium*, Cambridge, Uk, Sep. 2005, pp. 457–562.

[19] U. Hirn, R. Schennach, C. Ganser, M. Magnusson, C. Teichert, and S. Östlund, "The area of molecular contact in fiber-fiber bonds," *The 15th Pulp and Paper Fundamental Research Symposium*, vol. 1, pp. 201–223, 2013.

[20] R. Schennach, U. Hirn, A. E. Horvath, F. Schmied, and C. Teichert, "A model approach to understand the fiber – fiber bond in paper," in *Progress in Paper Physics Seminar*, Graz, Austria, Sep. 2011, pp. 211–212.

[21] A. Kulachenko and T. Uesaka, "Direct simulations of fiber network deformation and failure," *Mechanics of Materials*, vol. 51, no. 0, pp. 1 – 14, 2012.

[22] A. Kulachenko, P. Gradin, and H. Koivurova, "Modelling the dynamical behaviour of a paper web. part i," *Computers & Structures*, vol. 85, no. 3–4, pp. 131 – 147, 2007.

[23] ——, "Modelling the dynamical behaviour of a paper web. part ii," *Computers & Structures*, vol. 85, no. 3–4, pp. 148 – 157, 2007.

[24] R. A. Stratton and N. L. Colson, "Dependence of fiber/fiber bonding on some papermaking variables," in *SYMP on Materials Interactions Relevant to the Pulp, Paper, and Wood Industries*, San Francisco, USA, Apr. 1990, pp. 173–181.

[25] F. Schmied, C. Ganser, W. Fischer, U. Hirn, W. Bauer, R. Schennach, and C. Teichert, "Insights into single fiber-fiber bonds using atomic force microscopy," in *Progress in Paper Physics Seminar*, Graz, Austria, Sep. 2011, p. 197.

[26] M. S. Magnusson and S. Östlund, "Inter-fibre bond strength and combined normal and shear loading," in *Progress in Paper Physics Seminar*, Graz, Austria, Sep. 2011, pp. 205–207.

[27] F. J. Schmied, C. Teichert, L. Kappel, U. Hirn, W. Bauer, and R. Schennach, "What holds paper together: Nanometre scale exploration of bonding between paper fibres," *Scientific Reports*, vol. 3, no. 2432, pp. 1–6, 2013.

[28] T. Uesaka, "Fibre-fibre bond: What paper physicist sees," in *International Paper Physics Conference*, Stockholm, Sweden, Jun. 2012, pp. 12–14.

[29] L. Nordman, C. Gustafsson, and G. Olofsson, "The strength of bondings in paper ii," *PAP PUU-PAP TIM*, vol. 1, no. 8, pp. 315–320, 1954.

[30] A. Koubaa and Z. Koran, "Measure of the internal bond strength of paper/board," *Jr. Tappi*, vol. 78, no. 3, pp. 103–111, 1995.

[31] C. Hammond and P. J. Evennett, "Sample preparation for light microscopy," *Microscopy Techniques*, vol. 42, pp. 106 –114, 2005.

[32] G. J. Monkman, "Robot grippers for use with fibrous materials," *Robotic Research*, vol. 14, pp. 144 –151, 1995.

[33] M. Probst, C. Hurzeler, R. Borer, and B. J. Nelson, "A microassembly system for the flexible assembly of hybrid robotic mems devices," *Int. Jr. of Optomechatronics*, vol. 3, no. 2, pp. 69–90, 2009.

[34] M. Probst, M. Fluckiger, S. Pane, O. Ergeneman, Z. Nagy, and B. J. Nelson, "Manufacturing of a hybrid acoustic transmitter using an advanced microassembly system," *IEEE Transactions on Industrial Electronics*, vol. 56, no. 7, pp. 2657–2666, 2009.

[35] S. J. Ralis, B. Vikramaditya, and B. J. Nelson, "Micropositioning of a weakly calibrated microassembly system using coarse-to-fine visual servoing strategies," *IEEE Transactions on Electronics Packaging Manufacturing*, vol. 23, no. 2, pp. 123–131, 2000.

[36] B. Tamadazte, N. Le Fort-Piat, S. Dembélé, and G. Fortier, "Robotic micromanipulation for microassembly: modelling by sequencial function chart and achievement by multiple scale visual servoings," *Journal of Micro-Nano Mechatronics*, vol. 5, no. 1-2, pp. 1–14, 2009.

[37] K. N. Andersen, S. Fatikow, and P. Boggild, "Nanorobotic manipulation setup for pick-and-place handling and nondestructive characterization of carbon nanotubes," in *IEEE/RSJ International Conference on Intelligent Robots and Systems*, 2007 2007, pp. 291–296.

[38] K. Carlson *et al.*, "A carbon nanofibre scanning probe assembled using an electrothermal microgripper," *Jr. Nanotechnology*, vol. 18, no. 34, p. 7, 2007.

[39] L. Chen, W. Rong, L. Sun, and H. Xie, "Micromanipulation robot for automatic fiber alignment," in *IEEE International Conference on Mechatronics and Automation*, 2005, pp. 1756 – 1759.

[40] W. Chen and W. Lin, "Design of a flexure-based gripper used in optical fiber handling," in *IEEE Conference on Robotics, Automation and Mechatronic*, 2004, pp. 83–88.

[41] Z. Ling and K. Lian, "New fabrication techniques of su-8 fiber holder with cantilever-type elastic microclips by inclined uv lithography in water using single mylar mask," *Microsystems Technology*, vol. 16, pp. 405 – 410, 2010.

[42] F. Arai, T. Sakami, H. Maruyama, A. Ichikawa, and T. Fukuda, "Minimally invasive micromanipulation of microbe by laser trapped micro tools," in *Proc. IEEE International Conference on Robotics and Automation*, Washington DC, USA, May 2002, pp. 1937–1942.

[43] A. Georgiev, P. K. Allen, and W. Edstrom, "Visually-guided protein crystal manipulation using micromachined silicon tools," in *Proc. IEEE/RSJ International Conference on Intelligent Robots and Systems)*, Sendai, Japan, Sep./Oct. 2004, pp. 236–241.

[44] K. Inoue, T. Arai, T. Tanikawa, and K. Ohba, "Dexterous micromanipulation supporting cell and tissue engineering," in *IEEE SYMP on Micro-NanoMechatronics and Human Science*, Nagoya, Japan, Nov. 2005, pp. 197–202.

[45] P. Kallio and J. Kuncova, "Capillary pressure microinjection of living adherent cells: Challenges in automation," *Jr. Micromechatronics*, vol. 3, no. 3-4, pp. 189–220, 2006.

[46] J. Park *et al.*, "An integrated bio cell processor for single embryo cell manipulation," in *Proc. IEEE/RSJ International Conference on Intelligent Robots and Systems*, Sendai, Japan, Sep./Oct. 2004, pp. 242–247.

[47] Y. Sun, M. A. Greminger, and B. J. Nelson, "Investigating protein structure with a microrobotic system," in *Proc. IEEE International Conference on Robotics and Automation (ICRA 2004)*, New Orleans, USA, Apr./May 2004, pp. 2854–2859.

[48] E. W. H. Jager, O. Inganäs, and I. Lundstörm, "Microrobots for micrometer-size objects in aqueous media: potential tools for single-cell manipulation," *Science*, vol. 288, pp. 2335–2338, 2000.

[49] T. Yang, L. Holzer, R. Kägi, F. Winnefeld, and B. Keller, "In situ nanomanipulators as a tool to separate individual tobermorite crystals for {AFM} studies," *Ultramicroscopy*, vol. 107, no. 10–11, pp. 1068 – 1077, 2007.

[50] C. H. Mayhood, J. O. J. Kallmes, and M. M. Cauley, "Mechanical properties of paper; part ii: Measured shear strength of individual fiber to fiber contacts," *TAPPI*, vol. 45, no. 1, pp. 69–73, 1962.

[51] W. J. Fischer, U. Hirn, W. Bauer, and R. Schennach, "Testing of individual fibre-fibre joints under biaxial load and simultaneous analysis of deformation," *Nordic Pulp and Paper Research Journal*, vol. 27, pp. 237–244, 2012.

[52] M. S. Magnusson, X. Zhang, and S. Östlund, "Experimental evaluation of the interfibre joint strength of papermaking fibres in terms of manufacturing parameters and in two different loading directions," *Experimental Mechanics*, vol. 53, pp. 1621–1634, 2013.

[53] T. Uesaka, *Determination of fibre-fibre bond properties*, ser. Handbook of physical and mechanical testing of paper and paperboard. Marcel Dekker, New York, 1984, pp. 379–402.

[54] A. P. Schniewind, L. J. Nemeth, and D. L. Brink, "Fiber and pulp properties; i. shear strength of single-fiber crossings," *TAPPI*, vol. 47, no. 4, pp. 244–248, 1964.

[55] K. W. Hardacker, "The automatic recording of the load-elongation characteristic of single papermaking fibers - IPC fiber load-elongation recorder," *Jr. Tappi*, vol. 45, no. 3, pp. 237–246, 1962.

[56] C. Thomson, R. Lowe, D. Page, and A. Ragauskas, "Exploring fibre-fibre interfaces via fret and fluorescence microscopy," *Journal of Pulp and Paper Science*, vol. 34, no. 2, pp. 113–120, 2008.

[57] A. Torgnysdotter, A. Kulachenko, P. Gradin, and L. Wågberg, "The link between the fiber contact zone and the physical properties of paper: A way to control paper properties," *Journal of Composite Materials*, vol. 41, no. 13, pp. 1619–1633, 2007.

[58] C. Marulier, P. Dumont, L. Orgéas, D. Caillerie, and S. Du Roscoat, "Towards 3d analysis of pulp fibre networks at the fibre and bond levels," *Nordic Pulp and Paper Research Journal*, vol. 27, no. 2, pp. 245–255, 2012.

[59] C. Marulier, P. Dumont, L. Orgéas, S. Rolland du Roscoat, and D. Caillerie, "3d analysis of paper microstructures at the scale of fibres and bonds," *Cellulose*, vol. 22, no. 3, pp. 1517–1539, 2015.

[60] J. Tang, H. Wang, R. Liu, X. Li, Z. Zhang, J. Yao, and G. Ding, "A directly strain measuring method for electroplated nickel micro-tensile test," *Microsystem Technologies*, vol. 16, no. 11, pp. 1839–1844, 2010.

[61] T. Tsuchiya, M. Shikida, and K. Sato, "Tensile testing system for sub-micrometer thick films," *Sensors and Actuators A: Physical*, vol. 97-98, no. 0, pp. 492–496, 4/1 2002.

[62] H. S. Cho, K. J. Hemker, K. Lian, J. Goettert, and G. Dirras, "Measured mechanical properties of liga ni structures," *Sensors and Actuators A: Physical*, vol. 103, no. 1-2, pp. 59–63, 1/15 2003.

[63] Y. Yang, N. Yao, W. O. Soboyejo, and C. Tarquinio, "Deformation and fracture in micro-tensile tests of freestanding electrodeposited nickel thin films," *Scripta Materialia*, vol. 58, no. 12, pp. 1062–1065, 6 2008.

[64] U. Lang, M. Reichen, and J. Dual, "Fabrication of a tensile test for polymer micromechanics," *Microelectronic Engineering*, vol. 83, no. 4-9, pp. 1182–1184, 0 2006.

[65] K. Nagayama, S. Yanagihara, and T. Matsumoto, "A novel micro tensile tester with feed-back control for viscoelastic analysis of single isolated smooth muscle cells," *Medical engineering and physics*, vol. 29, no. 5, pp. 620–628, 6 2007.

[66] A. Gestos, P. G. Whitten, G. M. Spinks, and G. G. Wallace, "Tensile testing of individual glassy, rubbery and hydrogel electrospun polymer nanofibres to high strain using the atomic force microscope," *Polymer Testing*, vol. 32, no. 4, pp. 655–664, 6 2013.

[67] M. Eder, S. Stanzl-Tschegg, and I. Burgert, "The fracture behaviour of single wood fibres is governed by geometrical constraints: in situ esem studies on three fibre types," *Wood Science and Technology*, vol. 42, no. 8, pp. 679–689, 12/01 2008.

[68] E. Zussman, X. Chen, W. Ding, L. Calabri, D. A. Dikin, J. P. Quintana, and R. S. Ruoff, "Mechanical and structural characterization of electrospun pan-derived carbon nanofibers," *Carbon*, vol. 43, no. 10, pp. 2175–2185, 8 2005.

[69] "Instron model 5848 microtester user manual," http://www.instron.com/wa/library/StreamFile.aspx?doc=808, Tech. Rep., [accessed 5 June 2014].

[70] L. Q. Liu, D. Tasis, M. Prato, and H. D. Wagner, "Tensile mechanics of electrospun multiwalled nanotube/poly(methyl methacrylate) nanofibers," *Advanced Materials*, vol. 19, no. 9, pp. 1228–1233, 2007.

[71] W. N. S. Jr., "An interferometric strain/displacement measurement system," Tech. Rep., 1989.

[72] W. N. S. Jr., B. Yuan, and R. L. Edwards, "A new technique for measuring the mechanical properties of thin films," *Journal of Microelectromechanical Systems*, vol. 6, no. 3, pp. 193–199, 1997.

[73] M. Zupan, M. J. Hayden, C. J. Boehlert, and K. J. Hemker, "Development of high-temperature microsample testing," *Experimental Mechanics*, vol. 41, no. 3, pp. 242–247, 09/01 2001.

[74] Y.-W. Cheng, D. T. Read, J. D. McColskey, and J. E. Wright, "A tensile-testing technique for micrometer-sized free-standing thin films," *Thin Solid Films*, vol. 484, no. 1-2, pp. 426–432, 7/22 2005.

[75] Y. Zhu and H. D. Espinosa, "An electromechanical material testing system for in situ electron microscopy and applications," *Proceedings of the National Academy of Sciences of the United States of America*, vol. 102, no. 41, pp. 14 503–14 508, October 11 2005.

[76] E. Bamberg, C. P. Grippo, P. Wanakamol, A. H. Slocum, M. C. Boyce, and E. L. Thomas, "A tensile test device for in situ atomic force microscope mechanical testing," *Precision Engineering*, vol. 30, no. 1, pp. 71–84, 1 2006.

[77] T. Fukuda, K. Tanie, and T. Mitsuoka, "Study on control of a micro-manipulator (1st report, basic characteristics of a micro-gripper and a method of bilateral control)." *Nippon Kikai Gakkai Ronbunshu, C Hen/Transactions of the Japan Society of Mechanical Engineers, Part C*, vol. 53, no. 493, pp. 1950–1956, 1987.

[78] C.-J. Kim, A. P. Pisano, R. S. Muller, and M. G. Lim, "Polysilicon microgripper," in *Solid-State Sensor and Actuator Workshop, 1990. 4th Technical Digest., IEEE*, 1990, pp. 48–51.

[79] ——, "Design, fabrication, and testing of a polysilicon microgripper," in *American Society of Mechanical Engineers, Dynamic Systems and Control Division (Publication) DSC*, Dallas, USA, Nov. 1990, pp. 99–109.

[80] ——, "Polysilicon microgripper," *Sensors and Actuators: A. Physical*, vol. 33, no. 3, pp. 221–227, 1992.

[81] C.-J. Kim, A. P. Pisano, and R. S. Muller, "Silicon-processed overhanging microgripper," *Journal of Microelectromechanical Systems*, vol. 1, no. 1, pp. 31–36, 1992.

[82] M. Kohl, B. Krevet, and E. Just, "Sma microgripper system," *Sensors and Actuators, A: Physical*, vol. 97-98, pp. 646–652, 2002.

[83] O. Sardan, V. Eichhorn, D. H. Petersen, S. Fatikow, O. Sigmund, and P. Bøggild, "Rapid prototyping of nanotube-based devices using topology-optimized microgrippers," *Nanotechnology*, vol. 19, no. 49, p. 495503, 2008.

[84] R. Pérez, J. Agnus, C. Clévy, A. Hubert, and N. Chaillet, "Modeling, fabrication, and validation of a high-performance 2-DoF piezoactuator for micromanipulation," *IEEE/ASME Transactions on Mechatronics*, vol. 10, no. 2, pp. 161–171, 2005.

[85] D. H. Wang, Q. Yang, and H. M. Dong, "A monolithic compliant piezoelectric-driven microgripper: Design, modeling, and testing," *Mechatronics, IEEE/ASME Transactions on*, vol. 18, no. 1, pp. 138–147, 2013.

[86] D.-H. Kim, M. G. Lee, and Y. S. Byungkyu Kim and, "A superelastic alloy microgripper with embedded electromagnetic actuators and piezoelectric force sensors: a numerical and experimental study," *Smart Materials and Structures*, vol. 14, no. 6, p. 1265, 2005.

[87] D. Kim, B. Kim, and H. Kang, "Development of a piezoelectric polymer-based sensorized microgripper for microassembly and micromanipulation," *Microsystem Technologies*, vol. 10, no. 4, pp. 275–280, 2004.

[88] K. Kim, X. Liu, Y. Zhang, J. Cheng, X. Y. Wu, and Y. Sun, "Elastic and viscoelastic characterization of microcapsules for drug delivery using a force-feedback MEMS microgripper," *Biomedical Microdevices*, vol. 11, no. 2, pp. 421–427, 2009.

[89] T. C. Duc, G. K. Lau, J. F. Creemer, and P. M. Sarro, "Electrothermal microgripper with large jaw displacement and integrated force sensors," *Microelectromechanical Systems, Journal of*, vol. 17, no. 6, pp. 1546–1555, 2008.

[90] S. A. Bazaz, F. Khan, and R. I. Shakoor, "Design, simulation and testing of electrostatic SOI MUMPs based microgripper integrated with capacitive contact sensor," *Sensors and Actuators A: Physical*, vol. 167, no. 1, pp. 44–53, 2011.

[91] F. Beyeler, A. Neild, S. Oberti, D. J. Bell, Y. Sun, J. Dual, and B. J. Nelson, "Monolithically fabricated microgripper with integrated force sensor for manipulating microobjects and biological cells aligned in an ultrasonic field," *Microelectromechanical Systems, Journal of*, vol. 16, no. 1, pp. 7–15, 2007.

[92] R. E. Mackay, H. R. Le, and R. P. Keatch, "Design optimisation and fabrication of SU-8 based electro-thermal micro-grippers," *Journal of Micro-Nano Mechatronics*, vol. 6, no. 1, pp. 13–22, 2011.

[93] S. Muntwyler, B. E. Kratochvil, F. Beyeler, and B. J. Nelson, "Monolithically integrated two-axis microtensile tester for the mechanical characterization of microscopic samples," *Microelectromechanical Systems, Journal of*, vol. 19, no. 5, pp. 1223–1233, 2010.

[94] G. Eberle, H. Schmidt, and W. Eisenmenger, "Piezoelectric polymer electrets," *Dielectrics and Electrical Insulation, IEEE Transactions on*, vol. 3, no. 5, pp. 624–646, 1996.

[95] H. Kawai, "The piezoelectricity of poly (vinylidene fluoride)," *Japanese Journal of Applied Physics*, vol. 8, no. 7, p. 975, 1969.

[96] "Piezo film sensors, technical manual," http://www.meas-spec.com, Tech. Rep., [accessed 5 May 2014].

[97] J. F. Nye, *Physical properties of crystals*. London: Oxford University Press, 1969.

[98] G. Sessler and A. Berraissoul, "Tensile and bending piezoelectricity of single-film pvdf monomorphs and bimorphs," *Electrical Insulation, IEEE Transactions on*, vol. 24, no. 2, pp. 249–254, Apr 1989.

[99] C. K. M. Fung, I. Elhajj, W. J. Li, and N. Xi, "A 2-d pvdf force sensing system for micro-manipulation and micro-assembly," in *Robotics and Automation, 2002. Proceedings. ICRA '02. IEEE International Conference on*, vol. 2, 2002, pp. 1489–1494.

[100] D.-H. Kim, B. Kim, S. Yun, and S. Kwon, "Cellular force measurement for force reflected biomanipulation," in *Robotics and Automation, 2004. Proceedings. ICRA '04. 2004 IEEE International Conference on*, vol. 3, April 2004, pp. 2412–2417.

[101] Y. Shen, N. Xi, W. J. Li, and J. Tan, "A high sensitivity force sensor for microassembly: design and experiments," in *Advanced Intelligent Mechatronics, 2003. AIM 2003. Proceedings. 2003 IEEE/ASME International Conference on*, vol. 2, 2003, pp. 703–708.

[102] Y. Shen, N. Xi, K. W. C. Lai, and W. J. Li, "A novel pvdf microforce/force rate sensor for practical applications in micromanipulation," *Sensor Review*, vol. 24, no. 3, pp. 274–283, 2004.

[103] D.-H. Kim, Y. Soek, and B. Kim, "Mechanical force response of single living cells using a microrobotic system," in *Robotics and Automation, 2004. Proceedings. ICRA '04. 2004 IEEE International Conference on*, vol. 5, 2004, pp. 5013–5018.

[104] Y. Xie, D. Sun, C. Liu, S. H. Cheng, and Y. H. Liu, "A force control based cell injection approach in a bio-robotics system," in *Robotics and Automation, 2009. ICRA '09. IEEE International Conference on*, 2009, pp. 3443–3448.

[105] Z. Sun, W. Chen, Y. Su, and L. Hao, "A micro-force-tracking system based on pvdf static micro-force sensor and fuzzy-pid control method," *Mechatronics and Information Technology, Pts 1 and 2*, vol. 2-3, pp. 489–494, 2012.

[106] Z. Yang, G. Ding, H. Cai, X. Xu, H. Wang, and X. Zhao, "Analysis and elimination of the 'skip contact' phenomenon in an inertial micro-switch for prolonging its contact time," *Journal of Micromechanics and Microengineering*, vol. 19, no. 4, pp. 045 017–045 027, 2009.

[107] P. Wang, K. Tanaka, S. Sugiyama, X. Dai, X. Zhao, and J. Liu, "A micro electromagnetic low level vibration energy harvester based on MEMS technology," *Microsystem Technologies*, vol. 15, no. 6, pp. 941–951, 2009.

[108] T. Fritz, M. Griepentrog, W. Mokwa, and U. Schnakenberg, "Determination of Young's modulus of electroplated nickel," *Electrochimica Acta*, vol. 48, no. 20-22, pp. 3029–3035, 2003.

[109] S. He, J. S. Chang, L. Li, and H. Ho, "Characterization of Young's modulus and residual stress gradient of MetalMUMPs electroplated nickel film," *Sensors and Actuators A: Physical*, vol. 154, no. 1, pp. 149–156, 2009.

[110] J. K. Luo, A. J. Flewitt, S. M. Spearing, N. A. Fleck, and W. I. Milne, "Young's modulus of electroplated Ni thin film for MEMS applications," *Materials Letters*, vol. 58, no. 17-18, pp. 2306–2309, 2004.

[111] Y. Woo and S.-H. Kim, "Sensitivity analysis of plating conditions on mechanical properties of thin film for MEMS applications," *Journal of Mechanical Science and Technology*, vol. 25, no. 4, pp. 1017–1022, 2011.

[112] H. Majjad, S. Basrour, P. Delobelle, and M. Schmidt, "Dynamic determination of Young's modulus of electroplated nickel used in LIGA technique," *Sensors and Actuators A: Physical*, vol. 74, no. 1-3, pp. 148–151, 1999.

[113] S. Basrour, L. Robert, and P. Delobelle, "Measurement of residual stresses in a plate using bulging test and a dynamic technique: application to electroplated nickel coatings," *Materials Science and Engineering: A*, vol. 288, no. 2, pp. 160–163, 2000.

[114] L. S. Stephens, K. W. Kelly, S. Simhadri, A. B. McCandless, and E. I. Meletis, "Mechanical property evaluation and failure analysis of cantilevered LIGA nickel microposts," *Microelectromechanical Systems, Journal of*, vol. 10, no. 3, pp. 347–359, 2001.

[115] J. Zhang, "Determination of Young's modulus of electroplated nickel-iron (Ni/Fe) and micro-machined Si thin films by the balance method," *Journal of Materials Processing Technology*, vol. 123, no. 3, pp. 329–335, 2002.

[116] K. Liew, C. Wong, and M. Tan, "Tensile and compressive properties of carbon nanotube bundles," *Acta Materialia*, vol. 54, no. 1, pp. 225 – 231, 2006.

[117] C. Tran, W. Humphries, S. Smith, C. Huynh, and S. Lucas, "Improving the tensile strength of carbon nanotube spun yarns using a modified spinning process," *Carbon*, vol. 47, no. 11, pp. 2662 – 2670, 2009.

[118] M. Eder, S. Stanzl-Tschegg, and I. Burgert, "The fracture behaviour of single wood fibres is governed by geometrical constraints: in situ esem studies on three fibre types," *Wood Science and Technology*, vol. 42, no. 8, pp. 679–689, 2008.

[119] R. Liu, H. Wang, X. Li, J. Tang, S. Mao, and G. Ding, "Analysis, simulation and fabrication of mems springs for a micro-tensile system," *Journal of Micromechanics and Microengineering*, vol. 19, no. 1, p. 015027, 2009.

[120] T. M. Cresson, J. D. Goss, and B. W. Wallace, "Sensor, system, and method for determining z-directional properties of a sheet; us patent: Us5297062a," 1994.

[121] P. Saketi, J. Hirvonen, Y. Lai, C. Ganser, C. Teichert, J. Järnström, P. Fardim, and P. Kallio, "Automated drop-on-fiber contact angle measurement using a microrobotic platform," *Nordic Pulp and Paper Research Journal*, vol. 29, no. 2, pp. 225–231, 2014.

[122] A. M. Ordonez, "Force controlled piezoelectric fiber press," Master Thesis, Tampere University of Technology, 2012.

[123] W. J. Barrow, "Permanence/durability of the book, a two-year research program," *VA: W.J. Barrow Res. Lab Pub. no.1*, 1963.

[124] D. D. Robertson, "The evaluation of paper permanence and durability," *TAPPI*, vol. 59, no. 12, pp. 63–69, 1976.

[125] N. Gurnagul, R. C. Howard, X. Zou, T. Uesaka, and D. H. Page, "The mechanical permanence of paper: A literature review," *Journal of Pulp and Paper Science*, vol. 19, no. 4, pp. 160–166, 1993.

[126] M. J. D. Powell, "An efficient method for finding the minimum of a function of several variables without calculating derivatives," *The Computer Journal*, vol. 7, no. 2, pp. 155–162, 1964.

[127] M. Denn, *Optimization by Variational Methods*. McGraw-Hill, New York, 1969.

[128] A. Morris, *Foundations of Structural Optimization: A Unified Approach*. A Wiley-Interscience Publication, Wiley, New York, 1982.

[129] J. Zhang, H. Zhu, and C. Zhao, "Combined finite element analysis and subproblem approximation method for the design of ultrasonic motors," *Sensors and Actuators A: Physical*, vol. 163, no. 2, pp. 510 – 515, 2010.

[130] M. Walter, "Technical documentation, project: mw260 – lot no. sub 0866," MicroWorks GmbH, Germany, Tech. Rep., 2014.

[131] "Nse-5310 data sheet - miniature position encoder with zero reference and i^2c output," AMS AG, Unterpremstätten, Austria.

[132] W. Bolton, *Mechatronics: Electronic Control Systems in Mechanical and Electrical Engineering*. Pearson Education, Prentice Hall, 2003.

[133] S. K. Latifi, P. Saketi, M. Bozic, and P. Kallio, "The effect of refining on z-directional strength of bleached softwood kraft pulp fiber bonds using microrobotics," in *Progress in Paper Physics*, vol. 1, 2014, pp. 84–86.

[134] S. K. Latifi, P. Saketi, and P. Kallio, "Microrobotic system for multi-rate measurement of bio-based fibres z-directional bond strength," *Journal of Micro-Bio Robotics*, 2015 in Press; Accepted on 14.05.2015.

[135] T. Erden, "Design and implementation of rotational degrees of freedom into microrobotics platform," Master Thesis, Tampere University of Technology, 2014.

Tampereen teknillinen yliopisto
PL 527
33101 Tampere

Tampere University of Technology
P.O.B. 527
FI-33101 Tampere, Finland

ISBN 978-952-15-3545-1
ISSN 1459-2045